Model Development for Organic Semiconductor Heterostructure Devices

A Dissertation
SUBMITTED TO THE FACULTY OF
UNIVERSITY OF MINNESOTA
BY

Feilong Liu

IN PARTIAL FULFILLMENT OF THE REQUIREMENTS
FOR THE DEGREE OF
DOCTOR OF PHILOSOPHY

Professor P. Paul Ruden, Adviser

May 2015

Acknowledgements

In retrospect of the past six years at the University of Minnesota, I believe that it has been the right decision to work on a Ph.D. degree here in the Department of Electrical and Computer Engineering. Completing a Ph.D. is an important step in life, and working with an exceptional adviser has made the process a wonderful journey in my memory.

My adviser Prof. P. Paul Ruden is one of the few most important people that have tremendous impact on my life. He is very knowledgeable, approachable and amiable. Under his guidance and supervision, I have not only aquired the methodology, attitude, and interest in doing academic research, but have been greatly influenced by his personality and charisma as well.

The road to my Ph.D. would not be successful without the following people and I very appreciate the opportunity to work together with all of them. Dr. Darryl L. Smith from Los Alamos National Laboratory has been co-advising me in most of the research projects. I am very impressed by his inspiring thoughts on many topics. Prof. C. Daniel Frisbie, Prof. Russell J. Holmes, Dr. Wei Xie, Dr. Zuoti Xie, and Elliot Schmidt from Department of Chemical Engineering and Materials Science have been providing valuable advice from an interdisciplinary point of view, and I benefit a lot from their discussions and comments throughout the years. My collaborators Dr. Ian H. Campbell, Dr. Brian K. Crone, Dr. Scott A. Crooker, Dr. Aditya D. Mohite, Dr. Avadh B. Saxena, and Dr. Wanyi Nie from Los Alamos National Laboratory have been guiding and helping my research from an experimental perspective, without their well-designed and well-performed experiments, my work on theory development would be meaningless. Former and current Ruden group members Dr. Isaiah P. Steinke, Dr. Mohammad Yunus, Dr. Hsiu-Chuang Chang, Dr. Brijesh Kumar, Jennifer Krohn, Aditi Goswami, Sha Shi, Yue Liu, and Tianbai Cui have been helping me among different research projects and making the office an enjoyable place to work.

I would like to express my gratitude to the funding resources that have been supporting me. The University of Minnesota Graduate School Fellowship and Doctoral Dissertation Fellowship, the National Science Foundation MRSEC program under award No. DMR-0819885, the Los Alamos National Laboratory LDRD program, and the Defense Advanced Research Projects Agency (DAPRA) under grant No. FA2386-11-1-4058. Also I am very thankful to the facilities and travel grants of the Department of Electrical and Computer Engineering, and the Minnesota Supercomputing Institute.

I would also like to mention James Daire and Janice Daire, for their warmest welcome when I came to United States for the first time. Finally, I would like to thank my mother, Junhong Wang, and all my family members and friends who carried me through physical and psychological difficulties.

Dedication

To
my mother
Junhong Wang
and
my father in heaven
Yuliang Liu

Abstract

Organic-semiconductor-based devices have been attracting a large research and development community due to their advantages of flexibility, low cost, and ease of fabrication. They also open up new realms of applications such as spintronic devices. Based on experience from numerous experiments, a heterostructure is a key component for enabling the performance of many types of organic devices such as light-emitting diodes, photovoltaic cells, and field-effect transistors. Theoretical work aims at better understanding the physics as well as providing guidance for future device development. In this dissertation, device theories, models, and calculations for various types of organic devices are developed and presented.

Organic light-emitting and photovoltaic devices have similarity in their structures. In both types of devices, heterostructures are employed. We develop a unified device model combining both the microscopic processes at the heterojunction interface and the macroscopic transport in the bulk. By tuning the parameters, the model can simulate both the light-emitting and photovoltaic devices. The study of carrier density profiles and current-voltage characteristics for different cases provides insight on how different processes affect the device properties.

Model calculations show that the microscopic processes at the heterostructure interface are critical for the efficiency of organic photovoltaic cells. By inserting a thin tunnel barrier at the interface, these processes can be controlled and the device efficiency can be improved. We study the effect of the interfacial layer on the enhancement/ suppression of the processes and incorporate the results into the unified device model.

The calculated short-circuit current and open-circuit voltage agree well with experimental observations.

In organic heterojunction light-emitting diodes, it has been observed that the electroluminescence can be improved significantly (~ 10%) by an external magnetic field. This is caused by the hyperfine interaction between the electron/hole polarons and the hydrogen nuclei of the host molecules, as well as the Zeeman effect due to an external magnetic field. The ratio of singlet/triplet excited states in the polaron pair states at the interface indicates the dominant process. We develop an analytical model using a density matrix approach and rate equations based on quantum statistics, with different types of spin correlation functions. The model calculations agree well with experimental results.

In organic field-effect transistors, a layer of organic ionic liquid has recently been introduced to substitute for a conventional dielectric in order to improve the channel charge density and reduce the operating voltage. The interface between an ionic liquid and an organic semiconductor has interesting physics which is not yet fully understood. We also incorporate this interface into the "heterojunction" family. One important property of this heterojunction is that there exists a coupling effect between the channel conductance and the gate-to-channel capacitance. We propose an equivalent-circuit based model which describes the physical mechanism and explains experimental results.

Table of Contents

List of Tables

List of Figures

Chapter 1 Introduction

1.1 Literature review

Organic electronics has received much attention since the first observation of electrical conductivity in polyacetylene by Alan Heeger's group in 1977.[1] After decades of progress this area has grown tremendously both in industry and academia.[2-5] Various applications have been developed, such as organic light-emitting diodes (OLEDs),[6-8] organic photovoltaic cells (OPCs),[9-11] and organic field effect transistors (OFETs).[12-14] These new devices have significant advantages over traditional technologies, which may open a new era and affect daily life in the near future.

FIG. 1.1 shows a television made from organic light-emitting devices. In contrast to the mainstream LCD technologies requiring a background light source, an OLED generates light within the device itself. Therefore displays using OLED technology

FIG. 1.1. World's largest OLED TV (LG Corporation).

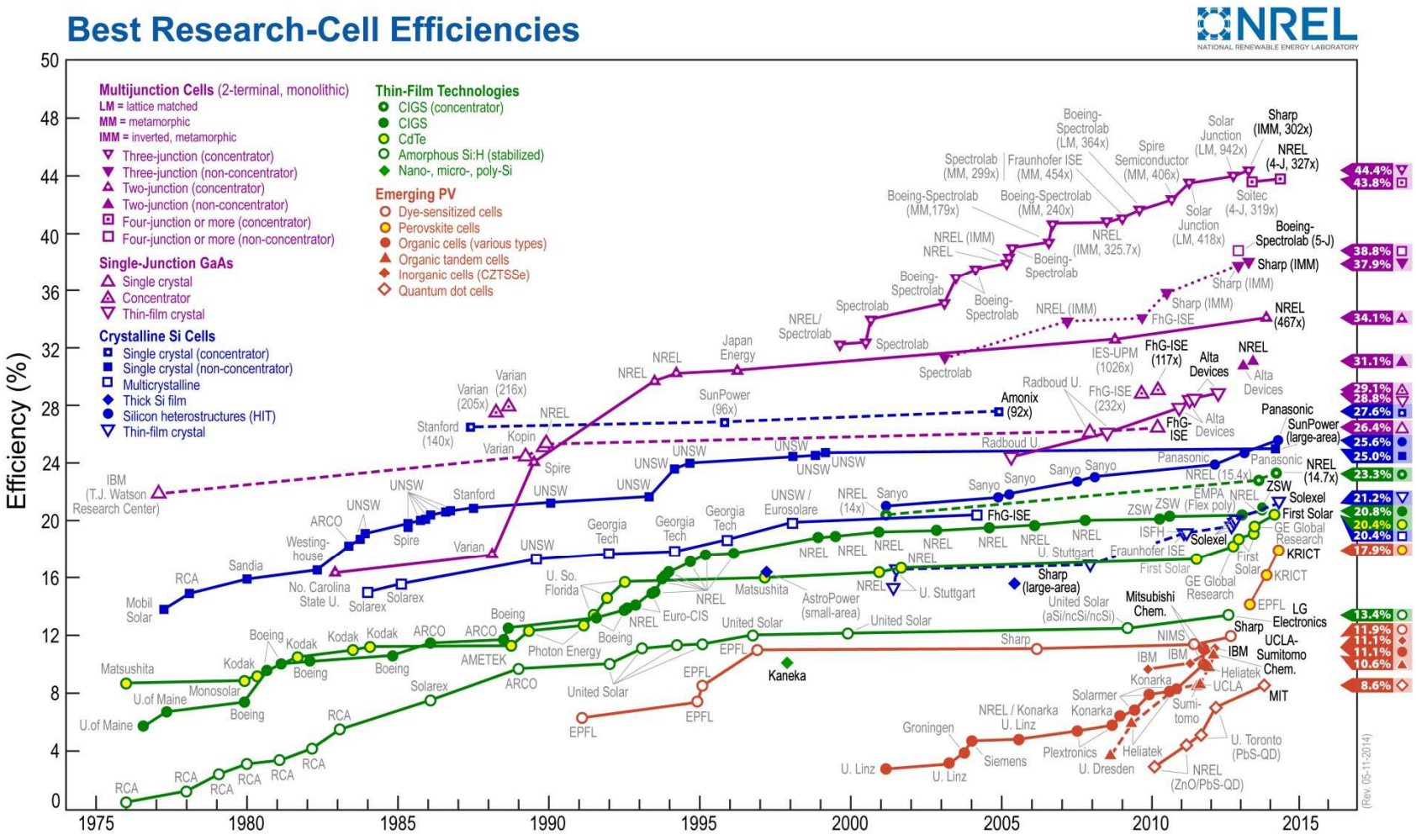

FIG. 1.2. Progress of different types of photovoltaic cell efficiencies (Source: National Center for Photovoltaics).

exhibit bright and vivid colors intrinsically. Another advantage of OLED comes from the fact that organic materials are generally soft and flexible, which facilitates large-area and curved displays giving a more natural view for human eyes.

A solution to the energy crisis today might be the solar cell technology, which converts solar radiation to electricity. Photovoltaic cells based on organic materials are prospective due to their relative ease of fabrication and low cost. Although the efficiency of OPCs is low compared with conventional photovoltaic cells, (shown in FIG. 1.2) the overall cost per unit energy may still make OPCs a competitive option over other candidates.

Field effect transistors are foundations of modern electronic circuits. With the introduction of organic semiconductors, more choices of the substrates besides silicon are available. As shown in FIG. 1.3, OFETs make flexible and bio-compatible circuit applications possible. Although the speed of OFET-based circuits is still slow

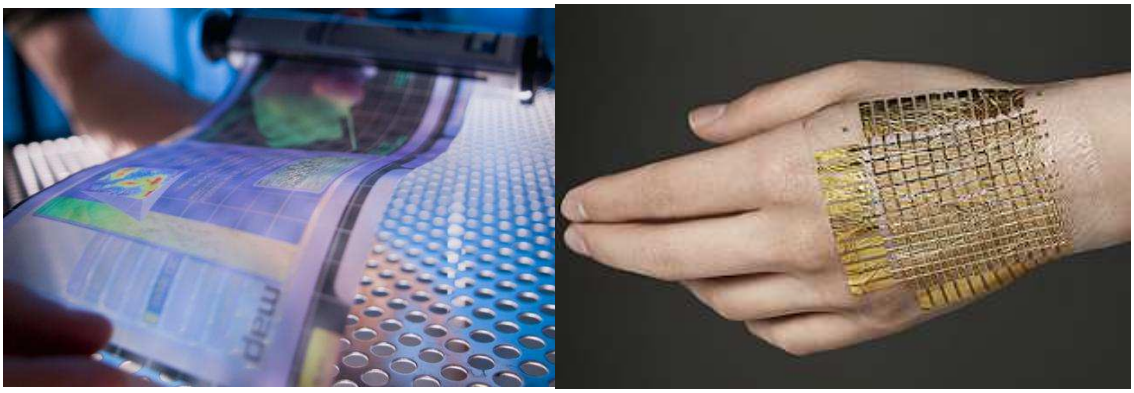

FIG. 1.3. (left) Electronic newspaper fabricated by U.S. Army Research Laboratory and Arizona State University; (right) Electronic “skin” fabricated by University of Tokyo.

compared with conventional technologies, they are promising for applications that do not require fast switching rates.

Revolutionary progress has been made in the past several decades in the research of organic electronics. It is an interdisciplinary field where researchers from chemistry, physics, and electrical engineering have all made great contributions.

The foundation of organic electronics is molecule design and synthesis.[10,15-18] To build a device, the organic molecules are required not only to support good charge transport, but also to exhibit other desired physical and chemical properties. Both

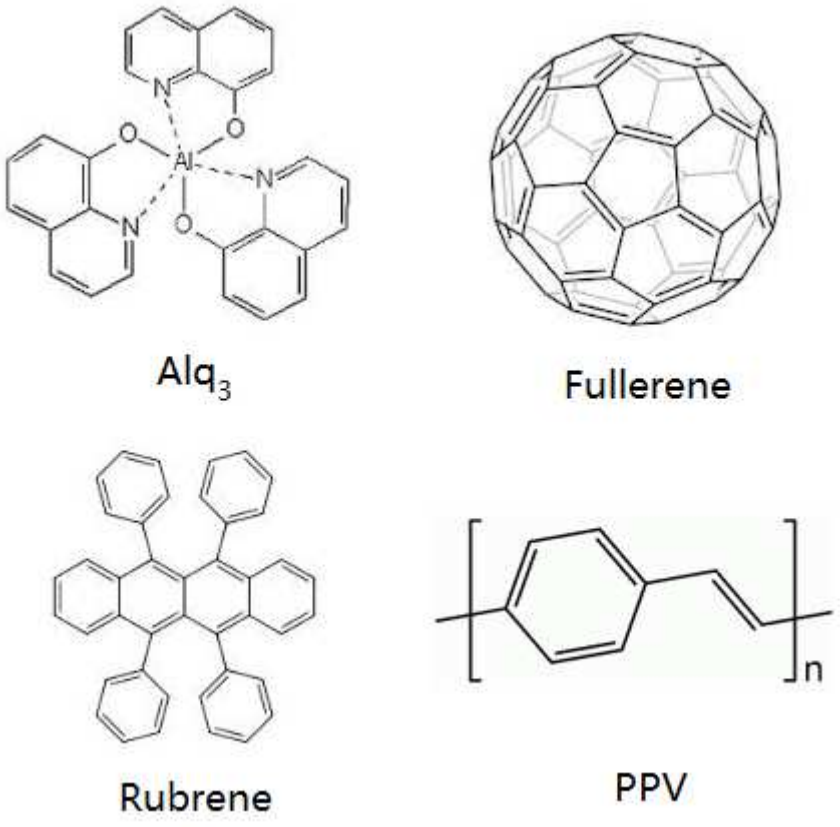

FIG. 1.4. Molecular structure of some typical organic semiconductors.

polymers and small molecules may be suitable for certain devices. Most of them have delocalized π-bonds. A few examples of the benchmark molecules are Tris(8-hydroxyquinolinato)aluminium (Alq_3),[19] fullerene,[20,21] rubrene,[22] and polyphenylene vinylene (PPV),[23] shown in FIG. 1.4. Compared to inorganic materials, a significant advantage of organics is that the material parameters such as band gap, energy levels, and carrier mobilities are tunable over a wide range.

The charge transport mechanism in organic semiconductors is different from that in conventional inorganic materials.[24,25] From a microscopic point of view, the carriers in conventional semiconductors typically move ballistically in a periodic atomic lattice over distances that are long compared to the lattice constant. This may be called "band transport". In many organic semiconductors, on the other hand, carriers are localized and "hopping" is the dominant transport mechanism. Therefore, the macroscopic mobility exhibits different dependence on device parameters such as the electric field and temperature.[26-29] Electrons and holes reside on host molecules and interact with their local environment forming polarons. Excitons in organic semiconductors are mostly of Poole-Frenkel type while those in inorganic semiconductors are typically of Wannier-Mott type. Compared to their inorganic counterparts, the excitons in organic semiconductors have large binding energy and are more localized. Moreover, organic semiconductors usually have a larger band gap and smaller band widths. In most devices the morphology of an organic material is an amorphous thin film, except in some OFETs single crystals are used for better mobility.[30] Because of these unique properties, the

device physics in organics shows distinct features, such as the commonly observed Langevin recombination and space charge effects.[31-33]

In order to build a functional device, different materials must be combined in a suitable configuration. The interface of two organic materials forms a heterojunction. For OLEDs and OPCs, a planar heterostructure is commonly used to enable device performance, and it is also a fundamental basis to study more advanced device configurations such as graded or bulk heterojunctions. For OFETs, we endow the term "heterojunction" with a more general meaning in this dissertation, which also includes the interface between an organic semiconductor (where the conduction channel is formed) and an organic ionic liquid (which behaves as a dielectric layer).

A typical device structure of an OLED or an OPC is shown in FIG. 1.5. From a viewpoint of energy conversion, in OLEDs energy is converted from electricity to light, while OPCs convert energy from light to electricity. Typically a device is composed of

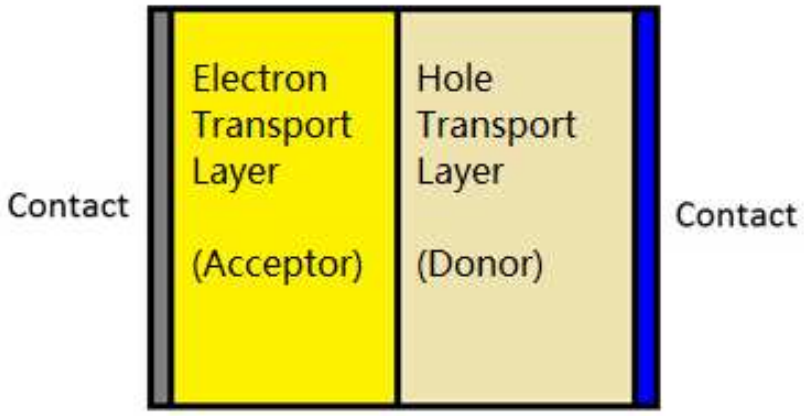

FIG. 1.5. Schematic device structure of typical OLEDs and OPCs

two organic layers of different materials. One is named the electron transport layer or acceptor active layer; it can support good electron transport (large electron mobility). The other is called the hole transport layer or donor active layer, supporting hole transport (large hole mobility). At the interface of the two layers a heterojunction is formed. The energy level alignment at the heterojunction is carefully designed such that both electrons and holes see an energy barrier when crossing the interface. The contact materials are also selected to facilitate electron/hole injection/collection at corresponding contacts. In OLEDs, when a forward bias is applied, electrons and holes are injected into the corresponding transport layers and move towards the interface, where they may subsequently get across the interface, recombine, and form excited states called excitons; or they may form excited states directly at the interface, called exciplexes. Excitons or exciplexes then may relax to the ground state by giving off photons. The interfacial enengy barrier prevents carriers from traversing the interface and improves recombination. In OPCs, when the device is under illumination, excitons are generated throughout the device. Due to the large binding energy, excitons do not dissociate unless

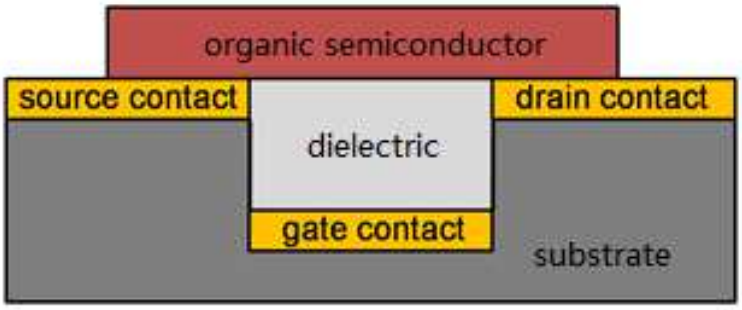

FIG. 1.6. Schematic device structure of typical OFETs

they are very close to the interface, where the energy offset helps exciton dissociation into electron and hole polarons. The electrons and holes are subsequently collected by the contacts due to the internal electric field and an electric current is formed.

A schematic device structure of an OFET is shown in FIG. 1.6. The device is similar to a conventional MOSFET with gate, source, and drain terminals. The differences are: 1) the structure of an OFET can either be a "top-gated", which is similar to a conventional MOSFET, or, more commonly, "bottom-gated", where the gate contact is usually deposited on the substrate at the bottom while the organic semiconductor forming conduction channel is on top; 2) in conventional MOSFETs the gate dielectric is usually a thin layer of thermally-grown SiO_2, while in OFETs the dielectric is typically of much larger thickness and consists of other materials such as conventional insulators or ionic liquids. The operating mechanism of OFETs and conventional MOSFETs has similarity in that they both use a gate voltage to control the conduction channel between the source and drain terminals. The difference is that there is typically no 'inversion layer' in OFETs as organic semiconductors are generally undoped.

There are many fabrication techniques for organic-based devices such as spin-coating,[7,8] ink-jet printing,[34,35] and roll-to-roll printing[36]. Although stability has been a major problem for many of these devices, device engineers are making improvements through encapsulation.[37-39]

Another emerging field based on organic devices is organic spintronics.[40-42] Organic semiconductors have advantages for spintronic applications due to the weak spin-orbit interaction of light atoms (C, H, O, etc.), leading to long spin coherence times.

Recently, researchers studied spin injection and transport for organic devices,[43-47] and spintronic properties such as magnetoelectroluminescence and magnetoconductance may also help to improve the efficiencies of OLEDs.

1.2 Objective of the work and organization of the thesis

The objective of this thesis is to provide contributions to the organic electronics community from a theoretical point of view. By developing various theoretical models we not only arrive at a better and deeper understanding of the device physics, but also provide reasonable options to improve the device efficiency.

Although much experimental work on OLEDs and OPCs has been presented, the importance of corresponding theoretical research should not be underestimated. We note the fact that OLEDs and OPCs are structurally very similar. Therefore we aim at developing one unified device model that can describe both types of devices. In the model discussed in chapter 2, we aim at combining the complicated microscopic processes at the heterojunction interface with bulk transport and carrier injection from the contacts. Subsequently by using the model, we study detailed properties of the devices. By choosing appropriate kinetic parameters for the microscopic processes we are able to simulate both OLED and OPC devices. Example results for electrostatics, charge and exciton profiles, and current-voltage relations are presented. Key results of this chapter have been published in Journal of Applied Physics and Applied Physics Letters.[48-50]

Chapter 3 is about an application of the device model presented in Chapter 2. We study the physics determining the OPC efficiency and improve it by inserting a thin tunnel barrier between the donor and acceptor layers. The microscopic processes associated with the interface are controlled and analyzed. Our theoretical work explains the physical mechanism behind recent experimental observations. Both short-circuit current and open-circuit voltage can be improved using this technique. The work in this chapter provides generic guidelines for improving the efficiency of OPCs and has been published mostly in Journal of Applied Physics.[51-54]

In chapter 4, we discuss theoretical work on magnetoelectroluminescence in OLEDs. Recent experiments have shown that the electroluminescence in an OLED can be improved by an external magnetic field. We aim at developing an analytical theory describing the device physics. The effect of hyperfine and Zeeman interactions, and different types of spin correlation functions on the device's optoelectric properties are shown. The microscopic process concepts for OLEDs discussed in chapter 2 are applied. The work in this chapter has been published in Physical Review B and Applied Physics Letters.[55,56]

Chapter 5 is about OFETs models. Recently an ionic liquid has been employed as the dielectric layer in OFETs between the gate and the conduction channel, improving the channel carrier density and reducing the operating voltage. This specific type of OFET is called an electric double layer transistor (EDLT). Due to the relatively large capacitance at the semiconductor/ionic liquid interface and the relatively low charge carrier mobility in organic semiconductors, there exists a coupling effect between the channel

conductance and the gate-to-channel capacitance. This coupling is a unique property of organic-based field effect transistors with an ionic liquid dielectric material. It is explained by a simple yet physical equivalent circuit model, and the results have been published in Applied Physics Letters.[57]

In chapter 6 we summarize the thesis and give suggestions for future work. Also other topics that I have been working on or involved in during my Ph.D. at University of Minnesota are outlined briefly.[58-64]

Chapter 2 Device model for organic bilayer heterojunction devices

2.1 Introduction

As discussed in chapter 1, in order to enable device performance and efficiency of OLEDs and OPCs, two or more different organic semiconductors are often employed in planar stacked structures or as bulk heterojunctions.[65-68] The electronic properties at the interface are complicated because the chemical composition changes sharply from one material to the other, therefore the electronic structure, the mobility, and the carrier concentration vary strongly in this region. The interface properties are complicated further by interfacial states, which are sensitive not only to the specific types of materials, but also to the detailed synthesis and fabrication techniques. The interface is of great importance for device performance. For example, interfaces can block the transport of electrons and/or holes, increasing the probability for exciton formation in an OLED. In an OPC the interface enables the dissociation of excitons generated by light. In this chapter, we propose a device model aimed at understanding the interface-related physics and its consequences for different device applications. To be specific, we explore a simple bilayer structure composed of an electron transport layer (ETL) and a hole transport layer (HTL), with the convention that the energies of both the highest occupied molecular orbital (HOMO) and the lowest unoccupied molecular orbital (LUMO) in the ETL are lower than in the HTL. C_{60} and tetracene form a representative pair of materials.

The chapter is organized as follows: in section 2.2 we discuss the microscopic processes at the heterojunction interface, such as interfacial exciton formation/ dissociation, exciplex formation/dissociation, and geminate/nongeminate recombination. Then we develop suitable device equations and interface parameters. In section 2.3 we perform calculations relevant for different device applications, such as an OLED with exciton or exciplex emission, and an OPC with or without geminate recombination. We discuss the results and explore the effects of the mechanisms at the interface. In section 2.4 we present conclusions.

2.2 Model construction

2.2.1 Microscopic processes

Before discussing the model, it is necessary to define two fundamental terms: the bulk region and the interface region. The two types of regions are defined by the environments that a particle (electron, hole, exciton, etc.) experiences. In the bulk regions, the materials have non-varying chemical compositions. These regions include most of the ETL and the HTL of the structure. In the interface region, there is a transition in chemical composition from one material to the other. The interface region is not a simple ideal boundary between the two layers. Lack of perfect control over the fabrication processes gives rise to an interface region with thickness $2\Delta L$. Much of the

model construction will concentrate on the interface region. However, we will first discuss the bulk region where the microscopic processes are simpler.

In the bulk region, when an electron and a hole are located on the same molecule, they constitute a correlated electron-hole pair due to their mutual Coulomb attraction, which leads to the formation of an excited molecular state called an exciton. Excitons in organic semiconductors are of Frenkel type and usually have a large binding energy (~ 0.5 eV).[69] Because both electrons and holes are spin 1/2 particles, the excitons can be either in a singlet state (total spin = 0) or one of three triplet states (total spin = 1). If the spin-orbit interaction is negligible, optical transitions between the excitons and the molecular ground state are possible only for singlet excitons.

FIG 2.1 shows a schematic representation of the microscopic processes in the bulk region. An electron and a hole on the same molecule can form an exciton, the rate of this process is proportional to both the electron density n and the hole density p. As

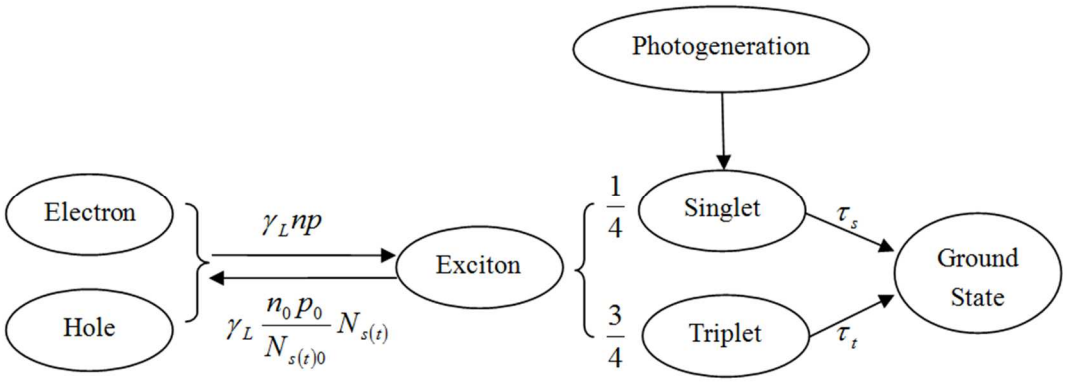

FIG 2.1. Schematic representation of microscopic processes in the bulk region.

the mobilities in organic semiconductors are low, the rate constant γ_L is assumed to be of Langevin form: $\gamma_L = e\,(\mu_n + \mu_p) / \varepsilon$,[70] where e is the magnitude of the electron charge, ε is the dielectric constant, and μ_n and μ_p are the electron and hole mobilities. This form of recombination implies that the process is limited by the transport of electrons and holes to the particular molecule where the exciton is formed rather than by the local exciton formation rate. In the simplest case, if the electrons and holes are not polarized, a quarter of the excitons formed are singlets with a density N_s and three quarters are triplets with a density N_t. An exciton can diffuse within the same material, the diffusivities for singlets and triplets are D_s and D_t, respectively. An exciton can also dissociate into an electron and a hole, and the rate is proportional to the exciton density N_s or N_t. However, due to the large binding energy of excitons, dissociation is very difficult in the bulk region. In equilibrium, detailed balance applies, therefore the singlet (triplet) exciton dissociation rate can be written as $\gamma_L n_0 p_0 N_{s(t)} / N_{s0(t0)}$, where n_0 and p_0 are the equilibrium densities of electrons and holes, and $N_{s0(t0)}$ are the equilibrium densities of singlet (triplet) excitons. When the device is under illumination singlet excitons can be generated by photons. The generation rate, denoted by G_l, depends on the light intensity, wavelength, and the absorption coefficient of the material. Singlet and triplet excitons can relax to the ground state, with relaxation lifetimes τ_s and τ_t. The relaxation process of triplet excitons can only be nonradiative, and they therefore usually have long lifetimes.

A staggered alignment of the HOMO and LUMO levels, with higher energies in the HTL, is envisioned. In the interface region we will focus on the following important

processes: exciton formation/dissociation, exciplex formation/dissociation, and recombination.

Under forward bias, injected electrons accumulate on the ETL side of the interface and injected holes accumulate on the HTL side. If the energy barriers are high, both electrons and holes will reach high densities in close proximity to each other and exciton formation processes can occur.[71] As shown in FIG. 2.2, an electron may transfer across the interface by a thermally activated process or by tunneling and join a hole in the HTL, which leads to the formation of an exciton in the HTL. The same procedures can

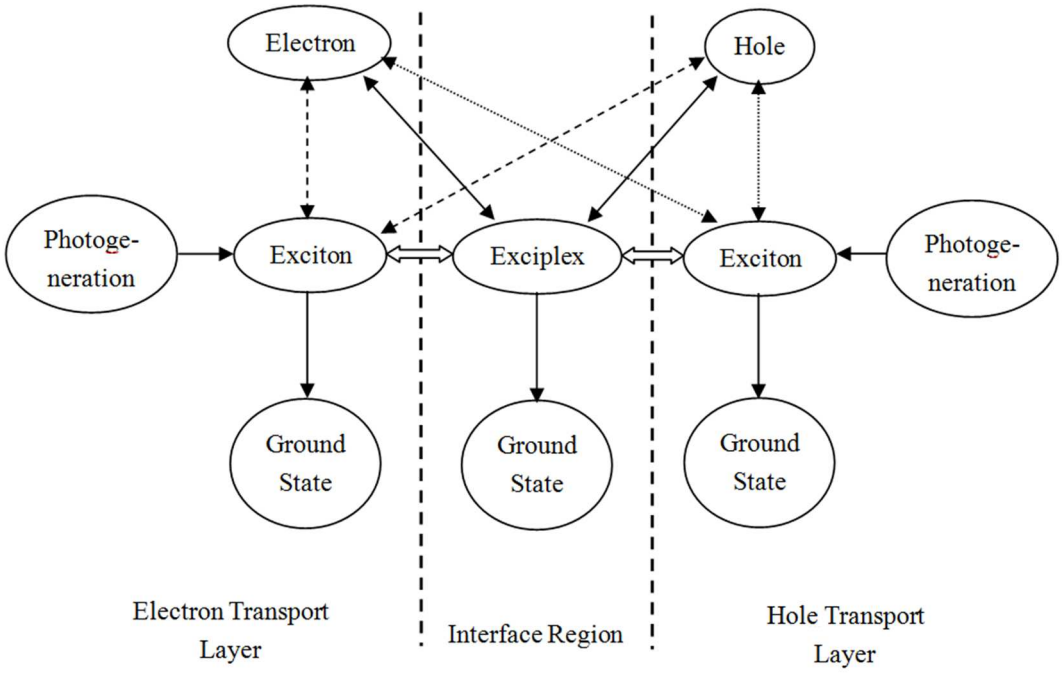

FIG. 2.2. Schematic representation of microscopic processes in and around the interface region.

apply to a hole, which can overcome the interface barrier, join an electron, and form an exciton in the ETL. The reverse process is exciton dissociation. An exciton that reaches the interface region may dissociate into an electron in the ETL and a hole in the HTL due to the difference in chemical potential in the two layers. The dissociation process is significant under illumination when there are excess excitons due to their generation by light absorption.

In the interface region there exists a sharp transition in the energy levels. Electrons (holes) have lower energy in the ETL (HTL) than in the HTL (ETL) due to the lower LUMO (HOMO) levels. Therefore, an intermolecular excited state may form across the interface involving an electron on an ETL molecule and a hole on an adjacent HTL molecule. This excited state of a pair of molecules is called an exciplex (or a charge transfer state).[72-74] The exciplex has lower energy than the bulk excitons, and it is immobile in the direction perpendicular to the interface. Similar to bulk excitons, an exciplex can be either in a singlet or triplet state. An exciplex can relax to the ground state or dissociate into an electron in the ETL and a hole in the HTL.

Another important process is geminate recombination.[75,76] A bulk exciton at the interface may dissociate into a correlated electron-hole pair, with the electron located on an ETL molecule and the hole on an adjacent HTL molecule. Either or both of the carriers may subsequently move away from the interface. However, it is also possible that the correlated state (exciplex) relaxes to the ground state. This will be referred to as geminate recombination. The overall process can be viewed as an exciton transforming

into an exciplex, which then recombines. Through the time-reversed process, an exciplex can also transform into an exciton.

The microscopic processes at the interface are summarized in FIG. 2.2. To build a macroscopic device model it is necessary to specify the kinetic coefficients for formation/dissociation rates. Analogous to the bulk, the exciton formation rate at the interface can be written as $\delta(x)\gamma_{ext}np$. $\delta(x)$ is the Dirac delta function, which limits the exciton formation to within the interface region, γ_{ext} is the exciton formation coefficient. To allow for a non-abrupt interface, an asymptotic approximation of the delta function is used. The origin is set at the nominal interface ($x = 0$), thus the ETL (HTL) are at $x < 0$ ($x > 0$). Bulk exciton formation is a local process, the rate depends on the electron and hole density at the same position. Interface exciton formation is a non-local process, the rate depends on the product of electron density in the ETL and the hole density in the HTL, $n_{-\Delta L}p_{\Delta L}$. This process annihilates an electron at $x = -\Delta L$ (the boundary of the ETL) and a hole at $x = \Delta L$ (the boundary of the HTL), and generates an exciton either at $x = -\Delta L$ or $x = \Delta L$. The exciton formation rates at $x = -\Delta L$ and $x = \Delta L$ may be different, hence we need to consider the two cases separately. (a) Exciton formation in the ETL at $x = -\Delta L$: In this case the electron annihilation rate at position x can be written as $\delta(x+\Delta L)\gamma_{ext}^{-}n_x p_{-x}$, where the peak of the expression is located at $x = -\Delta L$; the hole annihilation rate at position x can be written as $\delta(x-\Delta L)\gamma_{ext}^{-}n_{-x}p_x$, with the peak located at $x = \Delta L$. The exchange of subscripts for n and p ensures that the peak values of both rates are proportional to $\gamma_{ext}^{-}n_{-\Delta L}p_{\Delta L}$, therefore the particles taking part in the process are the majority carriers (electrons in the ETL and holes in the HTL). (b) Exciton formation

in the HTL at $x = \Delta L$: Here the electron and hole annihilation rates can be written as $\delta(x+\Delta L)\gamma_{ext}^{+} n_x p_{-x}$ and $\delta(x-\Delta L)\gamma_{ext}^{+} n_{-x} p_x$, respectively. Due to the conservation of particles (one electron and one hole form one exciton), the exciton formation rate is equal to the corresponding electron or hole annihilation rate.

The exciton dissociation rate is proportional to the exciton density. Analogous to the bulk recombination with detailed balance at equilibrium, the singlet (triplet) exciton dissociation rates can be written as $\delta(x+\Delta L)\gamma_{ext}^{-} \frac{n_{0,-\Delta L} p_{0,\Delta L}}{N_{s0(t0),-\Delta L}} N_{s(t),x}$ (for the ETL at $x = -\Delta L$) and $\delta(x-\Delta L)\gamma_{ext}^{+} \frac{n_{0,-\Delta L} p_{0,\Delta L}}{N_{s0(t0),\Delta L}} N_{s(t),x}$ (for the HTL at $x = \Delta L$). These are also the rates for the corresponding electron and hole generation.

As exciplexes only exist in the interface region it is more appropriate to model the exciplex density as a two-dimensional sheet density. The exciton formation rates depend on position x. They have a double peak at $x = -\Delta L$ and $x = \Delta L$ and are essentially zero elsewhere. The exciplex formation rates are independent of x in the interface region because the exciplex densities are sheet densities independent of position. On the other hand, the electron and hole annihilation involved in this process depends on position. The electrons at $x = -\Delta L$ and the holes at $x = \Delta L$ make the largest contributions to exciplex formation. The contributions drop sharply away from $x = \pm\Delta L$. Therefore, the exciplex formation rates can be modeled as $\gamma_{\exp} \int n_x p_{-x} \delta(x+\Delta L) dx$ or $\gamma_{\exp} \int n_{-x} p_x \delta(x-\Delta L) dx$. γ_{exp} is the exciplex formation coefficient. These two expressions are equivalent if we change the integration variable from x to $-x$, with the assumption that

the total thickness of the device is much greater than the thickness of the interface region. The electron and hole annihilation rates can be described by the exciplex formation rates multiplied by the corresponding delta functions, which can be written as $\delta(x+\Delta L)\gamma_{\exp}\int n_x p_{-x}\delta(x+\Delta L)dx$ (for electrons in the ETL) and $\delta(x-\Delta L)\gamma_{\exp}\int n_{-x} p_x\delta(x-\Delta L)dx$ (for holes in the HTL), respectively. Similarly, the rates of the reverse process, exciplex dissociation, can be obtained from detailed balance in equilibrium: $\gamma_{\exp}\frac{n_{0,-\Delta L}p_{0,\Delta L}}{N^{(2)}_{\exp,s0(t0)}}N^{(2)}_{\exp,s(t)}$, where $N^{(2)}_{\exp,s(t)}$ is the two-dimensional singlet (triplet) exciplex density, and $N^{(2)}_{\exp,s0(t0)}$ is the singlet (triplet) exciplex density in equilibrium. The corresponding electron and hole generation rates can be obtained in the same way by multiplying with the corresponding delta functions, yielding $\delta(x+\Delta L)\gamma_{\exp}\frac{n_{0,-\Delta L}p_{0,\Delta L}}{N^{(2)}_{\exp,s0(t0)}}N^{(2)}_{\exp,s(t)}$ (for electrons in the ETL) and $\delta(x-\Delta L)\gamma_{\exp}\frac{n_{0,-\Delta L}p_{0,\Delta L}}{N^{(2)}_{\exp,s0(t0)}}N^{(2)}_{\exp,s(t)}$ (for holes in the HTL).

As geminate recombination can be viewed as the transformation from excitons to exciplexes, the rate is proportional to the density of excitons. The excitons located at $x = \pm\Delta L$ have maximum probability for this process, and at other positions the probability essentially vanishes. Similar to the exciplex formation/dissociation processes, the rates of exciplex formation can be written as $\gamma^{-}_{ger,s(t)}\int N_{s(t)}\delta(x+\Delta L)dx$ (for the transfer of singlet (triplet) excitons at $x = -\Delta L$) and $\gamma^{+}_{ger,s(t)}\int N_{s(t)}\delta(x-\Delta L)dx$ (for the transfer of singlet (triplet) excitons at $x = \Delta L$). Furthermore, the rates for exciton density decrease

can be written as $\delta(x+\Delta L)\gamma^{-}_{ger,s(t)}\int N_{s(t)}\delta(x+\Delta L)dx$ for singlet (triplet) excitons in the ETL, and $\delta(x-\Delta L)\gamma^{+}_{ger,s(t)}\int N_{s(t)}\delta(x-\Delta L)dx$ for singlet (triplet) excitons in the HTL. The rates of the reverse processes are obtained by detailed balance. The rate of exciplex to exciton transfer at $x = -\Delta L$ is $\gamma^{-}_{ger,s(t)}\frac{N_{s0(t0),-\Delta L}}{N^{(2)}_{\exp,s0(t0)}}N^{(2)}_{\exp,s(t)}$, and the rate at $x = \Delta L$ is $\gamma^{+}_{ger,s(t)}\frac{N_{s0(t0),\Delta L}}{N^{(2)}_{\exp,s0(t0)}}N^{(2)}_{\exp,s(t)}$. The rate of exciton formation in the ETL is $\delta(x+\Delta L)\gamma^{-}_{ger,s(t)}\frac{N_{s0(t0),-\Delta L}}{N^{(2)}_{\exp,s0(t0)}}N^{(2)}_{\exp,s(t)}$, and the rate in the HTL is $\delta(x-\Delta L)\gamma^{+}_{ger,s(t)}\frac{N_{s0(t0),\Delta L}}{N^{(2)}_{\exp,s0(t0)}}N^{(2)}_{\exp,s(t)}$.

In summary, each microscopic process has two directions. For example, an electron and a hole can form an exciton, and an exciton can dissociate into an electron and a hole. The charge and particle conservation laws ensure that the rates of electron annihilation, hole annihilation and exciton formation are the same. For the exciplex-related process, the rate of electron (hole, exciton) annihilation integrated over the entire device is equal to the rate of exciplex formation. When the balance is perturbed due to carrier injection or photon-induced exciton formation, the processes in one direction will dominate over the reverse processes, and the corresponding densities will increase or decrease. The change in particle densities will reduce the rates of the dominant processes and increase the rates of the reverse processes until a new steady state is reached. For example, when a forward bias is applied, electrons and holes are injected into the device. The exciton formation rate increases and dominates over the exciton dissociation rate. As

a result, the electron and hole densities decrease and the exciton density increases. A new steady state is established with the electron, hole, and exciton densities different from equilibrium.

The microscopic processes discussed above have shown their importance in the operation of various devices. In the following a few examples are considered and the working mechanisms are briefly described.

OLEDs with light generation from exciton emission:[7,65] In this type of device energy from an electrical bias is converted into light. The device is working under a forward voltage bias. Electrons and holes are injected from cathode and anode contacts, respectively. They migrate toward the interface and form excitons. The excitons then diffuse into either of the ETL or HTL material, and then decay to the ground state radiatively or nonradiatively. A radiative decay generates a photon.

OLEDs with light generation from exciplex emission:[77,78] The working mechanism is similar to the device above. The main difference is that due to the properties of the materials, electrons and holes at the interface are more likely to form exciplexes. Exciplexes can then decay radiatively or nonradiatively, and light is obtained from the radiative decay.

OPCs with nongeminate recombination:[67,79] The aim of photovoltaic devices is to convert incident light into electrical energy. Through the absorption of photons, singlet excitons are generated. When they diffuse to the interface the excitons may dissociate into electrons in the ETL and holes in the HTL. Electrons and holes then may move to the corresponding contacts, producing current.

OPCs with geminate recombination:[80,81] In photovoltaic cells it is common that both the nongeminate process and the geminate process coexist. Some excitons at the interface may convert into exciplexes (charge-transfer states), which may relax to the ground state. Because of the geminate process, the exciton density decreases at the interface and consequently exciton dissociation is reduced. Hence, photocurrent is reduced and the device efficiency is degraded. More discussion on this topic is presented in chapter 3.

2.2.2 Device model

In this part the formulas for the processes discussed are incorporated into a set of one-dimensional device equations. The device model framework for the bulk region is discussed first.[82,83] Next, based on the discussion of the interfacial processes, the equations for the bulk region are extended to include the interface region.

In the bulk region, the transport of electrons, holes, singlet and triplet excitons are described by the following time-dependent rate equations:

$$\frac{\partial n}{\partial t} = \frac{1}{e}\frac{\partial J_n}{\partial x} - GR_s - GR_t \tag{2.1a}$$

$$\frac{\partial p}{\partial t} = -\frac{1}{e}\frac{\partial J_p}{\partial x} - GR_s - GR_t \tag{2.1b}$$

$$\frac{\partial N_s}{\partial t} = -\frac{\partial J_{Ns}}{\partial x} + GR_s - \frac{(N_s - N_{s0})}{\tau_s} + G_l \tag{2.1c}$$

$$\frac{\partial N_t}{\partial t} = -\frac{\partial J_{Nt}}{\partial x} + GR_t - \frac{(N_t - N_{t0})}{\tau_t} \tag{2.1d}$$

where J_n (J_p) is the electron (hole) charge current, J_{Ns} (J_{Nt}) is the singlet (triplet) exciton flux, GR_s (GR_t) is the singlet (triplet) exciton generation and recombination rate in the bulk region (it is also the electron/hole annihilation and generation rate), G_l is the photogeneration rate.

According to the discussion in section 2.2.1, the generation and recombination rate in the bulk region is a combination of both forward and reverse processes:

$$GR_s = \frac{1}{4}\gamma_L\left(np - \frac{n_0 p_0}{N_{s0}} N_s\right) \tag{2.2a}$$

$$GR_t = \frac{3}{4}\gamma_L\left(np - \frac{n_0 p_0}{N_{t0}} N_t\right) \tag{2.2b}$$

The charge current is composed of drift and diffusion components:

$$J_n = e\mu_n\left(nE + \frac{kT}{e}\frac{\partial n}{\partial x}\right) \tag{2.3a}$$

$$J_p = e\mu_p\left(pE - \frac{kT}{e}\frac{\partial p}{\partial x}\right) \tag{2.3b}$$

E is the electric field, μ_n (μ_p) is the electron (hole) mobility. To limit the number of variables, the mobility is taken to be independent of electric field, but it is easy to incorporate the field dependence of the mobility into the model.[84] k is Boltzmann's constant, T is the temperature, and the diffusivities have been written in terms of the mobilities using the Einstein relation.

Excitons are chargeless particles, therefore the exciton flux contains only a diffusion term:

$$J_{Ns} = -D_s \frac{\partial N_s}{\partial x} \tag{2.4a}$$

$$J_{Nt} = -D_t \frac{\partial N_t}{\partial x} \tag{2.4b}$$

D_s (D_t) is the diffusivity of singlet (triplet) excitons.

The electron and hole densities are related to the molecular density N_m and the electrostatic potential ϕ by non-degenerate statistics. Poisson's equation is coupled to the rate equations above. The boundary conditions for electrons and holes at the contacts are thermionic emission and backflow recombination, incorporating image charge induced barrier lowering. Tunneling effects at the contacts are not included because the model is intended to work in the low voltage regime (< 5 V) and charge injection barriers are not high (< 1 eV). Hence, tunnel injection can be neglected.[82] The exciton densities at the contacts are fixed at the equilibrium values. The equilibrium exciton density is determined by the molecular density and the singlet (triplet) exciton energy $E_{s(t)}$:

$$N_{s0(t0)} = N_m \exp\left(-\frac{E_{s(t)}}{2kT}\right) \tag{2.5}$$

Following the discussion of section 2.2.1, the interface region is treated in the framework of a one-dimensional continuum model. The principal motivation for this approach is numerical efficiency. However, the continuum model can also be thought of as a macroscopic description that averages over microscopic disorder at the interface, i.e. local fluctuations in chemical composition or interface roughness. The change in

chemical composition is described by a hyperbolic tangent function that has a transition region width on the order of or less than molecular dimensions. We assume that the change in device parameters scales linearly with the chemical composition. For example, the HOMO energy level as a function of position is described as:

$$HOMO(x) = \frac{1}{2}\left[\tanh\left(\frac{x}{\Delta L}\right)\left(HOMO_{HTL} - HOMO_{ETL}\right) + \left(HOMO_{HTL} + HOMO_{ETL}\right)\right] \quad (2.6)$$

The interface region thickness $2\Delta L$ is adjustable and typically is much smaller than the total thickness of the device. The width is chosen sufficiently small that further reductions do not change the calculated device characteristics. From equation (2.6), in the ETL at $x << -\Delta L$, $\tanh(x/\Delta L) \approx -1$, therefore $HOMO(x) \approx HOMO_{ETL}$; in the HTL at $x >> \Delta L$, $\tanh(x/\Delta L) \approx 1$, therefore $HOMO(x) \approx HOMO_{HTL}$; In the interface region the HOMO level varies smoothly between $HOMO_{ETL}$ and $HOMO_{HTL}$. Other material parameters are taken to obey the same type of formula.

The asymptotic form of the $\delta(x)$ function used for interface microscopic processes is the derivative of the hyperbolic tangent function, with the appropriate normalization.

$$\delta(x) \to \frac{1}{2\Delta L\left[\cosh(x/\Delta L)\right]^2} \quad (2.7)$$

The interface exciton formation/dissociation terms can be incorporated into the device equations (2.1) as follows. Excitons can be formed/dissociated in both ETL and HTL, but electrons can only be annihilated/generated in the ETL and holes can only be annihilated/generated in the HTL.

The net rate of electron annihilation in the ETL (peak at $x = -\Delta L$) and exciton generation in the ETL (peak at $x = -\Delta L$) is given by:

$$\delta(x+\Delta L)GR^{-}_{ext,s(t)}(x)=\delta(x+\Delta L)\gamma^{-}_{ext,s(t)}\left(n_x p_{-x}-\frac{n_{0,-\Delta L}p_{0,\Delta L}}{N_{s0(t0),-\Delta L}}N_{s(t),x}\right) \quad (2.8a)$$

If the net rate is positive, the interface exciton formation dominates over the exciton dissociation; if the net rate is negative, exciton dissociation is dominant.

Similarly, the net rate of electron annihilation in the ETL and exciton formation in the HTL (peak at $x = \Delta L$) is:

$$\delta(x+\Delta L)GR^{+}_{ext,s(t)}(x)=\delta(x+\Delta L)\gamma^{+}_{ext,s(t)}\left(n_x p_{-x}-\frac{n_{0,-\Delta L}p_{0,\Delta L}}{N_{s0(t0),\Delta L}}N_{s(t),-x}\right) \quad (2.8b)$$

The net rate of hole annihilation in the HTL and exciton formation in the ETL is:

$$\delta(x-\Delta L)GR^{-}_{ext,s(t)}(-x)=\delta(x-\Delta L)\gamma^{-}_{ext,s(t)}\left(n_{-x} p_{x}-\frac{n_{0,-\Delta L}p_{0,\Delta L}}{N_{s0(t0),-\Delta L}}N_{s(t),-x}\right) \quad (2.8c)$$

The net rate of hole annihilation in the HTL and exciton formation in the HTL is:

$$\delta(x-\Delta L)GR^{+}_{ext,s(t)}(-x)=\delta(x-\Delta L)\gamma^{+}_{ext,s(t)}\left(n_{-x} p_{x}-\frac{n_{0,-\Delta L}p_{0,\Delta L}}{N_{s0(t0),\Delta L}}N_{s(t),x}\right) \quad (2.8d)$$

Similarly, the exciplex formation and dissociation rates are described by the following equations. The net rate of electron annihilation in the ETL with exciplex formation is given by:

$$\delta(x+\Delta L)GR^{n}_{\exp,s(t)}=\delta(x+\Delta L)\gamma_{\exp,s(t)}\left(\int n_x p_{-x}\delta(x+\Delta L)dx-\frac{n_{0,-\Delta L}p_{0,\Delta L}}{N^{(2)}_{\exp,s0(t0)}}N^{(2)}_{\exp,s(t)}\right) \quad (2.9a)$$

The net rate of hole annihilation in the HTL with exciplex formation is given by:

$$\delta(x-\Delta L)GR^{p}_{\exp,s(t)}=\delta(x-\Delta L)\gamma_{\exp,s(t)}\left(\int n_{-x} p_{x}\delta(x-\Delta L)dx-\frac{n_{0,-\Delta L}p_{0,\Delta L}}{N^{(2)}_{\exp,s0(t0)}}N^{(2)}_{\exp,s(t)}\right) \quad (2.9b)$$

With the assumption that the thickness of the interface region is much smaller than the total thickness of the device, the integration in equation (2.9) can be extended over all x. From equation (2.9) and by changing the integration variables from x to $-x$ we obtain:

$$GR^{n}_{\mathrm{exp},s(t)} = GR^{p}_{\mathrm{exp},s(t)} = GR_{\mathrm{exp},s(t)} \tag{2.10}$$

As exciplexes are formed on molecules on both sides of the interface, the exciplex formation/dissociation is also limited by the sheet density of molecules. Assuming that each molecule provides one state available for an exciplex, the sheet density of exciplex states in the interface region is given by $N_m\Delta L$, and the fraction of available exciplex states is given by $\left(1-\frac{N^{(2)}_{\mathrm{exp},s}+N^{(2)}_{\mathrm{exp},t}}{N_m\Delta L}\right)$. Accounting for this effect the net exciplex formation/dissociation rate can be rewritten as:

$$\begin{aligned} GR_{\mathrm{exp},s(t)} = \gamma_{\mathrm{exp},s(t)}\Bigg[&\int n_x p_{-x}\delta(x+\Delta L)dx\left(1-\frac{N^{(2)}_{\mathrm{exp},s}+N^{(2)}_{\mathrm{exp},t}}{N_m\Delta L}\right) \\ &-\frac{n_{0,-\Delta L}p_{0,\Delta L}}{N^{(2)}_{\mathrm{exp},s0(t0)}}N^{(2)}_{\mathrm{exp},s(t)}\left(1-\frac{N^{(2)}_{\mathrm{exp},s0}+N^{(2)}_{\mathrm{exp},t0}}{N_m\Delta L}\right)\Bigg] \end{aligned} \tag{2.11}$$

The exciplex density in equilibrium is determined by the sheet molecular density at the interface and the singlet (triplet) exciplex energies $E_{exp,s(t)}$:

$$N_{\mathrm{exp},s0(t0)} = N_m\Delta L\exp\left(-\frac{E_{\mathrm{exp},s(t)}}{2kT}\right) \tag{2.12}$$

The rate of geminate recombination is described as follows. The net rate of exciton dissociation in the ETL and exciplex formation via geminate recombination is given by:

$$\delta(x+\Delta L)GR^{-}_{ger,s(t)} = \delta(x+\Delta L)\gamma^{-}_{ger,s(t)}\left(\int N_{s(t)}\delta(x+\Delta L)dx - \frac{N_{s0(t0),-\Delta L}}{N^{(2)}_{\exp,s0(t0)}} N^{(2)}_{\exp,s(t)}\right) \quad (2.13a)$$

The net rate of exciton dissociation in the HTL and exciplex formation via geminate recombination is given by:

$$\delta(x-\Delta L)GR^{+}_{ger,s(t)} = \delta(x-\Delta L)\gamma^{+}_{ger,s(t)}\left(\int N_{s(t)}\delta(x-\Delta L)dx - \frac{N_{s0(t0),\Delta L}}{N^{(2)}_{\exp,s0(t0)}} N^{(2)}_{\exp,s(t)}\right) \quad (2.13b)$$

In the interface region, the change in chemical composition leads to changes in the HOMO and LUMO levels. The derivatives give equivalent fields that are added to the electrostatic field. Therefore, the electric field should be modified and the overall effective fields that are seen by electrons and holes are given by:

$$E_e'(x) = E(x) + \frac{1}{e}\frac{d}{dx}LUMO(x) \quad (2.14a)$$

$$E_h'(x) = E(x) + \frac{1}{e}\frac{d}{dx}HOMO(x) \quad (2.14b)$$

E_e' and E_h' are the overall effective field for electrons and holes, respectively.

Excitons can diffuse within either material, but in this model it is impossible for them to diffuse across the interface, implying that the exciton diffusion decreases sharply and approaches zero in the interface region. Therefore the exciton diffusivities are modified as:

$$D_{s(t)}'(x) = \frac{1}{2}\left[\tanh\left(\frac{x}{\Delta L}\right)\left(D_{s(t),HTL} - D_{s(t),ETL}\right) + \left(D_{s(t),HTL} + D_{s(t),ETL}\right)\right] \times\left(1 - \frac{1}{[\cosh(x/\Delta L)]^2}\right) \quad (2.15)$$

Equations (2.6), (2.8), (2.11), (2.13), (2.14) and (2.15) summarize the interface properties. By incorporating them into equations (2.1), (2.3) and (2.4), we obtain a set of equations that are appropriate for all regions of the device:

$$\frac{\partial n}{\partial t} = \frac{1}{e}\frac{\partial J_n}{\partial x} - GR_s - GR_t - \delta(x+\Delta L)\left(GR^-_{ext,s}(x) + GR^+_{ext,s}(x) + GR^-_{ext,t}(x) + GR^+_{ext,t}(x) + GR_{\exp,s} + GR_{\exp,t}\right) \tag{2.16a}$$

$$\frac{\partial p}{\partial t} = -\frac{1}{e}\frac{\partial J_p}{\partial x} - GR_s - GR_t - \delta(x-\Delta L) \times \left(GR^-_{ext,s}(-x) + GR^+_{ext,s}(-x) + GR^-_{ext,t}(-x) + GR^+_{ext,t}(-x) + GR_{\exp,s} + GR_{\exp,t}\right) \tag{2.16b}$$

$$\frac{\partial N_s}{\partial t} = -\frac{\partial J_{Ns}}{\partial x} + GR_s - \frac{(N_s - N_{s0})}{\tau_s} + G_l + \delta(x+\Delta L)\left(GR^-_{ext,s}(x) - GR^-_{ger,s}\right) + \delta(x-\Delta L)\left(GR^+_{ext,s}(-x) - GR^+_{ger,s}\right) \tag{2.16c}$$

$$\frac{\partial N_t}{\partial t} = -\frac{\partial J_{Nt}}{\partial x} + GR_t - \frac{(N_t - N_{t0})}{\tau_t} + \delta(x+\Delta L)\left(GR^-_{ext,t}(x) - GR^-_{ger,t}\right) + \delta(x-\Delta L)\left(GR^+_{ext,t}(-x) - GR^+_{ger,t}\right) \tag{2.16d}$$

$$\frac{\partial N^{(2)}_{\exp,s}}{\partial t} = GR_{\exp,s} + GR^-_{ger,s} + GR^+_{ger,s} - \frac{(N^{(2)}_{\exp,s} - N^{(2)}_{\exp,s0})}{\tau_{\exp,s}} \tag{2.16e}$$

$$\frac{\partial N^{(2)}_{\exp,t}}{\partial t} = GR_{\exp,t} + GR^-_{ger,t} + GR^+_{ger,t} - \frac{(N^{(2)}_{\exp,t} - N^{(2)}_{\exp,t0})}{\tau_{\exp,t}} \tag{2.16f}$$

$$J_n = e\mu_n\left(nE_e' + \frac{kT}{e}\frac{\partial n}{\partial x}\right) \tag{2.17a}$$

$$J_p = e\mu_p\left(pE_h' - \frac{kT}{e}\frac{\partial p}{\partial x}\right) \tag{2.17b}$$

$$J_{Ns} = -D_s'\frac{\partial N_s}{\partial x} \tag{2.17c}$$

$$J_{Nt} = -D_t' \frac{\partial N_t}{\partial x} \tag{2.17d}$$

Equations (2.16e) and (2.16f) include the relaxation of exciplexes to the ground state. $\tau_{exp,s}$ and $\tau_{exp,t}$ are the singlet and triplet exciplex lifetimes, respectively.

A non-uniform discretization scheme is applied with a dense grid near the interface region. The Scharfetter-Gummel approach[85] is used to determine the current density. The time-dependent rate equations are integrated forward in time using Gear's method. To find the steady state solutions for a specified applied voltage, a time-dependent voltage ramp which stops at the desired voltage is applied to the right contact and the equations are time-integrated starting from thermal equilibrium until a steady state is reached. The criteria for steady state are that the left hand sides of equations (2.16) approach zero. To calculate the current-voltage characteristics a series of voltage ramps are applied. In performing the time integrations it is useful to have an explicit expression for the time dependence of the electric field at the left contact:[82]

$$\begin{aligned} \frac{\partial E(-L_1)}{\partial t} &= -\frac{1}{L}\frac{\partial \phi(L_2)}{\partial t} - \frac{4\pi}{\varepsilon_s}\left[J(-L_1) - \frac{1}{L}\int_{-L_1}^{L_2} J(x)dx \right] \\ &- \frac{4\pi e}{\varepsilon_s L}\int_{-L_1}^{L_2}\left(\int_{-L_1}^{x} \left(F(x') - F(-x')\right)dx' \right)dx \end{aligned} \tag{2.18}$$

where $F(x') = \delta(x'+\Delta L)\left(GR_{ext,s}^{-}(x') + GR_{ext,s}^{+}(x') + GR_{ext,t}^{-}(x') + GR_{ext,t}^{+}(x') + GR_{\exp,s} + GR_{\exp,t}\right)$.

L_1 is the thickness of the ETL and L_2 is the thickness of HTL. (L_1, L_2 >> ΔL) $L = L_1 + L_2$ is the total thickness of the device. $J = J_n + J_p$ is the total charge current. The electron injecting contact is at $x = -L_1$ and the hole injecting contact is at $x = L_2$. Equation (2.18)

comes from the time derivative of Poisson's equation. It is used to find $E(-L_1)$ to start the spatial integration of Poisson's equation at each new time step.

2.3 Results and discussion

2.3.1 Device parameters

To specify parameters for our calculations we assume that the material for the ETL is C_{60} and the material for the HTL is tetracene.[10,86] Both layers are 50 nm thick. Considerable work has been done previously regarding the material properties of C_{60}[87-93] and tetracene[86,94-98]. The band gaps used for the simulations are 2.5 eV (C_{60}) and 3.0 eV (tetracene).[86,88] The HOMO energy level is 6.2 eV for C_{60} and 5.4 eV for tetracene.[86,87] For C_{60} the singlet (triplet) exciton energy is 1.83 eV (1.55 eV).[89] For tetracene the singlet (triplet) exciton energy is 2.32 eV (1.25 eV).[94-96] The exciton relaxation lifetimes used for C_{60} are 16 ns (singlets) and 40 μs (triplets).[87,90,91] The exciton relaxation lifetimes used for tetracene are 0.1 ns (singlets) and 0.6 μs (triplets).[96,97] Various results for exciton diffusion lengths have been reported, [87,92,93,97,98] and we take the value of exciton diffusivities to be 1.56×10^{-7} cm^2/s for both singlets and triplets in C_{60}, 1.44×10^{-2} cm^2/s for singlets and 1.60×10^{-4} cm^2/s for triplets in tetracene. C_{60} and tetracene have comparable diffusion lengths, but as there is a longer relaxation lifetime in C_{60}, its

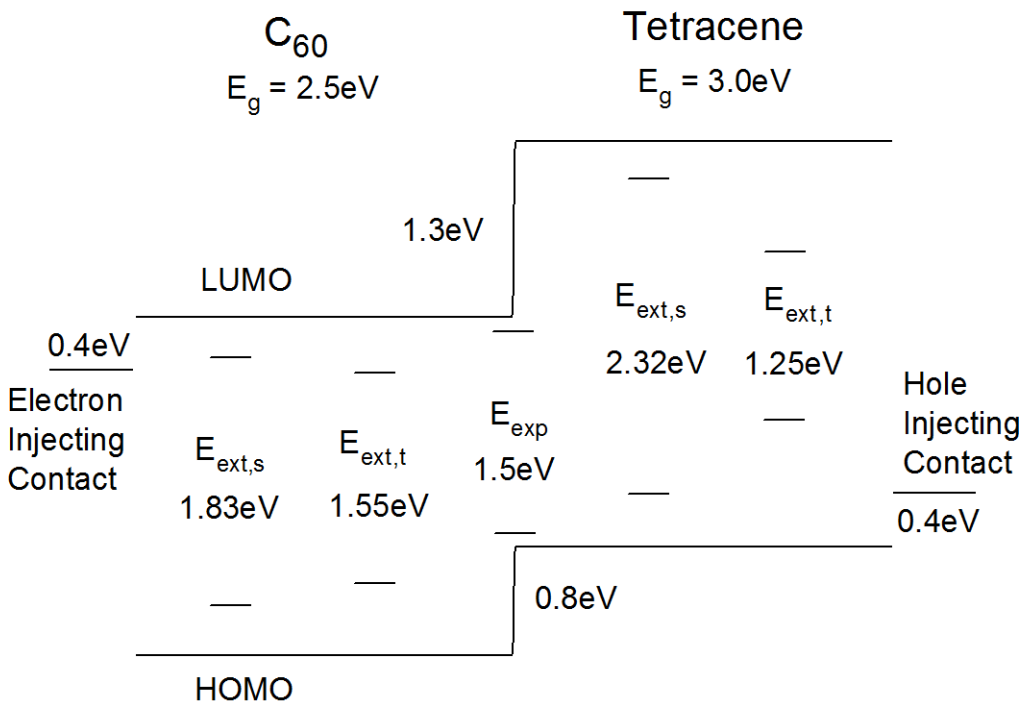

FIG. 2.3. Schematic band diagram with exciton and exciplex energies.

diffusivity is smaller. Singlet to triplet exciton transitions (intersystem crossing) in C_{60}[87] and exciton fission/fusion in tetracene[99] are not considered. Due to lack of data on the exciplex energies and lifetimes at the C_{60}/tetracene interface, both the singlet and triplet exciplex energies are taken to be 1.5 eV, and the exciplex lifetimes are assumed to be short enough (10^{-9} s) that exciplex accumulation is far from approaching the sheet molecular density limit. Due to the lack of detailed mobility data, we make a reasonable assumption that the ETL (HTL) C_{60} (tetracene) has an electron (hole) mobility of 10^{-2} $cm^2V^{-1}s^{-1}$ and a hole (electron) mobility of 10^{-6} $cm^2V^{-1}s^{-1}$. The molecular density N_m for both C_{60} and tetracene are taken to be 1.4×10^{21} cm^{-3}. Both the electron and hole injection contact barriers are taken to be 0.4 eV. For simplicity, the dielectric constant for both materials is taken to be 3. (Allowing for different dielectric constants is

relatively straightforward and this effect has been considered previously[83]). The calculations are done for room temperature. We assume that the two materials are nearly ideally separated with effective interface thickness parameter ΔL = 0.1 nm, which is smaller than the size of a molecule. These parameters are summarized in the schematic band diagram shown in FIG. 2.3.

In the following the fundamental device characteristics with no interface-related exciton or exciplex processes are first studied by discussing the profiles of the energy bands, electrostatic potential, electron and hole densities, singlet and triplet exciton densities under different applied biases. Subsequently, we introduce the interface processes and study the different roles they may play in device applications. We study the effect of interface exciton formation for OLEDs with exciton emission and the effect of exciplex formation for OLEDs with exciplex emission. Then we focus on OPCs and consider both nongeminate and geminate recombination.

2.3.2 General properties of bulk bilayer structure

The electrostatic potential, HOMO and LUMO energy level profiles at different applied voltages are shown in FIG. 2.4. The device built-in potential, V_{bi}, which is the difference between the energy levels of the electron and hole injecting contacts, is 0.9 V. When the applied voltage reaches V_{bi}, the total electrostatic potential drop across the device is zero and the HOMO and LUMO levels are flat. Under forward bias electrons travel from left to right and holes from right to left. Electrons and holes accumulate on

the two sides of the interface, and the applied voltage drops mainly across the interface region, as shown by the V = 1.5 V and V = 2.1 V cases in the figure. The electrons and holes form an interface dipole, which effectively lowers the interface barrier.[100] As the voltage continues to increase, the carrier accumulation increases and the barrier lowering continues until, at about V = 2.1 V, carriers start to overcome the barrier, and part of the voltage drops in the bulk region. The voltage drop and the carrier accumulation across the interface gradually saturate, as shown for V = 2.7 V. The inset figure shows the barrier lowering effect vs. applied voltage. For voltages smaller than V_{bi} the HOMO and LUMO offsets remain constant at 1.3 eV and 0.8 eV because there is no charge accumulation. At $V > V_{bi}$ the effective barrier decreases as the voltage increases. For sufficiently large voltage the charge accumulation and the effective barrier reduction gradually saturate.

FIG.2.5 shows the electron and hole density profiles. Only the electron density in the ETL and the hole density in the HTL are displayed, as the minority carrier densities

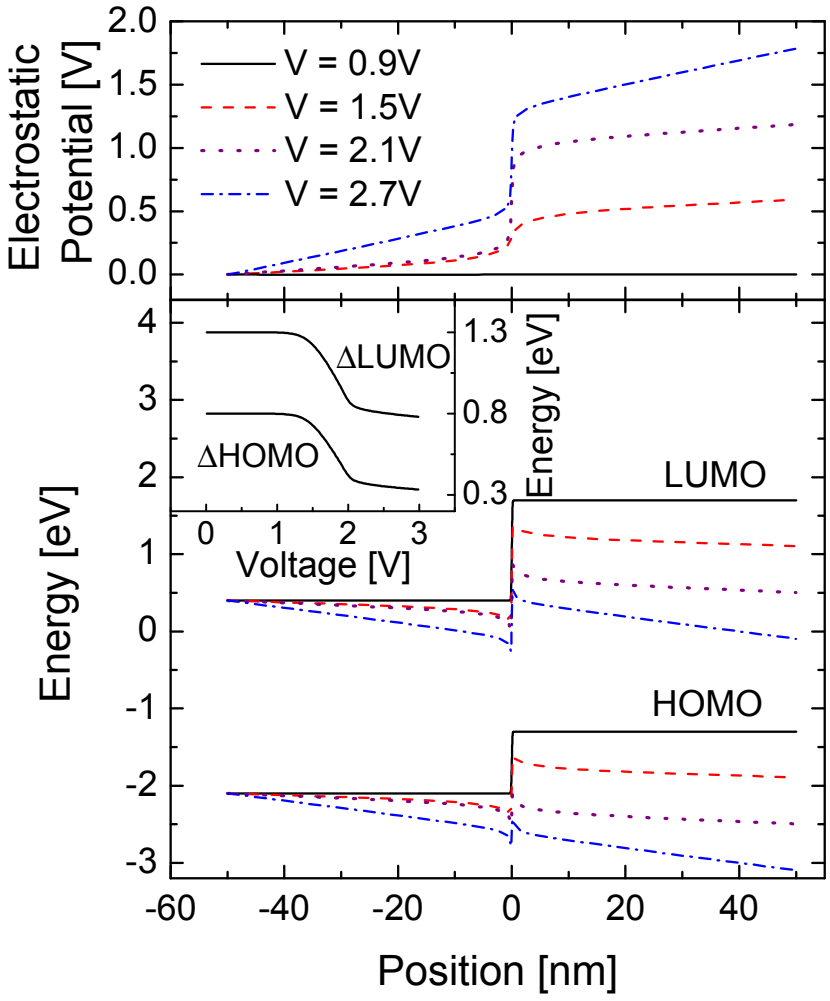

FIG. 2.4. Electrostatic potential, HOMO and LUMO energy level profiles at different applied voltages. The inset figure shows the dipole induced barrier lowering vs. voltage. are too small to be plotted on the same scale. At $V = V_{bi} = 0.9$ V, the device is at flatband and the electron and hole densities in the corresponding materials are position-independent. As the voltage increases, electrons and holes accumulate at the interface.

For the V = 2.7 V case, the electron density in the bulk ETL region decreases because some holes overcome the interface barrier and recombine with electrons.

FIG. 2.6 shows the exciton density profile for the voltages in FIGs. 2.4 and 2.5. At low and moderate voltages (V = 0.9 V and 1.5 V), the exciton density is approximately

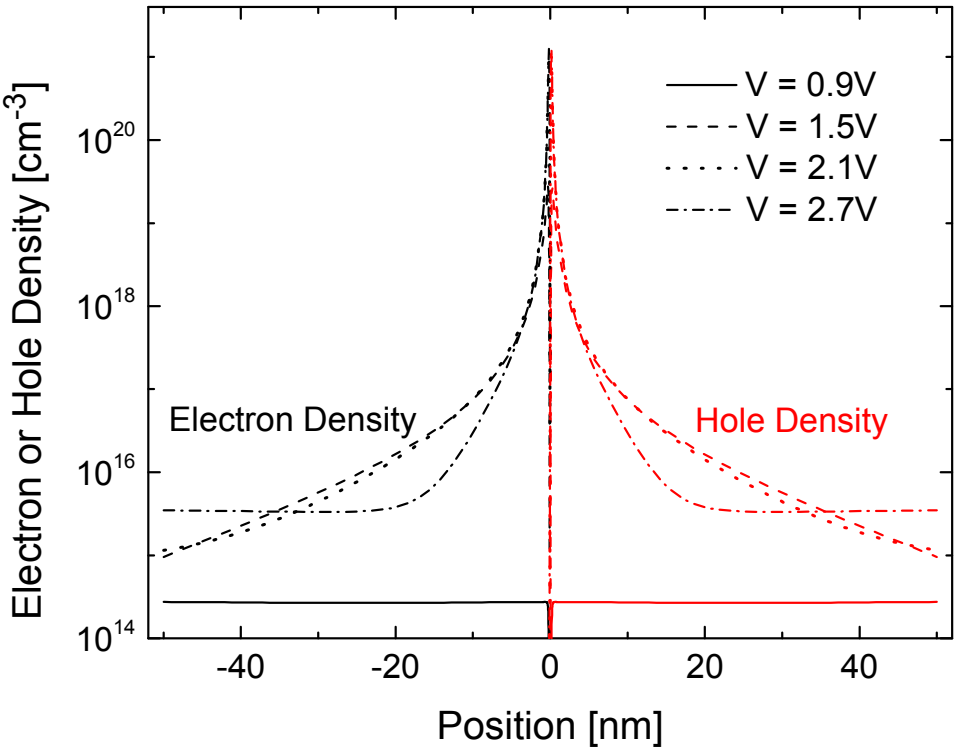

FIG. 2.5. Electron (black color) and hole (red color) density profiles for different applied voltages.

equal to the equilibrium value. For singlet excitons, C_{60} has a lower exciton energy than tetracene, therefore the singlet exciton density is larger in C_{60}. For triplet excitons, C_{60}

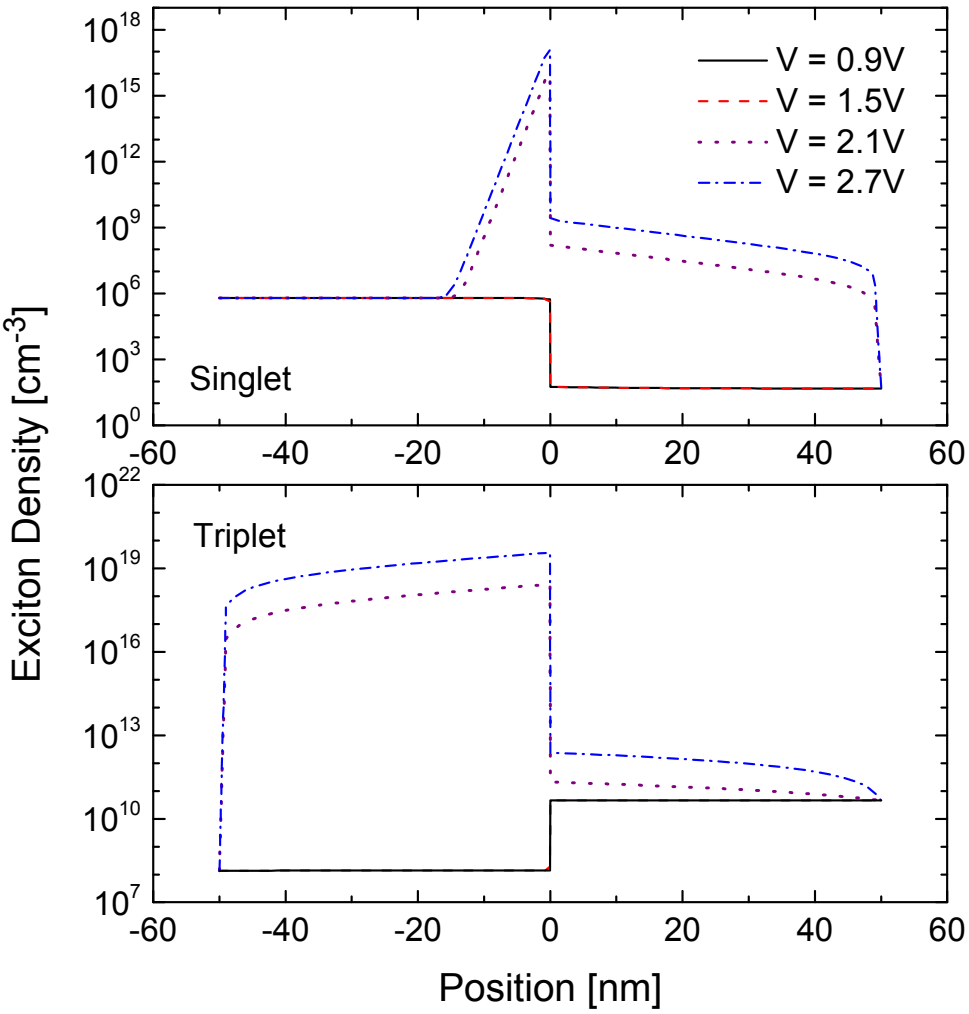

FIG. 2.6. Singlet and triplet exciton density profiles for different applied voltages with no intercfacial exciton- or exciplex-based processes (excitons are generated by bulk recombination).

has a greater exciton energy than tetracene, therefore the triplet exciton density is smaller in C_{60}. At high voltage, electrons and holes may cross the interface and excitons are formed near the interface due to the bulk exciton formation process. Excitons diffuse

within each layer and relax to the ground state. As ΔLUMO > ΔHOMO, the amount of electrons that enters tetracene is much less than the amount of holes that enters C_{60}, therefore both the singlet and triplet excitons have a lower density in tetracene. Triplet excitons have a larger diffusion length than singlet excitons because triplets have a much longer relaxation lifetime.

2.3.3 Light emission from exciton emission in OLEDs

In this section we discuss OLEDs with exciton emission. For simplicity all the interface exciton formation/dissociation coefficients are set to be equal: $\gamma^{-}_{ext,s} = \gamma^{+}_{ext,s} = \gamma^{-}_{ext,t} = \gamma^{+}_{ext,t} = \gamma_{ext}$. The magnitude is varied in terms of γ_L. The exciplex formation/dissociation processes are turned off ($\gamma_{exp} = 0$).

FIG. 2.7 shows the current-voltage characteristics and the electron/hole density profiles for different interfacial exciton formation rates. As the device is in the dark with no excess generation of excitons, exciton formation dominates over exciton dissociation. Interfacial exciton formation provides an extra current path, thus the current increases as the kinetic coefficient γ_{ext} increases. When there is no interface-related exciton formation ($\gamma_{ext} = 0$), the current is limited by the interface barriers. When there is a strong interface exciton formation rate ($\gamma_{ext} = 10^4\gamma_L$ and $\gamma_{ext} = \gamma_L$), the current is limited by the contact barriers. The small discontinuity of the slope of the current vs. voltage curve at $V = V_{bi}$ indicates the image charge effect at the contacts.[82] At $V > V_{bi}$ the image charge effect

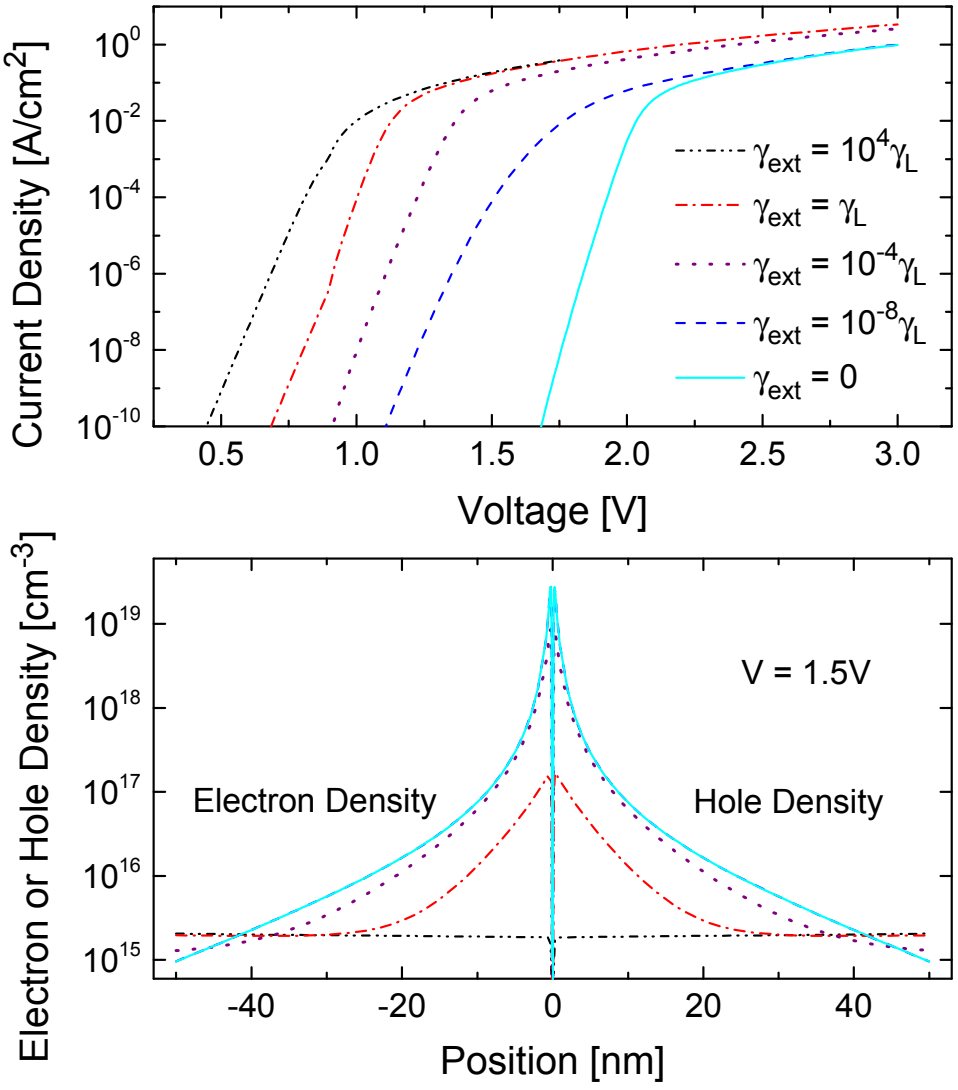

FIG. 2.7. Current-voltage characteristics for an OLED and the corresponding electron and hole density profiles at 1.5 V assuming different interfacial exciton formation rates.

reduces the contact barriers leading to an increase of the current. The electron and hole densities are reduced by interfacial exciton formation. When the kinetic coefficient is sufficiently large ($\gamma_{ext} = 10^4\gamma_L$ for $V = 1.5$ V), carrier accumulation essentially disappears.

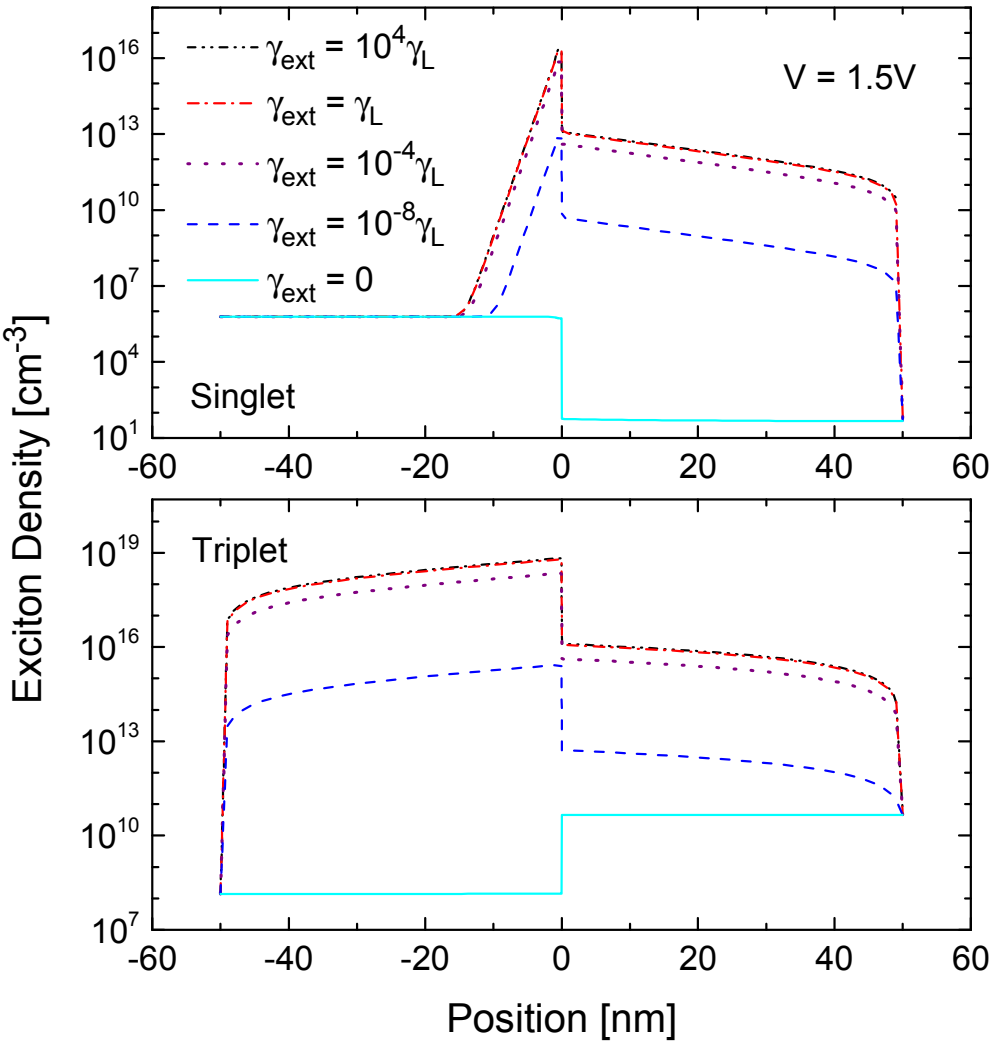

FIG. 2.8. Singlet and triplet exciton density profiles for an OLED for different interfacial exciton formation rates, the applied voltage is 1.5 V.

FIG. 2.8 shows the exciton density profile at V = 1.5 V. The relative differences between singlet/triplet excitons and the ETL/HTL regions have been explained in FIG. 2.6. When there is no interfacial exciton formation, the exciton density is approximately equal to the equilibrium value. When the interfacial exciton formation process takes

place, the exciton densities increase. The exciton densities reach a maximum value when essentially all electrons and holes that arrive at the interface recombine and form excitons. Compared with FIG. 2.6, the exciton densities can increase in two ways: increasing the applied voltage, which increases the bulk exciton formation rate, or increasing the interfacial exciton formation rates.

2.3.4 Light emission from exciplex emission in OLEDs

In this section an OLED with exciplex emission is studied. The interfacial exciplex formation/dissociation processes are turned on and the interfacial exciton formation/dissociation processes are turned off ($\gamma_{ext} = 0$). Under forward bias the interfacial exciplex formation dominates over the exciplex dissociation. As the exciplex formation rate increases, the current increases because exciplex formation provides an additional current path.

FIG. 2.9 shows the current-voltage characteristics for different energy level offsets with no exciplex recombination. Here the device current is entirely due to bulk recombination. The contact barriers are fixed, and the current is limited in all cases by the interface energy discontinuities. When the energy barriers are reduced, more carriers traverse the interface and the current increases. The interface energy barriers also slightly affect the slope of the logarithm of the current vs. voltage at low voltages. Large barriers prevent electrons and holes from crossing the interface and lead to a high density interface dipole layer, which effectively lowers the energy barrier.[100] This effect is more

significant for large barriers where the carrier accumulation is greater. The current therefore increases more rapidly. As the contact barriers are set to be the same for all

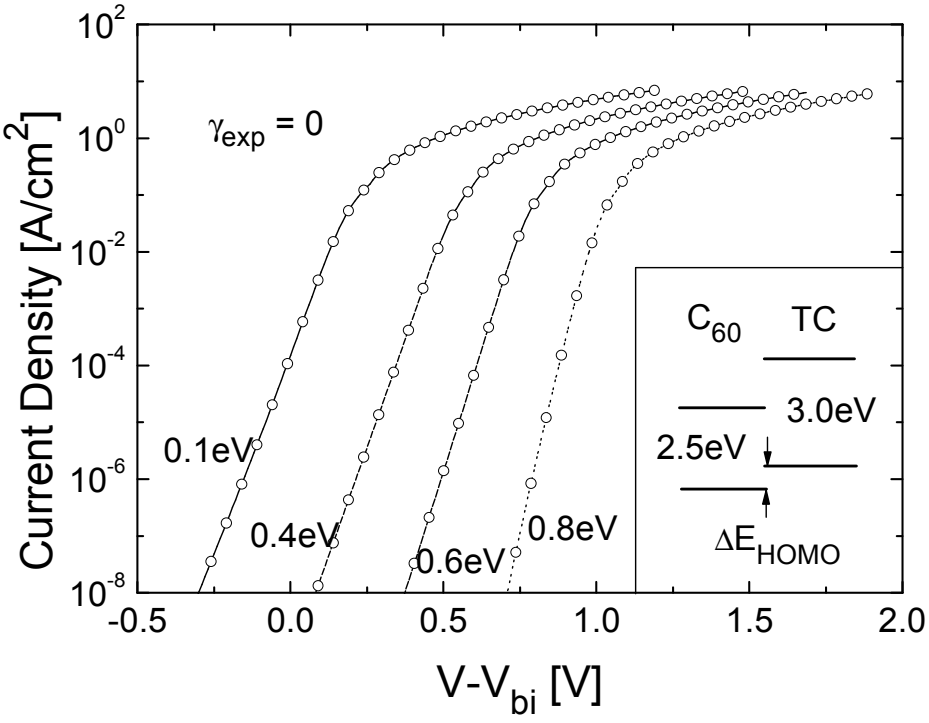

FIG. 2.9. Current-voltage characteristics for different energy level offsets with no exciplex recombination. The lines are total device currents with ΔE_{HOMO} = 0.1 eV, 0.4 eV, 0.6 eV and 0.8 eV, respectively. The circles represent the total recombination currents in the semiconductor. The corresponding built-in potentials are V_{bi} = 1.8 V, 1.5 V, 1.3 V and 1.1 V. The inset shows the schematic band diagram.

cases, the built-in potential, V_{bi}, which is the difference between the energy levels of the electron and hole injection contacts, changes with the energy alignment. To eliminate this effect in the graph, the current is plotted vs. $V - V_{bi}$.

FIG. 2.10 shows how the exciplex recombination rate plays a role in determining the current density. The differences in HOMO and LUMO levels between the two materials are 0.8 eV and 1.3 eV, respectively. For the two curves on the left ($\gamma_{exp} = \gamma_L$, $10^{-4}\gamma_L$), the exciplex recombination rates are relatively high, and the currents are

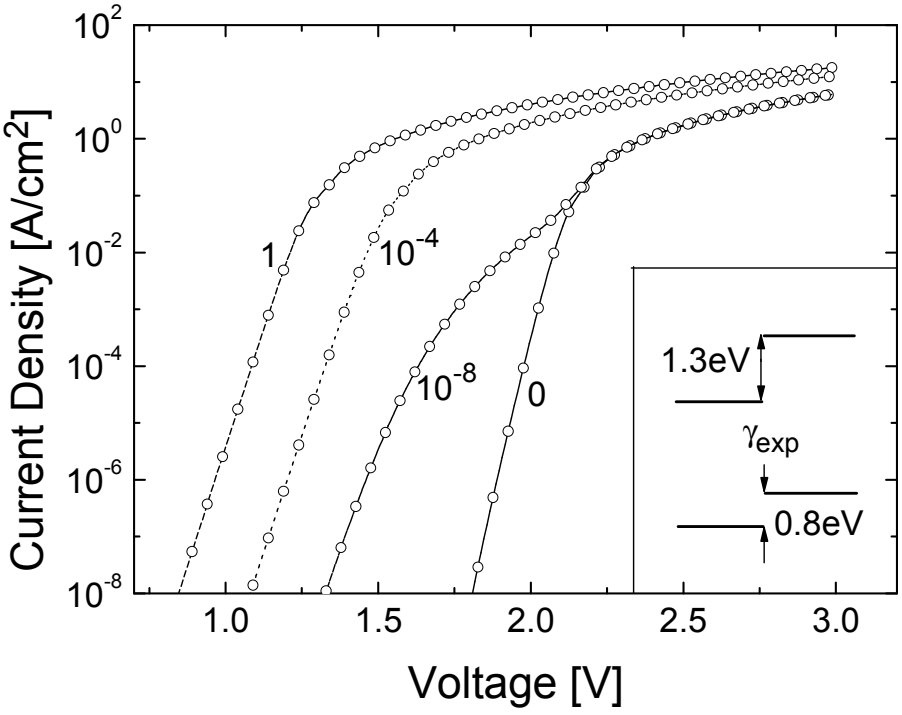

FIG. 2.10. Current-voltage characteristics with different exciplex recombination coefficient, γ_{exp}. The lines are total device currents with $\gamma_{exp} = \gamma_L$, $10^{-4}\gamma_L$, $10^{-8}\gamma_L$, and 0, respectively. The circles represent the total recombination currents in the semiconductor. The inset shows the schematic band diagram.

dominated by exciplex recombination. For the curve on the right, γ_{exp} is zero, thus all the current is due to bulk recombination. For the curve with $\gamma_{exp} = 10^{-8}\gamma_L$, exciplex recombination dominates at low voltages and bulk recombination dominates at high

voltages. At low voltages the current-voltage characteristics are essentially determined by the electrostatics of the two layers in separate states of quasi-equilibrium in all cases. Therefore when γ_{exp} is sufficiently large the current is directly proportional to γ_{exp}.

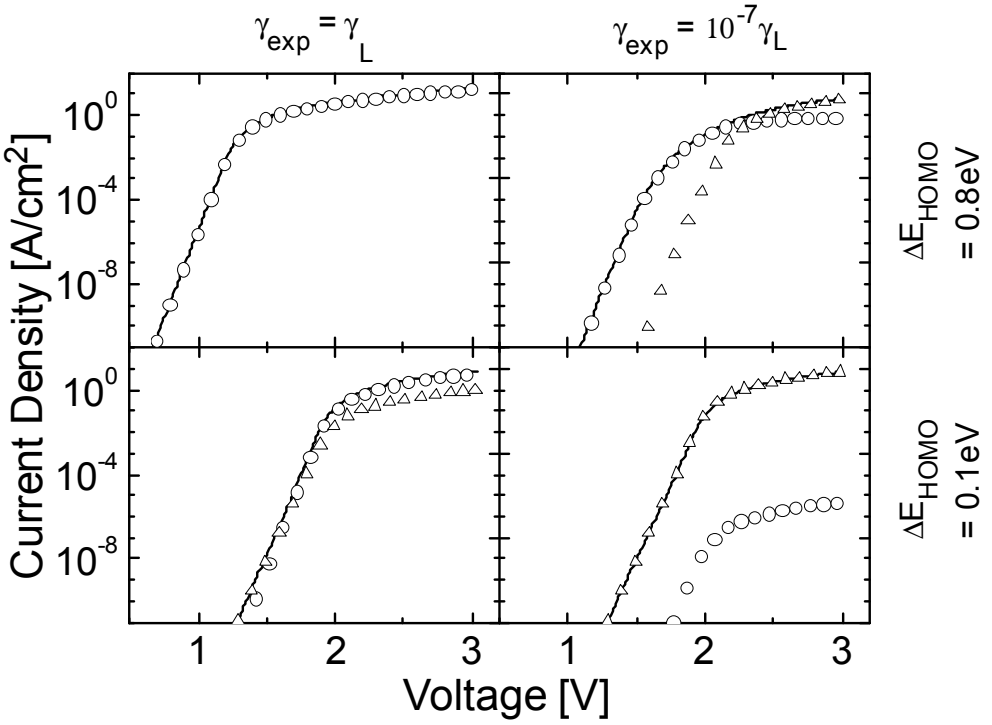

FIG. 2.11. The total current, bulk recombination current and exciplex recombination current with different ΔE_{HOMO} and γ_{exp}. The lines, triangles and circles denote the total current, bulk recombination current, and exciplex recombination current, respectively.

FIG. 2.11 explores the behavior of the two current components with different band offsets and exciplex recombination coefficients. There are four cases: (A) Large ΔE_{HOMO} (ΔE_{LUMO} is always larger than ΔE_{HOMO}) and large γ_{exp} (ΔE_{HOMO} = 0.8 eV, γ_{exp} = γ_L): As the interface barriers are high and the exciplex recombination rate is large, it is

difficult for electrons and holes to traverse the interface, and most of the carriers recombine through exciplex formation. At both high and low voltages, the total current is dominated by the exciplex recombination current. (B) Large ΔE_{HOMO} and small γ_{exp} (ΔE_{HOMO} = 0.8 eV, $\gamma_{exp} = 10^{-7}\gamma_L$): At low voltage, the number of carriers traveling to the interface is small, and they recombine through exciplex formation. At high voltage, large densities of electrons and holes pile up near the interface, but as γ_{exp} is small, injection across the interface and subsequent bulk recombination dominate. (C) Small ΔE_{HOMO} and large γ_{exp} (ΔE_{HOMO} = 0.1 eV, $\gamma_{exp} = \gamma_L$): For small applied voltages, a significant number of holes traverse the interface and recombine in the C_{60} layer. For large voltages, holes can still overcome the interface barrier, but as there is a high electron density in the C_{60} layer at the interface, the holes recombine immediately primarily through the exciplex mechanism. (D) Small ΔE_{HOMO} and small γ_{exp} (ΔE_{HOMO} = 0.1 eV, $\gamma_{exp} = 10^{-7}\gamma_L$): The interface barrier for holes is small and exciplex recombination is weak, therefore at both low and high voltages, the holes overcome the interface barrier and the recombination is mostly through bulk recombination in the C_{60} layer.

FIG. 2.12 shows the current-voltage characteristics with different exciplex relaxation lifetimes. For the short time case ($\tau = 10^{-7}$ s), exciplexes can relax quickly to the ground state and the exciplex density is much smaller than the molecular density at the interface. For the long lifetime case ($\tau = 10^{-6}$ s), exciplexes relax slowly and their current saturates and electrons and holes pile up at the interface. The interface dipole density approaches the interface molecular density at high voltage, therefore the exciplex reduces the barrier and opens the path for carrier injection across the interface and

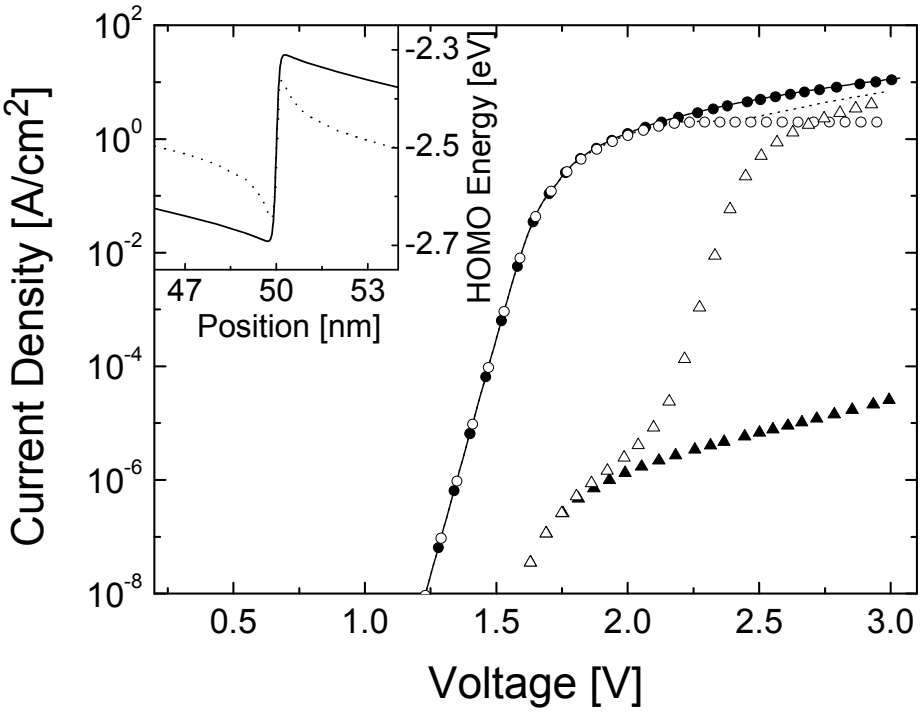

FIG. 2.12. Current-voltage characteristics with different exciplex relaxation times, τ. The lines, triangles and circles denote the total current, bulk recombination current, and exciplex recombination current, respectively. The solid line and filled symbols correspond to $\tau = 10^{-7}$ s; the dotted line and open symbols correspond to $\tau = 10^{-6}$ s. $\Delta E_{HOMO} = 0.4$ eV. The inset shows the HOMO energy levels at $V = 2.5$ V for the two cases.

subsequent bulk recombination. As the voltage increases the bulk recombination current increases and eventually dominates.

In FIG. 2.13, the singlet and triplet exciplex densities are plotted vs. voltage for different exciplex formation rates. The exciplex relaxation lifetimes in all cases are 10^{-9}

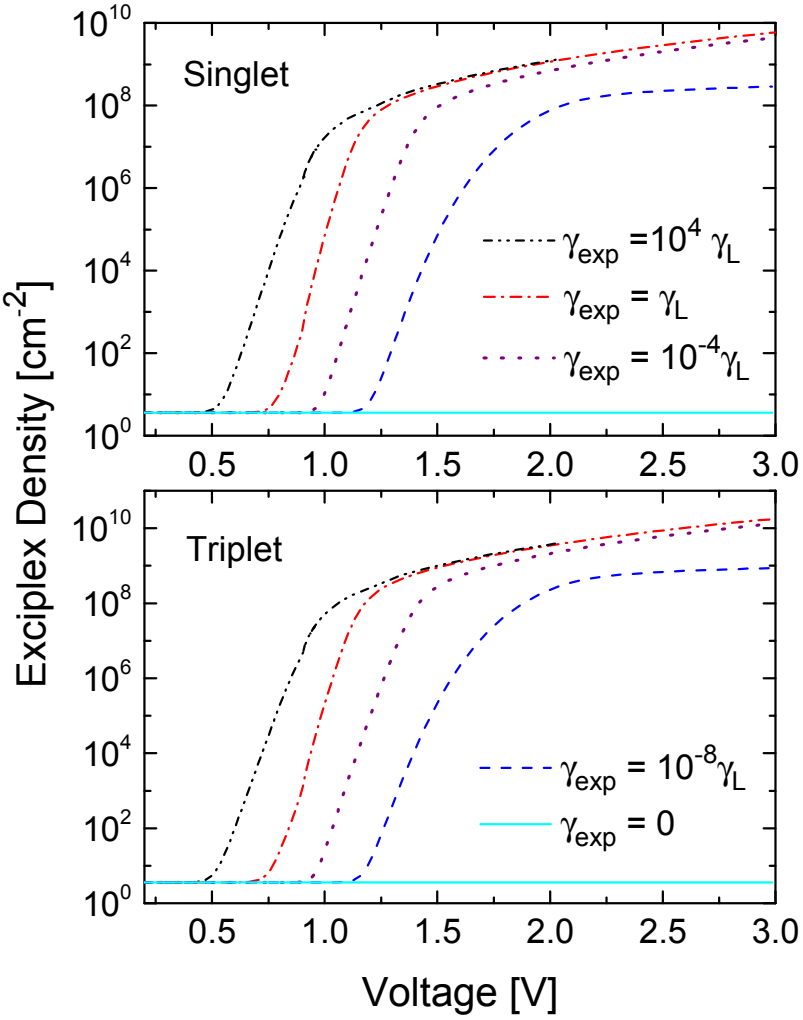

FIG. 2.13. Singlet and triplet exciplex densities vs. voltage in an OLED for different exciplex formation rates.

s therefore the exciplex density is always much smaller than the interface molecular density. At low voltages the exciplex densities are equal to their equilibrium values. Since we have assumed that the exciplex energy parameters are the same for singlets and triplets, their equilibrium values are equal. At high voltages exciplexes are formed in the

interface region and the density increases. Because we have assumed that the singlet and the triplet exciplexes have the same lifetimes, their density profiles have a ratio of 1 to 3. For the curve with $\gamma_{exp} = 10^{-8}\gamma_L$, the exciplex formation rate is low, therefore at high voltages some electrons and holes cross the barrier and contribute to bulk exciton formation rather than interface exciplex formation.[48]

2.3.5 Nongeminate recombination in OPCs

In this section we consider a photovoltaic device with nongeminate recombination. The device is under illumination and forward bias. The interfacial exciton formation/dissociation processes are turned on and the exciplex formation/ dissociation processes are turned off ($\gamma_{exp} = 0$). In this case the interfacial exciton dissociation dominates over exciton formation.

In FIG. 2.14, we consider the impact of different photogeneration profiles on the current-voltage characteristics and exciton density distributions. Four different cases are considered. (A) The device with no photogeneration (in the dark) as a comparison. (B) The device with uniform photogeneration throughout. As C_{60} and tetracene have different singlet exciton energies, they have a different absorption spectra. Therefore two additional cases are considered. (C) A uniform photogeneration profile in C_{60} but no

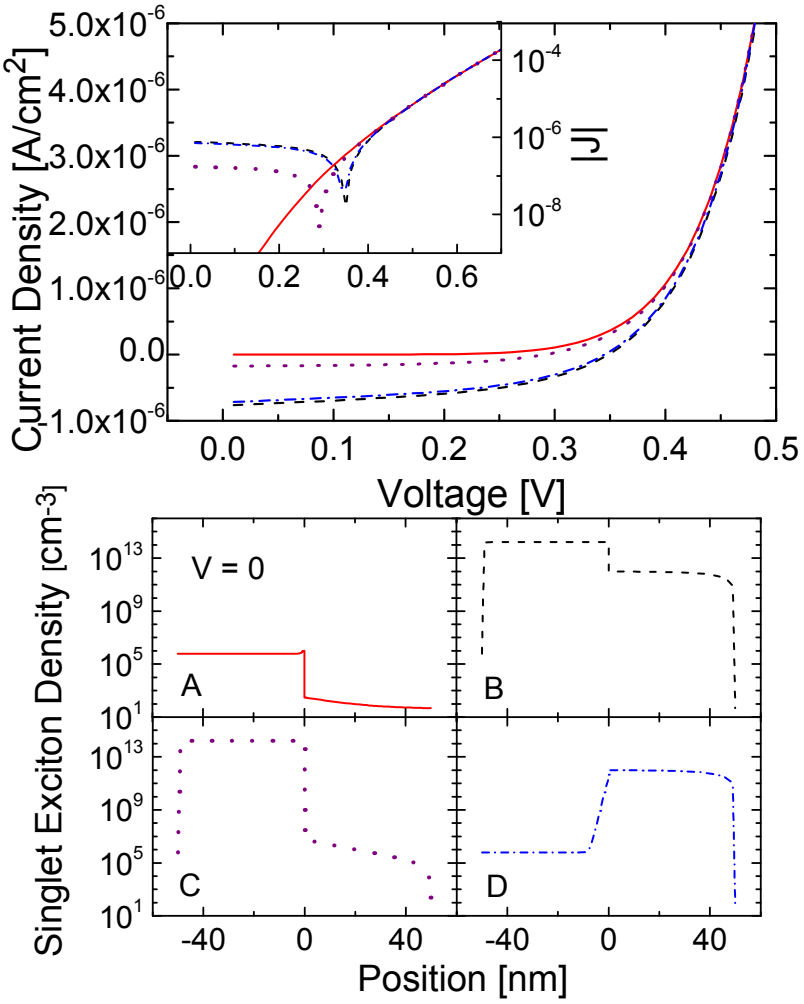

FIG. 2.14. Current-voltage characteristics for different photogeneration profiles for an OPC with a high interface dissociation rate. The inset shows the absolute values of the current on semi-logarithmic scale. The bottom plot shows the singlet exciton profiles at $V = 0$ for four different cases.

excitons generated in tetracene. (D) A uniform photogeneration profile in tetracene but no excitons generated in C_{60}. The photogeneration rates in all cases are $G_l = 10^{22}$ $cm^{-3}s^{-1}$. Under illumination interfacial exciton dissociation dominates over interfacial

recombination. To ensure significant exciton dissociation, the interfacial exciton dissociation coefficient is set to be sufficiently large ($\gamma_{ext} = 10^{10}\gamma_L$). The singlet exciton density profiles at $V = 0$ for all cases are plotted. In case (A), the exciton density is equal to the equilibrium value. In case (B), excitons are generated throughout the device. Because tetracene has a shorter exciton lifetime, its resulting exciton density is lower than that of C_{60}. In cases (C) and (D), the exciton density is high in the corresponding layers with photogeneration. The excitons in the interface region can dissociate into electrons and holes, and excitons can reform in both the ETL and HTL layers. This explains the increase in exciton density in the materials without photogeneration in cases (C) and (D). The current-voltage characteristics are plotted on linear and logarithmic scale (absolute value of current). It is obvious that case (B) has the maximum photocurrent because of maximum photogeneration. It is interesting to observe that the photocurrent in case (D) is much larger than in case (C). This is due to the large exciton diffusivity in tetracene. The photogeneration rate is the same for the two cases, but in tetracene a larger part of the excitons can travel to the interface and dissociate, which leads to a larger photocurrent.

2.3.6 Geminate recombination in OPCs

In this section geminate recombination is considered for a photovoltaic cell. The calculations are for non-zero photoexcitation. The direct transition between excitons and electrons/holes is turned off ($\gamma_{ext} = 0$), and exciton dissociation is assisted by forming an intermediate exciplex state. In this case the dominant processes are exciton transfer to exciplexes and exciplex dissociation into electrons and holes. In the following

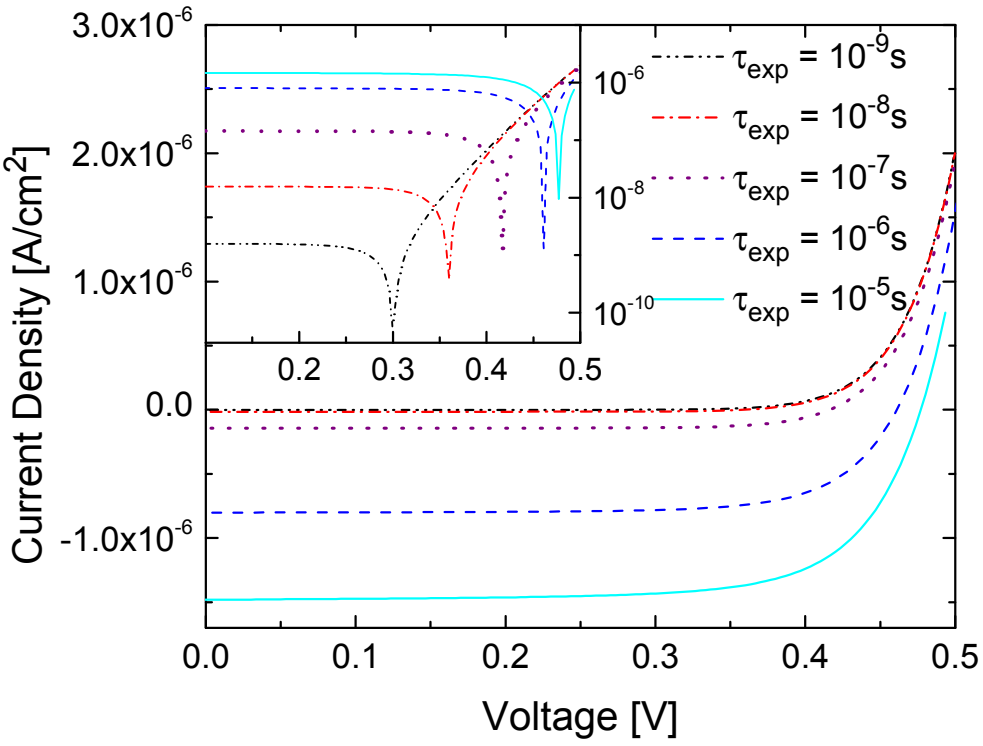

FIG. 2.15. Current-voltage characteristics for an OPC with geminate recombination and different exciplex relaxation lifetimes. The inset shows the absolute values of the currents on semi-logarithmic scale.

calculations, we assume that the rate of excitons transferring to exciplexes is large enough so that this is not the overall limiting process.

FIG. 2.15 shows the current-voltage characteristics for different exciplex relaxation lifetimes. The inset of the figure displays the absolute value of the currents on logarithmic scale. The lifetimes for singlet and triplet exciplexes are assumed to be the same. It is shown that, as the exciplex relaxation lifetimes increase, the photocurrent increases as well. The process of exciplexes relaxing to the ground state indicates

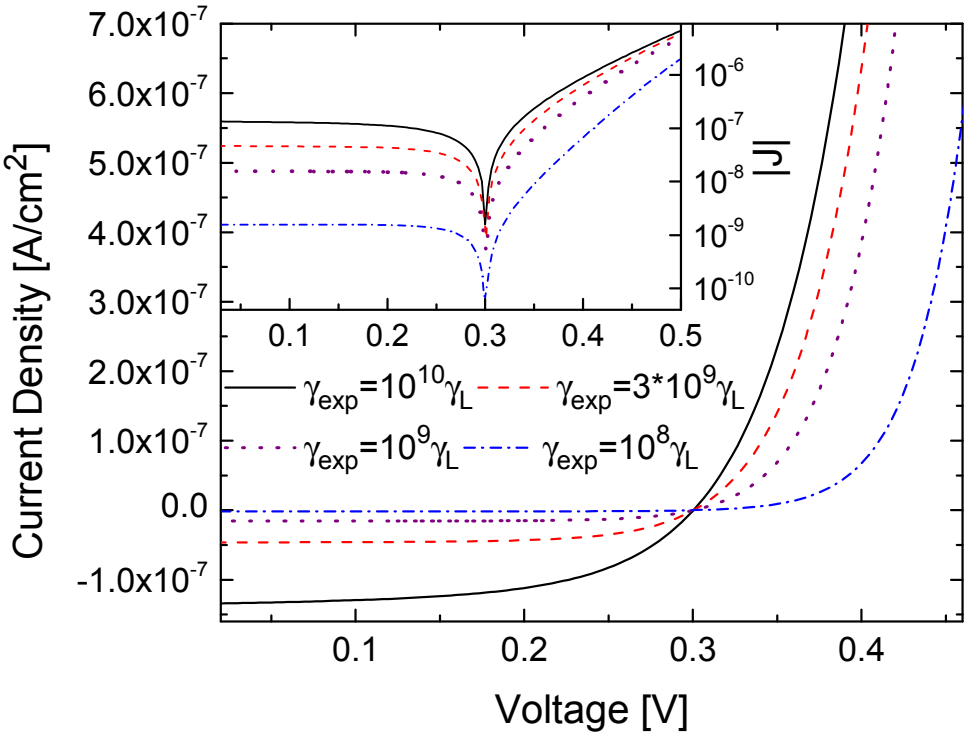

FIG. 2.16. Current-voltage characteristics for an OPC with geminate recombination and different exciplex dissociation rates. The inset shows the absolute values of the currents on semi-logarithmic scale.

geminate recombination. This process competes with the generation of electrons and holes by exciplex dissociation. As the lifetimes increase, it is more difficult for exciplexes to relax to the ground state. Therefore more exciplexes dissociate, and the

current increases. In the logarithmic plot, it is observed that the photocurrent is proportional to the exciplex lifetimes except for the case of very long lifetime ($\tau = 10^{-5}$ s). In this case the exciplex density approaches the interface molecular density, and some exciplexes undergo the reverse process and transfer back to excitons.

FIG. 2.16 shows the current-voltage characteristics for different exciplex dissociation rates. The absolute values of the currents are also plotted on logarithmic scale. As the exciplex dissociation coefficient decreases, more exciplexes relax to the ground state. The photocurrent decreases and the geminate process becomes dominant. The result shows that the efficiency of the device is degraded by geminate recombination, which agrees with the experimental results.[80,81] Another interesting observation is that the open circuit voltage V_{OC} is unchanged. The open circuit voltage is reached when the current injected from the contacts exactly cancels the current due to exciplex dissociation. According to our previous discussion,[48] with the device parameters given in this figure, the injected current results in exciplex formation in the interface region rather than exciton formation in the bulk region. When the exciplex dissociation coefficient is varied, the exciplex formation coefficient also changes because of detailed balance. Therefore, at $V = V_{OC}$, both the injection current and the dissociation current are changed by the same amount, and the open circuit voltage remains unchanged.

2.4 Conclusion

The microscopic processes at an organic heterojunction interfaces and their consequences for macroscopic device characteristics have been discussed, and a systematic device model is presented. The model addresses the important processes at the interface, such as interface exciton formation/dissociation, exciplex formation/ dissociation, and geminate/nongeminate recombination. The interface region is treated as continuous over a very short distance thus avoiding the introduction of internal boundary conditions. A simple bilayer structure is used as an example to obtain illustrative results. Various possible device applications are examined, with different situations emphasizing different processes. It is shown how processes that occur at the interface effectively control the overall device characteristics.

In our model exciton transitions between the singlet and triplet exciton states are not included. To incorporate this into the model additional terms which include the singlet/triplet exciton density and the intersystem crossing time should be added to the rate equations. For example in C_{60}, as singlet excitons may quickly convert through intersystem crossing to triplet excitons,[87] the singlet exciton diffusion length is not easily obtained from experiment. In tetracene the triplet exciton energy is close to half of the singlet exciton energy, therefore a singlet exciton may split into two triplet excitons, and two triplet excitons may combine into one singlet exciton as well.[99]

Chapter 3 Improving organic photovoltaic device efficiency through interface engineering

3.1 Introduction

Organic-semiconductor-based photovoltaic devices are promising for future energy conversion applications due to their low cost, ease of fabrication, and flexibility.[101,102] However, a major limitation of these devices is their relatively low efficiency.[103] Photons absorbed generate excitons, which upon dissociation and charge carrier collection by the contacts can yield an electrical current. As excitons in organic materials have large binding energies, interfaces between different types of materials with appropriate energy level alignments are needed for exciton dissociation. In order to improve the device efficiency various approaches have been explored, such as bulk heterojunction structures,[11] blocking of exciton quenching,[104] enhancement of charge collection,[105] etc. In this chapter, organic photovoltaic devices with a bilayer structure are studied in detail based on results in chapter 2, because this is the simplest configuration. Generalizations to more complicated device structures can build on a thorough understanding of bilayer devices.

The efficiency of a photovoltaic device is characterized by its power efficiency, η_{PE}, which is defined as the maximum electrical output power for a given optical input power. The maximum output power of a photovoltaic device can be expressed as the

product of three quantities: the short-circuit current J_{SC}, the open-circuit voltage V_{OC}, and the fill factor *FF*, which are all related to the following microscopic processes. Excitons are generated by light absorption and diffuse toward the interface between the electron transport layer (ETL, or acceptor active layer) and the hole transport layer (HTL, or donor active layer). The energy level alignment between the two materials is such that it is energetically favorable for excitons to dissociate into electrons and holes located in the corresponding layers. The generated electrons and holes are collected by the corresponding contacts and photocurrent is produced. Because of geminate processes discussed in section 2.3.6, charge-transfer states (or exciplexes) are usually formed shortly after the exciton dissociation. These excitations subsequently either relax

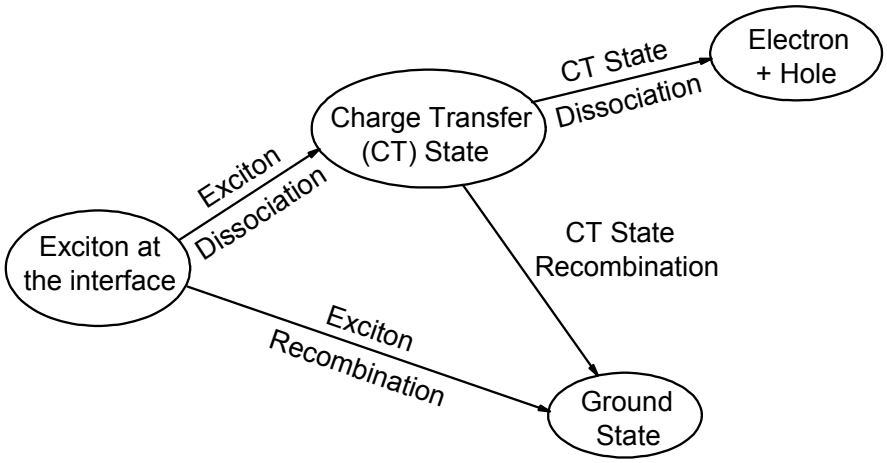

FIG. 3.1. Schematic diagram of critical microscopic processes at the ETL/HTL interface of an OPC.

to the ground state or dissociate into free electrons and holes. The processes are summarized in FIG. 3.1.

Only mobile electrons and holes can contribute to the photocurrent. In order to yield good device efficiency, (i) exciton dissociation (ED) should dominate over exciton recombination (ER), and (ii) charge-transfer state dissociation (CTD) should dominate over charge-transfer state recombination (CTR). For typical devices where the energy level offset at the interface of the ETL/HTL is designed to facilitate exciton dissociation, (i) is readily achieved. However, for the charge transfer states there is generally no guarantee that the CTD will dominate over the CTR, and hence (ii) may limit the overall efficiency.

Recently, Campbell and Crone proposed an improvement of the CTD to CTR ratio by inserting a thin insulating layer between the ETL and the HTL. Their experimental results showed an improved short-circuit photocurrent.[106] In this chapter, a detailed analysis of this approach to improve the performance of organic photovoltaic devices is presented. In addition to the short-circuit photocurrent, the effect of the insulating material on the open-circuit voltage is determined by numerical simulation and a corresponding analytical approximation is presented. The results of the device fill factor and power efficiency are also studied by numerical calculation and discussed.

3.2 Control of microscopic processes

An advantage of the insulating layer incorporation is that it maintains most of the original device structure. The ratio between different processes can be tuned without the need of changing the ETL/HTL layer materials. For the charge-transfer state, the bound electron and hole reside on the ETL and HTL molecules, respectively, separated by the insulating layer. The CTR rate depends on the wavefunction overlap between the bound electron and hole; as their separation increases with the insulating layer thickness, the CTR rate decreases. The rate of CTD is enhanced because the binding energy of the charge transfer state decreases as its positive and negative parts are separated by a greater distance, making the charge transfer state less stable. Therefore, the ratio of CTD to CTR rates, and thus the efficiency, increases. The insulating layer inhibits the ED process, which can be viewed as a tunneling process across the interface. However, as the ED rate is usually orders of magnitude greater than the ER rate, this reduction does not affect the overall efficiency significantly for a reasonable range of insulator thicknesses. The incorporation of the insulating layer does not significantly affect the exciton diffusion to the interface either. Within the range of the insulator thickness considered here, as the exciton dissociation rate at the interface is orders of magnitude greater than the exciton diffusion rate, the exciton density near the interface is always negligible compared to that in the bulk ETL and HTL, and the density gradient remains unchanged for different insulator thicknesses.

In order to describe these processes quantitatively, a simple physics-based model is introduced. The ED yielding the charge-transfer state is approximated as a tunneling process, where the electron or hole comprising an exciton that arrives at the interface tunnels across the interface barrier and its counterpart remains in place. This process rate has an exponential dependence on the thickness of the insulating layer. It can be written as $\exp(-L/L_{ED})$, where L is the thickness of the insulating layer, and L_{ED} is the characteristic decay length for ED. The rate of CTR is proportional to the overlap of the electron and hole wavefunctions. It is also approximated by an exponential, $\exp(-L/L_{CTR})$, where L_{CTR} is the corresponding decay length for CTR. The decay lengths depend on the energy level offsets between the ETL/HTL and the insulating layer. The CTD rate is inversely proportional to the charge-transfer state equilibrium density, N_{CT0}. N_{CT0} is proportional to $\exp(E_B/2kT)$. E_B is the binding energy of the charge-transfer state. For the simplest case, $1/E_B$ depends linearly on the distance between the positive and negative parts of the exciton, i.e. $1/E_B - 1/E_{B0}$ is proportional to L. (E_{B0} is the binding energy for vanishing tunnel barrier.) These thickness-dependent processes are incorporated into a numerical device model for bilayer structures that has been presented in chapter 2. C_{60} and tetracene are chosen as the ETL and HTL materials, respectively.[86]

3.3 Short-circuit photocurrent

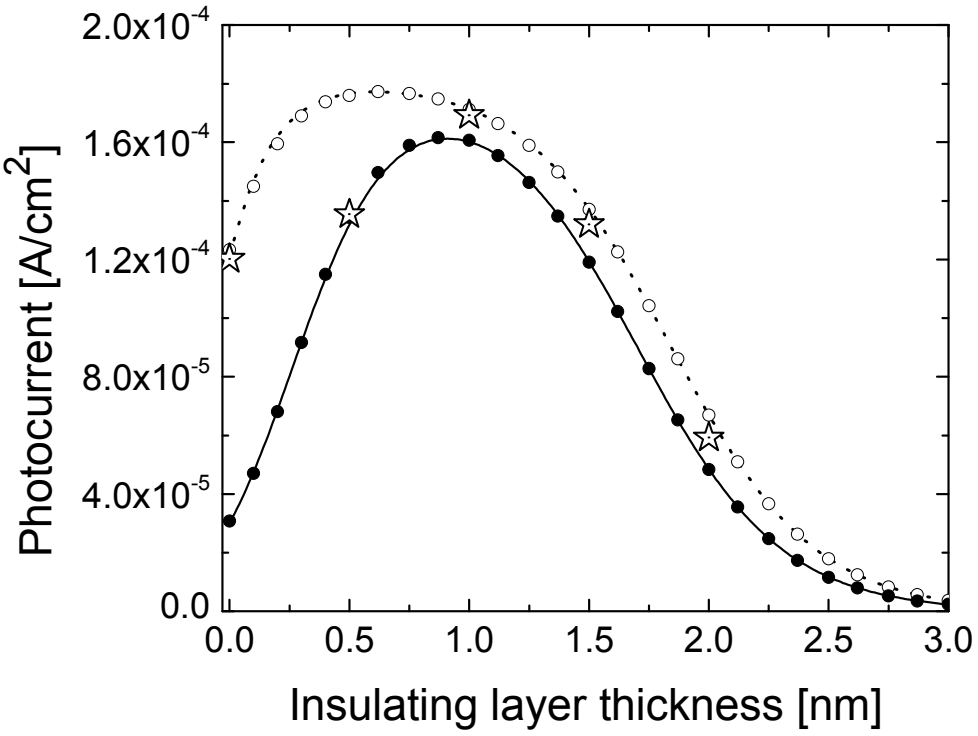

FIG. 3.2. Short-circuit photocurrents as a function of the insulating layer thickness. The stars are experimental data from reference 106. The circles are simulation results from the numerical device model in section 2.3.6. The lines are analytical approximations from equation (3.1). The open circles (dotted line) and filled circles (solid line) represent the different sets of device parameters shown in TABLE 3.1. Experimental data are courtesy of Dr. Brian K. Crone and Dr. Ian H. Campbell at Los Alamos National Laboratory.

Calculated short-circuit current results under illumination are compared with recent experimental data[106] for different thicknesses of the insulating layer, as shown in

FIG. 3.2. The stars are from the experiments and the circles are from the model simulations. The device is assumed to be illuminated monochromatically and photons are absorbed by creating excitons in tetracene only. To obtain simple results in the subsequent analysis, the absorption profile in tetracene is assumed to be constant, with a uniform exciton generation rate $G_L = 10^{21}$ cm^{-3}s^{-1}. The thickness of the tetracene layer, L_{TC}, is 30 nm. The insulating material used in the experiments is LiF.[106] The charge-

TABLE 3.1. Device parameters for calculation in chapter 3.[69,98,107-112]

Parameters	Open circles & dotted line	Filled circles & solid line
R_{ER}	$(0.2\ \text{ns})^{-1}$	$(0.2\ \text{ns})^{-1}$
R_{ED0}	$(12.5\ \text{fs})^{-1}$	$(20\ \text{fs})^{-1}$
R_{CTR0}	$(20\ \text{ns})^{-1}$	$(8\ \text{ns})^{-1}$
R_{CTD0}	$(10\ \text{ns})^{-1}$	$(40\ \text{ns})^{-1}$
E_{B0}	0.1 eV	0.05 eV
L_{ED}	0.3 nm	0.3 nm
L_{CTR}	0.25 nm	0.25 nm
D_E	1.1×10^{-2} cm^2/s	1.1×10^{-2} cm^2/s

collecting contacts are assumed to be ohmic with a 0.15 eV barrier and ideal quenching of excitons.

The device parameters can be extracted within certain ranges as shown in TABLE 3.1. R_{ER} (= τ_E^{-1}) is the ER rate. τ_E is the relaxation lifetime for singlet excitons in tetracene. R_{ED0} is the ED rate at zero thickness of the insulating layer. R_{CTR0} is the corresponding CTR rate. R_{CTD0} is the CTD rate for vanishing tunnel barrier. E_{B0} is the binding energy of the charge transfer state. L_{ED} and L_{CTR} are the decay lengths for ED and CTR, respectively. D_E is the diffusivity of singlet excitons in tetracene. All the values of the parameters above are reasonable and comparable to the results in the literature. [69,98,107-112]

Both the experiments and simulations show that, as the insulating layer thickness increases, the device photocurrent initially increases and subsequently decreases. In order to understand the device physics, in the following we derive an analytical approximation for the short-circuit current from the exciton kinetics of FIG. 3.1. This analytical approximation is shown in FIG. 3.2 as the dotted and solid lines corresponding to different sets of device parameters. The simple expressions agree well with the numerical simulation results. The short-circuit photocurrent can be represented approximately by the following equation:

$$J_{SC} \approx J_{MAX}\eta_{ET}\eta_{ED}\eta_{CTD}\eta_{CC} \tag{3.1}$$

J_{MAX} is the maximum photocurrent the device can generate assuming all the photo-excited excitons dissociate into free electrons/holes, which are all collected by the contacts. η_{ET} is the exciton transport efficiency, which represents the fraction of photo-excited excitons that arrives at the ETL/HTL interface. η_{ED} is the exciton dissociation efficiency, which is the ratio of ED over ED + ER. η_{CTD} is the charge-transfer state

dissociation efficiency, which is the ratio of CTD over CTD + CTR. η_{CC} is the charge collecting efficiency, which is the fraction of electrons and holes that arrive at the contacts. In our case $\eta_{CC} \approx 100\%$ as very few recombination events take place in the bulk ETL or HTL layers. From the discussions above, J_{MAX} and η_{ET} depend only on the bulk properties of the device and are independent of the insulating layer. The insulating layer, however, has a strong impact on η_{ED} and η_{CTD}.

J_{MAX} is calculated from the total exciton generation rate $L_{TC}G_L$. Each exciton generates one electron and one hole. Hence, multiplying by the unit charge, e, J_{MAX} is given by $J_{MAX} = eL_{TC}G_L = 4.8 \times 10^{-4}$ A/cm^2.

η_{ET} is calculated from the exciton flux, $-D_E dN_E/dx$, at the interface divided by the total exciton generation rate, $L_{TC}G_L$. N_E is the (singlet) exciton density and dN_E/dx is its gradient. Because of the ideal quenching boundary condition, the excitons near the contact will flow to it and relax to the ground state. The excitons quenched at the contact do not contribute to the photocurrent and the maximum of η_{ET} is 50%, which means half of the excitons flow to the ETL/HTL interface (at $x = 0$) and the other half flow to the contact (at $x = L_{TC}$). If the exciton diffusion length $L_{DIFF} = \sqrt{D_E \tau_E}$ is not large enough, η_{ET} will be even smaller because some excitons do not arrive at either boundary. From the rate equation of excitons at steady state and assuming that the exciton density at $x = 0$ and $x = L_{TC}$ are both zero, we can derive an expression for the spatial distribution of excitons:

$$N_E(x) = G_L \tau_E \left[1 + \frac{\sinh\left(\frac{x - L_{TC}}{L_{DIFF}}\right) - \sinh\left(\frac{x}{L_{DIFF}}\right)}{\sinh\left(\frac{L_{TC}}{L_{DIFF}}\right)} \right] \tag{3.2}$$

From equation (3.2), the magnitude of the exciton flux at the interface is $D_E \frac{dN_E}{dx}(x=0)$ $= G_L L_{DIFF} \frac{\cosh(L_{TC}/L_{DIFF}) - 1}{\sinh(L_{TC}/L_{DIFF})}$. Substituting $L_{DIFF} = \sqrt{D_E \tau_E} = 14.8$ nm[98,108,111,112] and $L_{TC} = 30$ nm in the expression, one obtains $\eta_{ET} = \frac{L_{DIFF}}{L_{TC}} \frac{\cosh(L_{TC}/L_{DIFF}) - 1}{\sinh(L_{TC}/L_{DIFF})} = 37.8\%$.

In order to calculate η_{ED} and η_{CTD} it is important to draw a clear distinction between two related concepts: the local rate of a process and the overall impact of that process on the device characteristics. The local rate of a process has the dimension of inverse time. The total effect of a process is described by its local rate multiplied by the length scale over which it is effective. The characteristic parameter therefore has units of velocity. As the ED, CTD and CTR processes only occur at the interface between the ETL and the HTL, their length scale L_{ITF} is limited to a small distance near the interface (about the size of a molecule). In the calculations L_{ITF} is taken to be 0.44 nm.[113] The estimation of the length scale for the ER needs some care. Different from the calculations of η_{ET} where excitons are uniformly generated throughout the tetracene layer, in the calculations of η_{ED} the excitons have already arrived at the ETL/HTL interface. An exciton located at the ETL/HTL interface can diffuse away from it toward the contact or relax to the ground state. In the example device, only the diffusion in tetracene is of interest because the excitons are only generated on the tetracene side of the interface.

Again, the ratio of the exciton diffusion length L_{DIFF} to the thickness of the tetracene layer L_{TC} plays a role. When L_{DIFF} is much smaller than L_{TC}, the length scale of ER is approximately L_{DIFF}. When L_{DIFF} is comparable to or greater than L_{TC}, essentially all excitons starting from the interface can arrive at the contact. By solving the diffusion equation with an ideal quenching boundary condition at the contact, an effective diffusion length L_{DIFF}' is obtained: $L_{DIFF}' = L_{DIFF}\coth(L_{TC}/L_{DIFF})$. This expression agrees with the preceding case of $L_{DIFF}' \approx L_{DIFF}$ when $L_{DIFF} << L_{TC}$. In general, as $\coth(x) > 1$, the effective diffusion length is greater than the diffusion length. This is because the quenching contact "draws in" excitons from the interface, thus enhancing the effect of diffusion. The overall ER velocity, v_{ER}, is the local rate multiplied by the length scale $R_{ER}L_{DIFF}'$. For the case $L_{DIFF} >> L_{TC}$, where most of the excitons can arrive and relax at the contact, $v_{ER} = R_{ER}L_{DIFF}' \approx R_{ER}\frac{L_{DIFF}^2}{L_{TC}} = \frac{D_E}{L_{TC}}$. In this case v_{ER} is independent with the local ER rate in tetracene because the ER mostly occurs at the contact.

The exciton dissociation efficiency η_{ED} as a function of the insulating layer thickness L is expressed as:

$$\eta_{ED} = \frac{v_{ED}}{v_{ED} + v_{ER}} = \frac{v_{ED0}\exp(-L/L_{ED})}{v_{ED0}\exp(-L/L_{ED}) + v_{ER}} = \frac{\exp(-L/L_{ED})}{\exp(-L/L_{ED}) + v_{ER}/v_{ED0}} \qquad (3.3)$$

where $v_{ED} = R_{ED}L_{ITF}$ and $v_{ER} = R_{ER}L_{DIFF}'$ are the overall exciton dissociation and exciton recombination velocities. η_{ED} is determined by the decay length L_{ED} and the ratio for zero thickness of the insulating layer, v_{ED0}/v_{ER}. L_{ED} determines the 'slope' of η_{ED} and v_{ED0}/v_{ER} determines its starting point. Usually $v_{ED0}/v_{ER} >> 1$, hence the value of η_{ED} at $L = 0$ is approximately equal to 1. As L increases, η_{ED} gradually decreases.

The charge-transfer state dissociation efficiency η_{CTD} as a function of L is expressed as:

$$\eta_{CTD} = \frac{v_{CTD}}{v_{CTD} + v_{CTR}} = \frac{v_{CTD}}{v_{CTD} + v_{CTR0}\exp(-L/L_{CTR})} = \frac{\exp(L/L_{CTR})}{\exp(L/L_{CTR}) + v_{CTR0}/v_{CTD}} \quad (3.4)$$

where $v_{CTD} = R_{CTD}L_{ITF}$ and $v_{CTR} = R_{CTR}L_{ITF}$, are the overall velocities characterizing charge transfer state dissociation and recombination, and $R_{CTD} = R_{CTD0}\frac{N_{CT0}(L=0)}{N_{CT0}(L)} = R_{CTD0}\frac{\exp(E_{B0}/2kT)}{\exp(E_B/2kT)}$ depends on the equilibrium density of charge transfer state excitations, N_{CT0}. As the CTD and CTR have the same length scales, v_{CTR0}/v_{CTD} is equivalent to the ratio of the local rates, R_{CTR0}/R_{CTD}. E_{B0} is the binding energy at $L = 0$. $E_B = E_{B0}\frac{L_0}{L + L_0}$ is the binding energy for an insulating layer with thickness L. $L_0 \approx 1$ nm is taken as the average distance between the centers of neighboring tetracene and C_{60} molecules.[113,114] η_{CTD} is determined by the decay length L_{CTR} and the ratio v_{CTR0}/v_{CTD}. Similar to the case of η_{ED} above, L_{CTR} determines the 'slope' of η_{CTD} and v_{CTR0}/v_{CTD} determines its initial value. As L increases, η_{CTD} increases and gradually approaches 1.

Based on the discussion above, the results for the short-circuit current in FIG. 3.2 can be understood. As L starts to increase from zero, η_{CTD} increases rapidly while η_{ED} stays almost constant and does not decrease much. From equation (3.1), the short-circuit photocurrent increases with L. When L is large enough η_{CTD} approaches unity and cannot increase further. η_{ED} begins to decrease and the photocurrent decreases. Another advantage of the idea of incorporation the insulating layer is that the parameters determining η_{ED} and η_{CTD} can be designed separately. The ratios v_{ED0}/v_{ER} and v_{CTR0}/v_{CTD}

are properties of the bilayer device structure, which are independent with the specific type of the insulating material. On the other hand, the decay lengths L_{ED} and L_{CTR} are purely determined by the properties of the insulating material.

3.4 Open-circuit voltage

When the device is under forward bias, additional microscopic processes are introduced. Electrons and holes are injected from the contacts and flow toward the ETL/HTL interface. At the interface they recombine and charge-transfer states are formed. The charge-transfer states can subsequently relax to the ground state. When the forward bias is large enough, the charge injection from the contacts and the charge collection by the contacts will balance. The total device current will be zero and the bias in this case is defined as the open-circuit voltage V_{OC}. The calculated open-circuit voltages as a function of the insulating layer thickness are plotted in FIG. 3.3. The open and filled circles are from numerical simulation with corresponding sets of device parameters in FIG. 3.2. The dotted and solid lines are analytical approximations to be discussed below. The analytical approximation agrees well with the numerical results, which shows that the incorporation of the insulating layer not only improves the short-circuit current, but also the open-circuit voltage.

As discussed in a section 2.2.1, the electron-hole recombination at the interface is proportional to the product of the electron density, n, and the hole density, p. The CTD dissociation is proportional to the charge-transfer state density, N_{CT}. At $V = V_{OC}$, these

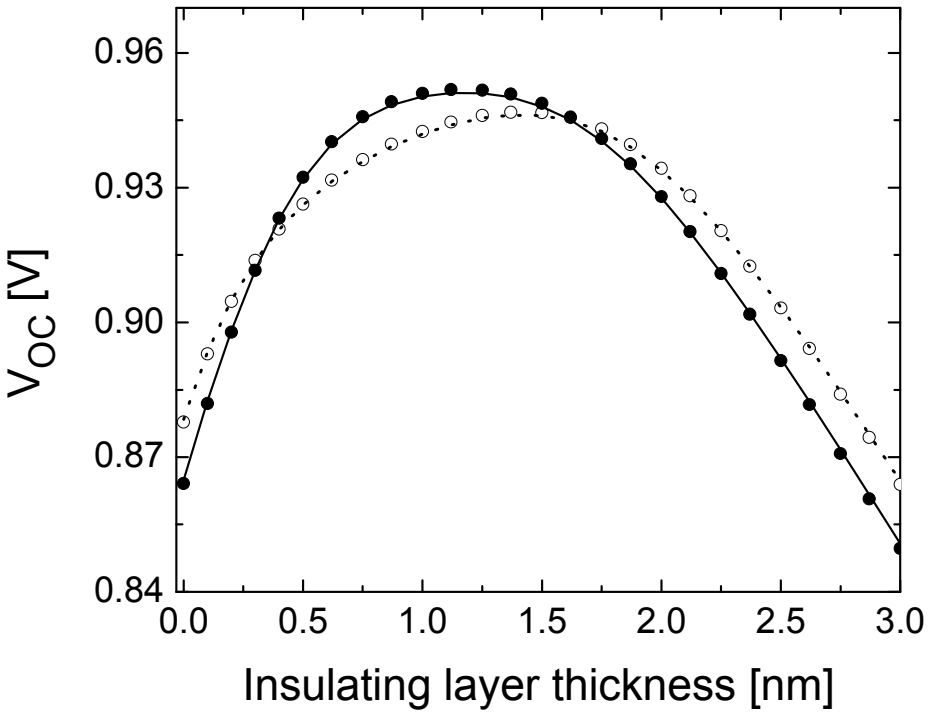

FIG. 3.3. Calculated open-circuit voltages as a function of the insulating layer thickness. The circles are simulation results from the numerical device model. The lines are analytical results from equation (3.7). The open circles (dotted line) and filled circles (solid line) represent the corresponding sets of device parameters shown in TABLE 3.1.

two processes balance and the following equation is satisfied:

$$np - \frac{n_0 p_0}{N_{CT0}} N_{CT} \approx 0 \tag{3.5}$$

n_0, p_0 and N_{CT0} are the equilibrium values of electron, hole and charge-transfer excitation densities, respectively. Evidently, equation (3.5) is satisfied in equilibrium (detailed balance). Under non-equilibrium conditions, the product of n and p is related to their equilibrium values through the difference between the electron and hole quasi-Fermi levels.

$$np = n_0 p_0 \exp\left(\frac{\Delta E_F}{kT}\right) = n_0 p_0 \exp\left(\frac{eV}{\eta_I kT}\right) \tag{3.6}$$

η_I is the ideality factor, which is the difference of quasi-Fermi levels at the interface divided by the applied voltage V across the device. From equations (3.5) and (3.6) the open-circuit voltage can be approximated as:

$$V_{OC} \approx \eta_I kT \ln\left(\frac{np}{n_0 p_0}\right) = \eta_I kT \ln\left(\frac{N_{CT}}{N_{CT0}}\right) \tag{3.7}$$

In the example device $\eta_I = 1.04$. Following the discussions on the short-circuit current, as the insulating layer thickness increases, N_{CT}/N_{CT0} first increases due to the decrease of N_{CT0} and the suppression of CTR , and subsequently decreases because the ED rate (the supply of charge-transfer state) decreases. The open-circuit voltage follows a similar behavior as N_{CT}/N_{CT0}.

3.5 Fill factor and power efficiency

The fill factor, FF, is defined as $V_M I_M / V_{OC} I_{SC}$, where $V_M I_M$ is the maximum power output in the current-voltage characteristics. The calculated fill factors are shown in FIG.

3.4. As the numerical model does not include any series or parallel resistances, the calculated fill factors are higher than experimental results,[115] and the insulating layer does not affect the fill factor significantly (~ 1%).

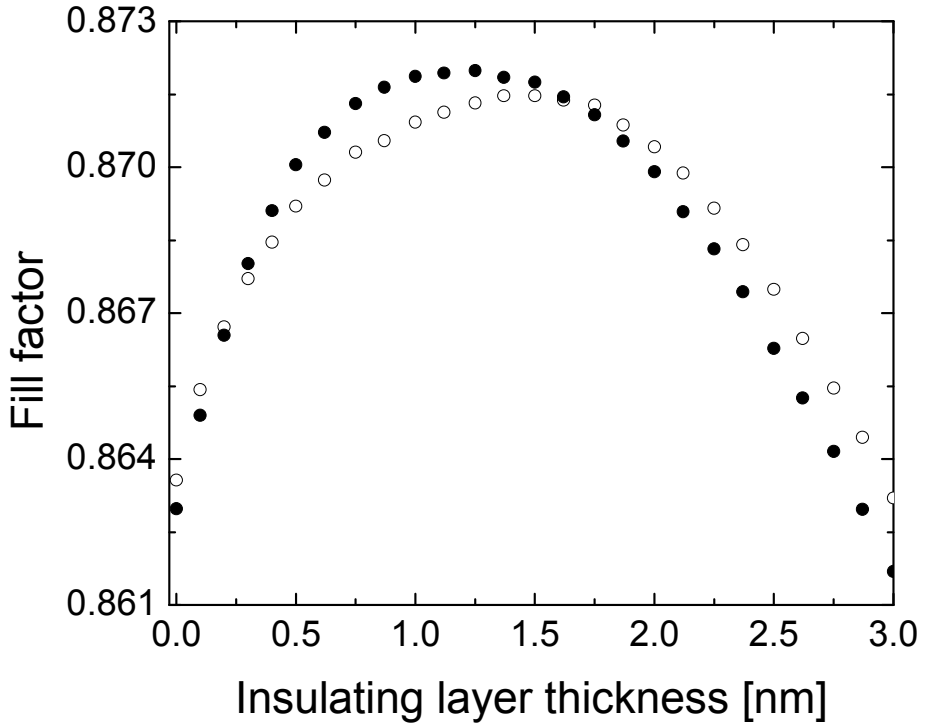

FIG. 3.4. Calculated fill factors as a function of the insulating layer thickness. The circles are simulation results from the numerical device model. The open and filled circles represent the corresponding sets of device parameters shown in TABLE 3.1.

FIG. 3.5 shows the calculated power efficiency from the numerical simulation as a function of the insulating layer thickness. From the discussions above, the insulating layer can improve the short-circuit current and the open-circuit voltage, and does not affect significantly the fill factor, therefore, the power efficiency is improved. (By as much as 50% for the open circles and 600% for the filled circles, depending on specific

parameters) The power efficiency is calculated assuming that the singlet exciton energy in tetracene is 2.32 eV.[95] The calculated power efficiency is higher than the

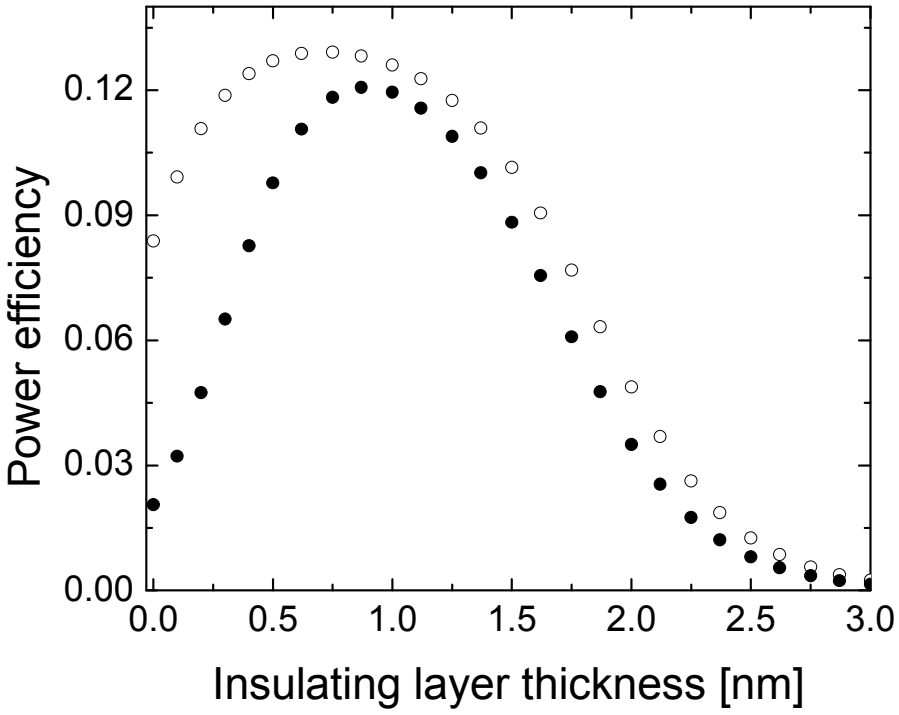

FIG. 3.5. Calculated power efficiencies as a function of the insulating layer thickness. The circles are simulation results from the numerical device model. The open and filled circles represent the corresponding sets of device parameters shown in TABLE 3.1.

experimental results for organic solar cells[116] because in the calculation, (1) the incident light is assumed to be monochromic and all the photons are absorbed in the device; (2) the calculation does not include any series or parallel resistance. The power efficiency is not only limited by the factors discussed above such as η_{ET}, η_{ED}, η_{CTD}, and FF. As the charge-transfer states have a lower energy than the excitons, the energy lost from this difference also reduces the power efficiency.

3.6 Conclusion

We have shown theoretically that the incorporation of a thin insulating layer can improve the efficiency of organic photovoltaic devices. By suppressing the charge-transfer state recombination and enhancing its dissociation, the electron and hole generation becomes more efficient. As a result, the short-circuit photocurrent and the open-circuit voltage both increase and the device has better performance. The original device structure is maintained and the device performance can be tuned independently by designing an optimized bilayer structure or by choosing appropriate insulating materials.

The insulating layer incorporation provides one option for interface control. However, the idea of tuning the rates of different processes by interface engineering has also led to other approaches. For example, charge and exciton kinetics can be modified by optimization of the interface morphology.[117] For bulk heterojunction devices, the interface processes may be controlled by introducing a block copolymer linking the donor and acceptor phases.[118]

Chapter 4 Analytical theory of magnetoelectroluminescence in organic heterojunction light-emitting devices

4.1 Introduction

Organic light-emitting devices (OLEDs) are potential candidates for future display technologies due to advantages such as high contrast ratio, light weight, and flexibility. In addition, the field of spintronics has recently expanded into the organic semiconductor realm because of relatively long spin coherence times, which is a critical requirement for applications such as organic spin valves.[119-122] Exploration of the modulation of OLED light emission by an applied external magnetic field combines these two areas of research.[123-132] An increase in electroluminescence of up to 10% in small magnetic fields has been observed in experiments,[123,128,129,131] and the physics originating from the hyperfine interaction between electron/hole polarons and hydrogen nuclei in the host molecules has begun to be explored.[133,134] The study of magnetoelectroluminescence (MEL) also has potential for the development of organic semiconductor spintronics and for adding insight into the physics of charge carriers in the organic semiconductors and at organic/organic interfaces. In this chapter, we present an analytical model for MEL using a spin density matrix approach. After establishing rate equations for the relevant microscopic processes, we obtain steady-state solutions. We explore theoretically the competition between the hyperfine interaction, which expedites

spin mixing, and the Zeeman effect which tends to suppress it. We then compare our results with experimental data on BPhen/m-MTDATA heterojunction OLEDs.

4.2 Theory

A schematic diagram of the donor/acceptor interface of an OLED is shown in FIG. 4.1. An electron (hole) and its host acceptor (donor) molecule form an electron (hole) polaron. Under forward bias, the electron and hole polarons move towards the acceptor/donor interface, where polaron pairs may form due to their mutual Coulomb attraction. A polaron pair (PP) is envisioned as a relatively weakly bound state in which the electron and hole polarons reside on different molecules in relatively close but not necessarily immediate proximity. A PP can relax to a more tightly bound state with lower energy called an exciplex.[48,49] In the exciplex state the electron/hole polarons reside on acceptor/donor molecules that are immediate neighbors. The exciplex may eventually decay radiatively (resulting light emission) or non-radiatively. In different systems other processes may occur. For example, an electron or hole may overcome the interfacial energy barrier and form a PP in one material, followed by relaxation to a bulk exciton and subsequent radiative or non-radiative decay. The model presented below is generally applicable to both cases, but to be specific, the following discussions are based on the "interface" processes sketched in FIG. 4.1(a).

Assuming non-polarized carrier injection from the contacts, the spins of the electron and hole polarons are randomly oriented with two possible values, up (↑) and down (↓). For the PPs, we consider the spin configurations parallel (↑↑, ↓↓) and antiparallel (↑↓, ↓↑) as the basis set. The first (second) arrow denotes the electron (hole) spin. As the interaction between the two polarons in the PP state is relatively weak, the

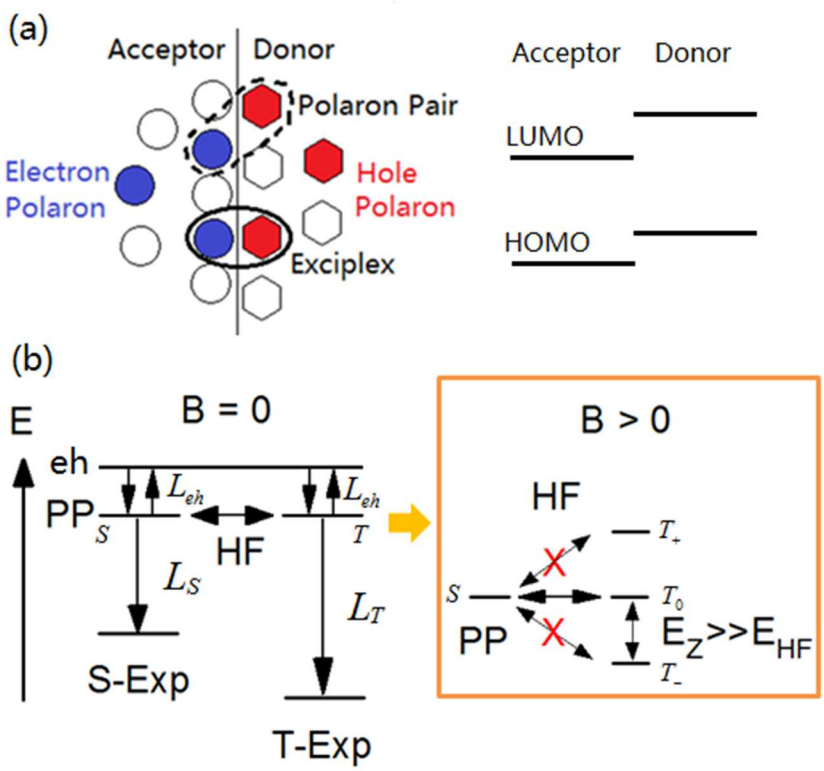

FIG. 4.1. (a) Schematic of the acceptor/donor interface and its band diagram. (b) The energy levels and critical processes in a heterojunction OLED. An external magnetic field tends to suppress spin mixing in PP states. HF denotes the hyperfine interaction, S-Exp and T-Exp are short for singlet and triplet exciplexes, e,h stands for electron and hole polarons, and other acronyms are explained in the text.

exchange coupling between two spins can be neglected for the moment. (This effect is incorporated into the theory in section 4.4.) In the PP state different spin configurations have approximately the same energy at zero magnetic field. However, in the exciplex state, a strong Coulomb interaction leads to a significant exchange splitting between singlet and triplet states. As shown in FIG. 4.1(b), the exciplex energy levels for singlet and triplet states are therefore different, and the exciplex formation rates from the polaron pair (L_S and L_T) are also different.

The PP state is an important intermediate step, in which spin flips (intersystem crossing) may occur without changing the energy significantly if there is no applied magnetic field. The most important mechanism for spin flips in the organic semiconductors under consideration is the hyperfine interaction between the polarons and (typically many) hydrogen nuclei in the molecules.[131,133,134] In this chapter, the hyperfine interaction is assumed to be isotropic; therefore the MEL is independent of the direction of the magnetic field. The spin-orbit interaction is negligible due to the light elements (C, H, O) composing the molecules.[134] (Exceptions like molecules containing heavy metal atoms[135,136] are not considered here, but in principle one can expand the dimension of the Hilbert space to include the orbital angular momentum.) When an external magnetic field is present, the Zeeman effect splits the energy levels of the different PP states. In general, the mixing of states due to the hyperfine interaction is then suppressed, resulting in a magnetic-field dependence of the luminescence (FIG. 4.1(b)). On the other hand, due to the large exchange splitting, the exciplex states do not mix.

The observed luminescence is the result of recombination of a large number of singlet exciplexes generated from their precursor PP states. A convenient tool with which to describe the relevant ensemble of polaron pair states is a density matrix, which has been employed previously for modeling the magnetoresistance of organic semiconductors.[137,138] The four dimensional PP spin Hilbert space in this study is spanned by the combination of electron and hole polaron spin states. The system Hamiltonian includes both the Zeeman (H_Z) and the hyperfine (H_{HF}) interaction. We choose the Zeeman interaction as the 0th order Hamiltonian and the hyperfine interaction as a perturbation. The two terms are expressed as:[134,139]

$$H_Z = \sum_n Q_n(t) H_Z^n \tag{4.1a}$$

$$H_{HF} = \sum_n Q_n(t) H_{HF}^n \tag{4.1b}$$

$$H_Z^n = \frac{g\mu_B}{\hbar} \vec{B} \cdot \left(\vec{S}_h^n + \vec{S}_e^n \right) \tag{4.1c}$$

$$H_{HF}^n = \sum_{i_n} \left| \psi_e(r_{i_n}) \right|^2 a_{i_n} \vec{S}_e^n \cdot \vec{N}_{i_n} + \sum_{k_n} \left| \psi_h(r_{k_n}) \right|^2 a_{k_n} \vec{S}_h^n \cdot \vec{N}_{k_n} \tag{4.1d}$$

Here n labels the various molecular pair sites that can support a polaron pair state, $Q_n(t)$ is unity if the molecular pair n is occupied by a polaron pair at time t and zero otherwise. $Q_n(t)$ describes the fact that the polaron pair resides on the site n for a finite period of time and the local hyperfine and external magnetic fields interact coherently with the polarons only during that time (properties of $Q_n(t)$ are discussed in the Appendix C). $g \approx 2$ is the electron/hole g-factor.[140] μ_B is the Bohr magneton. $\vec{S}_{e,h}^n$ is the (electron, hole) polaron spin on molecular pair n, i_n and k_n label the nuclei that interact with the electron

and hole spin at the polaron pair site n; $\left|\psi_{e,h}\left(r_{i_n,k_n}\right)\right|^2$ is the squared (electron, hole) wavefunction evaluated at the nuclear position; $\vec{N}$ is the nuclear spin, and a is the hyperfine coupling constant. $\vec{B}$ is the external magnetic field. The polaron pair state can form an exciplex state or dissociate into separated electron and hole polarons.

The time evolution of the density matrix, ρ, for the PP ensemble is described by a stochastic Liouville equation:[141]

$$\frac{d\rho}{dt} = \frac{i}{\hbar}[\rho, H_Z + H_{HF}] + \left.\frac{\partial\rho}{\partial t}\right|_{eh} + \left.\frac{\partial\rho}{\partial t}\right|_{EP} \tag{4.2}$$

$\left.\frac{\partial\rho}{\partial t}\right|_{eh}$ is the formation rate of PPs from independent electron and hole polarons and the possible dissociation of the polaron pairs back to independent electron and hole polarons. Assuming charge conservation and spin randomness, this term can be written as:

$$\left.\frac{\partial\rho}{\partial t}\right|_{eh} = RI - L_{eh}\rho \tag{4.3a}$$

R is the rate constant for forming polaron pairs from independent electrons and holes, I is the identity operator and L_{eh} is the dissociation rate constant for polaron pairs. The dissociation rate for polaron pairs is assumed to be independent of polaron spin. $\left.\frac{\partial\rho}{\partial t}\right|_{EP}$ describes the rate of exciplex formation from PPs. It is proportional to the PP density, and can be written as:[133]

$$\left.\frac{\partial\rho}{\partial t}\right|_{EP} = -\frac{1}{2}(\Lambda\rho + \rho\Lambda) \tag{4.3b}$$

$\Lambda = \sum_{\lambda} L_{\lambda} |\lambda\rangle\langle\lambda|$ is the projection operator. $\lambda = S$, T_0, T_+, or T_- labels four exciplex states. The singlet state (S) and triplet states (T_0, T_+, T_-) are defined as $S = \frac{1}{\sqrt{2}}(\uparrow\downarrow - \downarrow\uparrow)$, $T_0 = \frac{1}{\sqrt{2}}(\uparrow\downarrow + \downarrow\uparrow)$, $T_+ = \uparrow\uparrow$, and $T_- = \downarrow\downarrow$. L_S and L_T (same for three triplet states[133]) are the singlet and triplet exciplex formation rate constants. It is convenient to define the rate constants $K_{S,T} = L_{eh} + L_{S,T}$. No magnetic field effects on the electroluminescence can arise if $K_S = K_T$, consequently, these quantities cannot be completely dominated by L_{eh}.

To find the steady state solution for ρ, Bloch-Wangsness-Redfield theory is employed.[142-145] After lengthy but straight-forward derivation (shown in Appendix A), analytical results for the ρ matrix elements are obtained in equations (4.4).

$$\rho_{22} = \rho_{33} = \frac{2\left[K_T + 2\left(J_O^h + J_O^e\right)\right]R}{\left(K_S + 3K_T\right)\left(J_O^h + J_O^e\right) + K_T\left(K_S + K_T\right) - \frac{\left(K_S - K_T\right)^2\left(J_O^h + J_O^e + K_T\right)}{2\left(J_O^h + J_O^e\right) + 4\left(J_S^h + J_S^e\right) + K_S + K_T}} \quad (4.4a)$$

$$\rho_{23} = \rho_{32} = \frac{K_S - K_T}{2\left(J_O^h + J_O^e\right) + 4\left(J_S^h + J_S^e\right) + K_S + K_T}\rho_{22} \quad (4.4b)$$

$$\rho_{11} = \rho_{44} = \frac{R + \left(J_O^h + J_O^e\right)\rho_{22}}{J_O^h + J_O^e + K_T} \quad (4.4c)$$

Subscripts 1 to 4 denote spin configurations: 1 = ↑↑, 2 = ↑↓, 3 = ↓↑, and 4 = ↓↓. All other matrix elements are equal to zero in a steady state. The J terms describe rates of spin mixing, which originate from spin correlation between states at time t and $t + \tau$. (We use J as a generic symbol for J_O^e, J_O^h, J_S^e, and J_S^h.) During the time interval τ, the PP experiences random perturbation due to the hyperfine interaction because the electron

and hole polarons interact with different nuclei as they hop from molecule to molecule. The J term in general can be expressed as: (Appendix A)

$$J = \frac{\alpha E_{HF}^2}{\hbar^2} \int f\left(|\tau|/\tau_0\right) e^{i\tau\Delta E/\hbar} d\tau \tag{4.5}$$

Here $E_{HF} = g\mu_B B_{HF}$ defines the energy scale of the hyperfine interaction, and ΔE is the Zeeman energy difference between the initial and final states. (In principle, the dynamics of the nuclear spins could also contribute to the time dependence of the correlation function f, but nuclear spin dynamics is slow compared to the polaron hopping times and therefore is not the important consideration.) For the J terms in equations (4.4), the superscripts denote the electron (e) and hole (h) polarons, the subscripts O and S indicate whether a spin flip occurs (*Opposite spin*, in this case $\Delta E = g\mu_B B$) or not (*Same spin*, in this case $\Delta E = 0$) during the time interval τ. The prefactor α equals 2/3 for the opposite spin case and 1/3 for the same spin case, which results directly from the statistical average of off-diagonal (x, y) and diagonal (z) terms in the Pauli matrices.

The function $f(|\tau|/\tau_0)$ in equation (4.5) is the correlation function. It is even and monotonically decreases with τ, because under random perturbations the final state gradually loses its relationship to the initial state. τ_0 describes the relevant time scale for this process. Specific forms of $f(|\tau|/\tau_0)$ are discussed in the Appendix C. Two forms for the correlation functions are considered:

$$\text{Type I: } F\left\{f\left(|\tau|/\tau_0\right)\right\} = \frac{2\tau_0}{1+\tau_0^2\omega^2} \tag{4.6a}$$

$$\text{Type II: } F\left\{f\left(|\tau|/\tau_0\right)\right\} = \frac{2\tau_0}{1+\tau_0|\omega|} \tag{4.6b}$$

Here $F\{f(|\tau|/\tau_0)\}$ is the Fourier transform of $f(|\tau|/\tau_0)$. The type I function corresponds to the assumption of a single relaxation time, τ_0.[142] The type II function is consistent with the 1/*frequency* (= $2\pi/\omega$) noise power spectrum that is frequently observed experimentally.[146,147] It can be the result of a range of relaxation times determining the time-decay of the correlation function.[148] Combining equations (4.5) and (4.6) the correlation terms can be written explicitly as:

$$\text{Type I: } J_O^{(e,h)} = \frac{4E_{HF(e,h)}^2}{3\hbar^2} \frac{\tau_{0(e,h)}}{1+\frac{g^2\mu_B^2\tau_{0(e,h)}^2}{\hbar^2}B^2}, \; J_S^{(e,h)} = \frac{2E_{HF(e,h)}^2}{3\hbar^2}\tau_{0(e,h)} \tag{4.7a}$$

$$\text{Type II: } J_O^{(e,h)} = \frac{4E_{HF(e,h)}^2}{3\hbar^2} \frac{\tau_{0(e,h)}}{1+\frac{g\mu_B\tau_{0(e,h)}}{\hbar}|B|}, \; J_S^{(e,h)} = \frac{2E_{HF(e,h)}^2}{3\hbar^2}\tau_{0(e,h)} \tag{4.7b}$$

The four exciplex formation rates are obtained by combining the PP density matrix elements with corresponding formation rate constants:

$$\chi_S = L_S(\rho_{22} - \rho_{23}) \tag{4.8a}$$

$$\chi_{T0} = L_T(\rho_{22} + \rho_{23}) \tag{4.8b}$$

$$\chi_{T+} = L_T\rho_{11} \tag{4.8c}$$

$$\chi_{T-} = L_T\rho_{44} \tag{4.8d}$$

The singlet exciplex formation rate fraction is obtained as:

$$Frac(\chi_S) = \frac{\chi_S}{\chi_S + \chi_{T0} + \chi_{T+} + \chi_{T-}} \tag{4.9}$$

The denominator in this expression is independent of the magnetic field, and, to the extent that dissociation of polaron pairs into independent polarons is negligible, equal to 4*R*.

The magnetic field effect (MFE) on the singlet exciplex density formed may be defined as:

$$MFE(B) = \frac{\chi_S(B) - \chi_S(B=0)}{\chi_S(B=0)} \tag{4.10}$$

After formation, the singlet/triplet exciplex states may decay radiatively or nonradiatively with different lifetimes.

It has been suggested in recent work that the singlet-triplet exciplex splitting at a particular organic/organic interface may be relatively small, thus allowing for thermally-activated intersystem crossing.[149] These processes may alter the singlet/triplet exciplex ratio and therefore affect the luminescence. Assuming a fraction $0 < P < 1$ of the triplet exciplexes transform into singlets, the overall singlet exciplex formation rate is given by:

$$\chi_S' = \chi_S + (\chi_{T0} + \chi_{T+} + \chi_{T-})P = \chi_S(1-P) + 4RP \tag{4.11}$$

The singlet-triplet exciplex splitting in the work cited above[149] was estimated to be 50 meV. Hence, for the magnetic field range of interest (~ 100 mT, corresponding to ~ 10 μeV), *P* is expected to be independent of the magnetic field. Therefore,

$$MFE'(B) = \frac{\chi_S'(B) - \chi_S'(0)}{\chi_S'(0)} = [\chi_S(B) - \chi_S(0)]\frac{1-P}{\chi_S'(0)} = MFE(B)\frac{\chi_S(0)}{\chi_S'(0)}(1-P) \tag{4.12}$$

The result shows that shape of the *MFE*'(*B*) curve is identical to that of the *MFE*(*B*) curve, the two differing only by a constant scaling factor.

4.3 Results and discussion

In order to use the theoretical model for MEL calculations, a rough estimate of the parameters is required. It is useful to introduce an effective (Overhauser) magnetic field that characterizes the strength of the hyperfine interaction described by $H_{HF} \sim g\mu_B B_{HF}$. Prior literature suggests that this field is on the order of several millitesla for organic molecules,[133,134] and a number of 5 mT is used in the following calculations. A first estimate of the correlation time scale, τ_0, is 2 ns, and we assume it to be the same for electron and hole polarons.[150,151] The singlet exciplex formation rate constant is taken to be $(0.6\ \text{ns})^{-1}$.[51,106,110]

In FIG. 4.2, the singlet exciplex fraction is plotted as functions of the ratio K_T/K_S and B_{HF}. For fraction plots in this chapter, we assume $K_T/K_S = L_T/L_S$ for simplicity. The external magnetic field is zero. The results are consistent with numerical simulations shown in FIG. 2(a) of reference 133. When the hyperfine interaction is negligible (from point A to point B), there is no mechanism for spin perturbation hence the singlet/triplet ratio is constant and equal to 1/3. In this case, exciplex formation dominates over spin mixing. When $K_T/K_S = 1$ (from point C to point D), the singlet/triplet ratio also maintains the value of 1/3 regardless of the hyperfine field strength. In this case, the model does not distinguish between singlet and triplet exciplex states because their formation rate constants are equal. When the hyperfine interaction is strong and K_T is not equal to K_S, the singlet/triplet exciplex ratio is determined by K_T/K_S. In that case the four

PP spin states are sufficiently mixed by the hyperfine interaction before exciplex formation can occur. An external magnetic field suppresses the spin mixing due to the

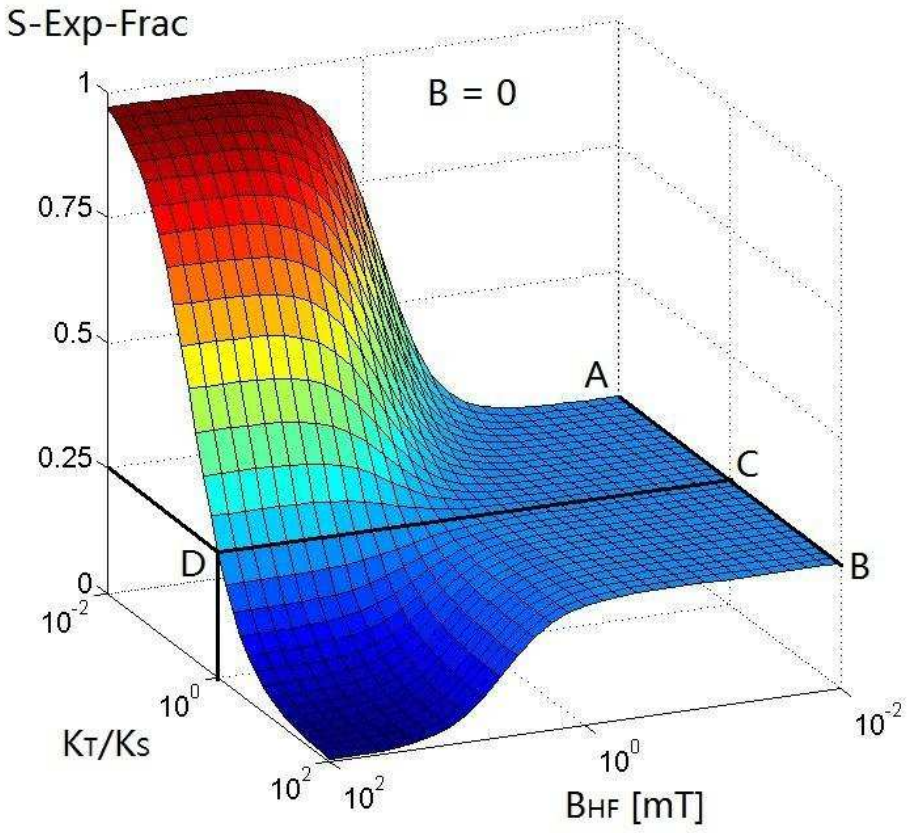

FIG. 4.2. Singlet exciplex fraction plotted as functions of the triplet/singlet formation rate and the strength of the hyperfine interaction. The external magnetic field is zero. The parameters are shown in the text.

hyperfine interaction, hence $K_T/K_S > 1$ is required for a positive MEL (Increased electroluminescence with increasing magnitude of the magnetic field). This study provides some physical insight into the statistical 25% limit often cited for OLED efficiency.

The singlet and triplet exciplex fraction as a function of the external magnetic field is shown in FIG. 4.3. Here $K_T/K_S = 1.5$. The hyperfine field B_{HF} is set large enough (50 mT) for sufficient PP spin mixing to occur in the absence of an applied magnetic

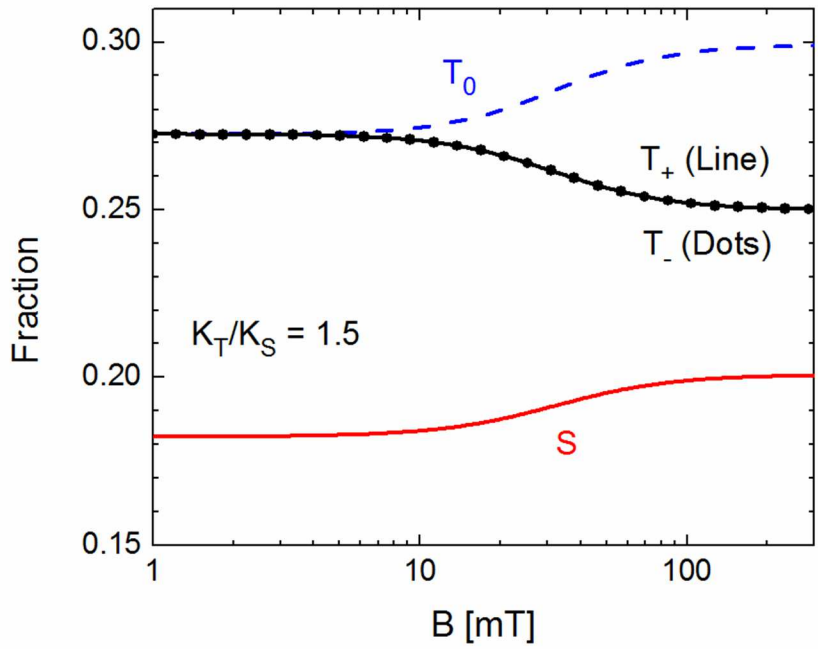

FIG. 4.3. Fraction of singlet and triplet exciplex states as a function of an external magnetic field. The hyperfine interaction is set to a large value (50 mT) to ensure sufficient spin mixing at zero magnetic field. The correlation function used is type I. Other parameters are the same as in FIG. 4.2.

field. We choose the correlation function in the calculation to be of type I. At zero magnetic field, the singlet and triplet PP spin states (the definitions are the same as for the corresponding exciplex states) have the same energy. The strong hyperfine

interaction leads to substantial spin mixing among all four states. Their fractions are determined by $\chi_{T0} = \chi_{T+} = \chi_{T-} = \chi_T$, $\chi_T/\chi_S = K_T/K_S$, and $\chi_S + 3\chi_T = 1$. As the magnetic field

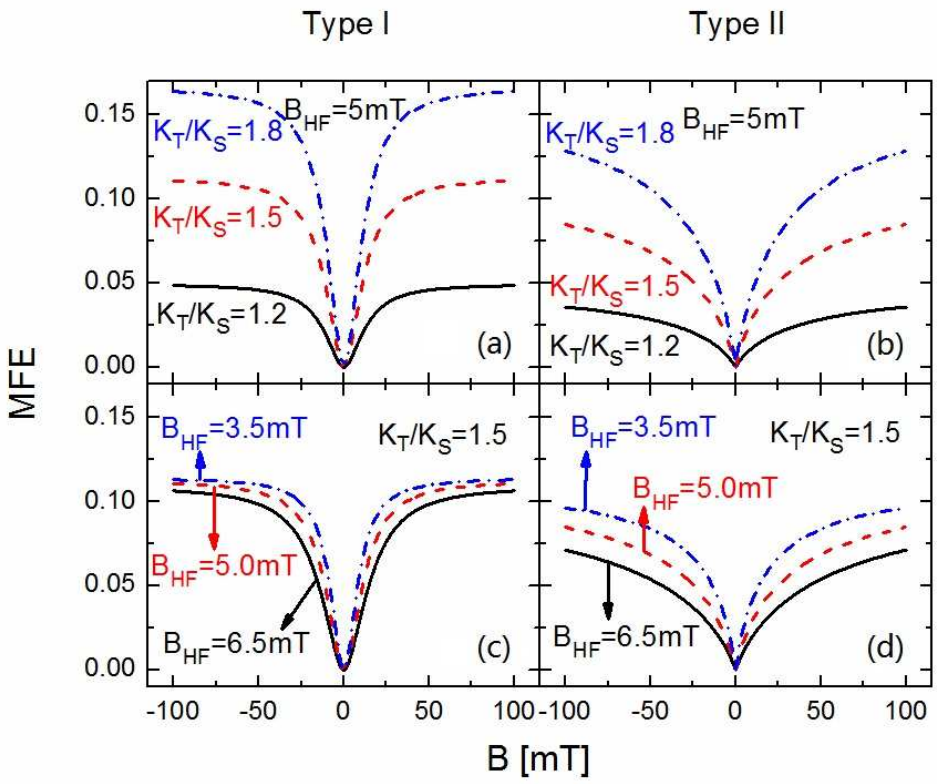

FIG. 4.4. Calculated MFE as a function of the magnetic field, varying three parameters: the hyperfine interaction strength B_{HF}, the ratio of triplet/singlet exciplex formation rates K_T/K_S, and the type of correlation function. MFE is defined in equation (4.10). The thermally-activated intersystem crossing is assumed to be zero.

increases, the Zeeman effect splits the energy degeneracy, and the effect of the hyperfine interaction is gradually suppressed. When the external magnetic field is strong, the energies of T_+ and T_- states are very different from that of the T_0 and S states, hence spin flips are suppressed and the exciplex fractions are determined simply by the number of

possible states, i.e. both are equal to 1/4. On the other hand, T_0 and S states are still at the same energy level. The strong hyperfine interaction determines their fraction through

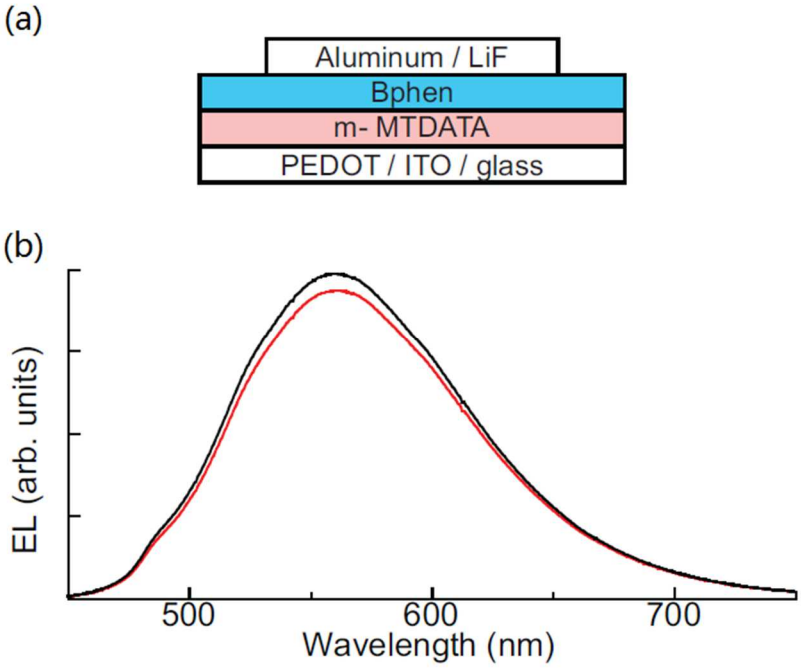

FIG. 4.5. (a) Schematic device structure in experiment. (B) Measured electroluminescence spectra when the external magnetic field is 0 (Red) or 100 mT (black). Experimental data are courtesy of Dr. Scott A. Crooker et al. at Los Alamos National Laboratory.

$\chi_{T0}/\chi_S = K_T/K_S$ and $\chi_S + \chi_{T0} = 0.5$. In this calculation T_+ and T_- states are symmetric therefore their fractions are always equal. (More discussion is presented in section 4.4.)

The MFE curves calculated from equation (4.10) are plotted as a function of the external magnetic field in FIG. 4.4. The parameters varying are the hyperfine interaction

strength B_{HF}, the ratio of triplet/singlet exciplex formation rates K_T/K_S, and the type of correlation function. The values used in the calculation are shown in the plots. The results show that the depth of the MFE curve is primarily determined by K_T/K_S and the width is determined by B_{HF}. The difference between the two types of correlation functions is the quadratic or linear dependence on the magnetic field. The MFE curves with type I function saturate faster than those with type II function as the magnitude of the field increases. As outlined in the discussion of equations (4.11) and (4.12), the amplitude of the magnetic field modulation of the luminescence may also be affected by intersystem crossing between the exciplex states. Here we fix $P = 0$ and vary the K_T/K_S ratio to fit the measurements, but equally good fits can be achieved fixing that ratio and varying P.

In the following, the model developed above is applied to the heterojunction OLED structure shown in FIG. 4.5 (a). The Al/LiF layer is the cathode and the PEDOT/ITO/glass layer is the anode. BPhen is the acceptor (electron transport layer) and m-MTDATA is the donor (hole transport layer). Under forward bias, light emission occurs due to singlet exciplex recombination at the BPhen/m-MTDATA interface. The measured electroluminescence spectra for $B = 0$ (red) and $B = 100$ mT (black) are shown in FIG. 4.5 (B). More experimental details can be found in a recent paper.[56]

The measured MEL data are normalized using equation (4.10) and plotted in open circles as a function of the external magnetic field in FIG. 4.6 (a). Each curve represents a part of the luminescence spectrum integrated over the wavelength range indicated. The depth and width of the MFE curves are shown in FIG. 4.6 (b). Depth is defined as the

difference between the maximum and minimum values of the curve. The width is taken to be the half-amplitude width. It is observed that as the wavelength increases, the depth decreases while the width increases. The different MFE behaviors for different wavelength ranges originate from variations of the interfacial environment. The molecules at the interface are subject to randomly varying steric interactions with their immediate environment. Consequently, exciplexes and PP states vary locally in spatial extent and energy, giving rise to the relatively broad spectrum observed. Generally, the number of hydrogen nuclei that interact with an electron (or hole) polaron is on the order of the number of hydrogen nuclei in the host molecule. However, due to the steric complexity at the interface, the wavefunctions of an electron (or hole) polaron may vary locally in its spatial extent. Therefore the number of relevant hydrogen nuclei may vary, resulting in a variation of the hyperfine interaction experienced by polarons in PP states at different locations along the interface.[56] As a simple estimate, assuming that the hydrogen nuclei are distributed evenly in space, the term E_{HF}^2 in equation (4.5) is proportional to $\int d^3 r \left|\psi_{e,h}\left(\vec{r}\right)\right|^4 \propto \frac{1}{V}$.[139] Here $\psi_{e,h}\left(\vec{r}\right)$ is the spatial wavefunction of the electron or hole polaron in a PP state and V is the volume that characterizes its spatial extent. (From equation (4.5), B_{HF} is then proportional to $1/\sqrt{V}$.) Incorporating this

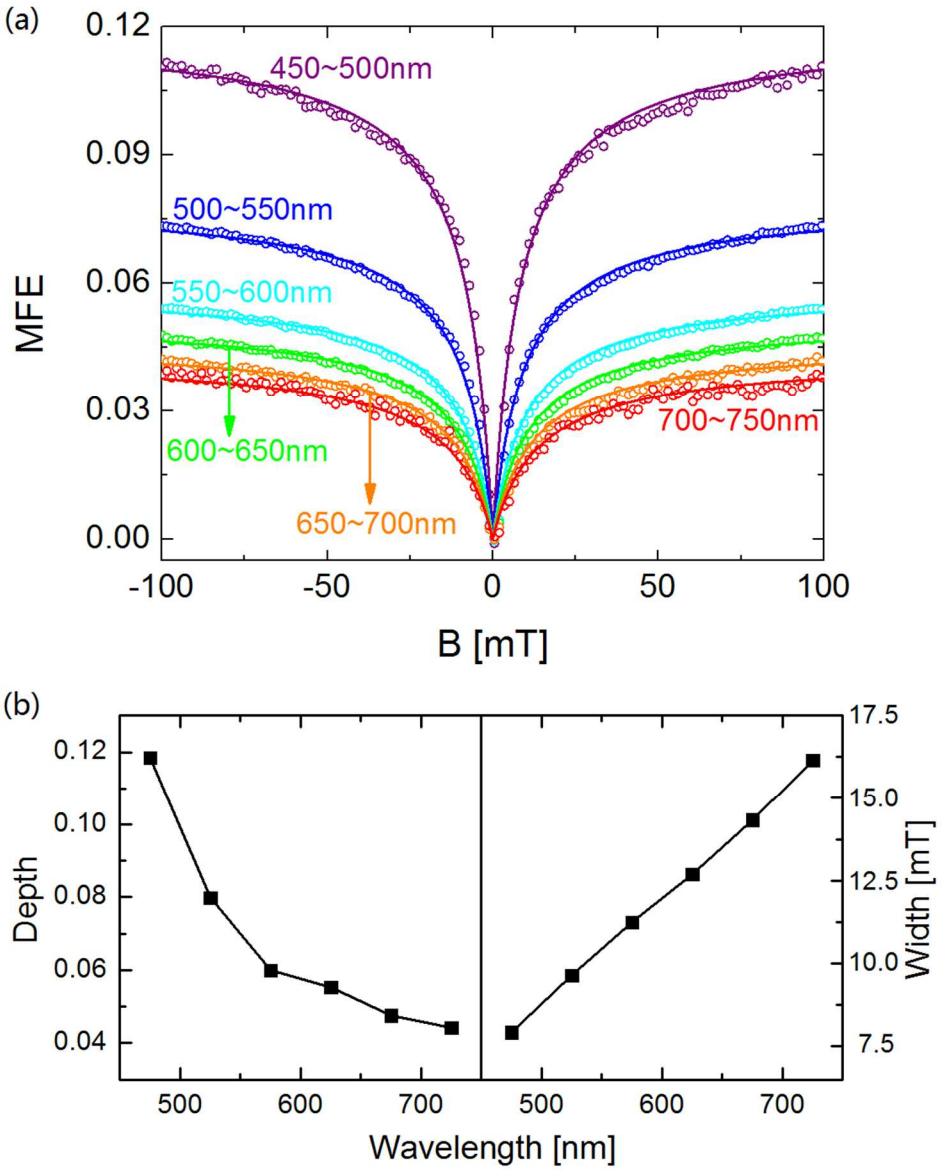

FIG. 4.6. (a) Dots: Measured electroluminescence as a function of the magnetic field. MFE is defined in equation (4.10). Lines: Corresponding model calculation results using a type II correlation function. The parameters are shown in Table 4.1. (b) The depth and width of the MFE curves as a function of the wavelength. Experimental data are courtesy of Dr. Scott A. Crooker et al. at Los Alamos National Laboratory.

effect, the correlation terms in equation (4.5) have dependence on V that is written as:

$$J = \frac{\tilde{J}}{V} \tag{4.13}$$

$\tilde{J}$ is a generic quantity that depends on the spatial density of hydrogen nuclei. For simplicit, in the calculation $\tilde{J}$ is assumed to be the same for donor and acceptor materials. Incorporating equation (4.13) into the model, we can fit the experimental data with appropriate parameters. τ_0 = 2 ns and K_S = (0.6 ns)$^{-1}$ are used from the previous discussions. The two parameters that vary among the different curves are V (normalized by the 550 ~ 600 nm curve, which we choose to define a reference value V_{ref}) and K_T/K_S.

TABLE 4.1. Parameters used in fitting experimental data of FIG. 4.6 (a)

Wavelength	$r = \left(\frac{V}{V_0}\right)^{\frac{1}{3}}$ (with respect to the 550~600nm curve)	K_T/K_S
450-500 nm	1.14	1.74
500-550 nm	1.06	1.4
550-600 nm	1	1.27
600-650 nm	0.95	1.23
650-700 nm	0.9	1.2
700-750 nm	0.85	1.18

The parameter values for all the curves are shown in TABLE 4.1. In fitting the data, the type II correlation function is used because it shows better agreement with experimental

data than the type I function. The model calculation results are shown as lines in FIG. 4.6 (a). Lower energies of the emitted photons correspond to more compact states; therefore the polarons interact with fewer nuclei.[56]

4.4 Incorporation of exchange coupling in polaron pair states

Some magneto-luminscence experiments for organic semiconductors reveal a fine structure in the MFE for very low magnetic fields (< 2 mT). The MFE consists of a slight decrease in luminescence before a substantial increase.[133,134,152] This observation implies that the effect of the hyperfine interaction does not decrease monotonically with

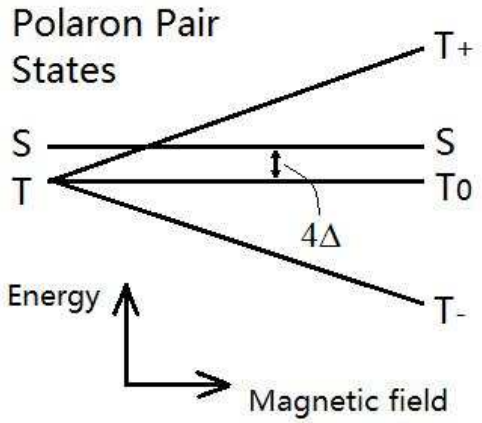

FIG. 4.7. Schematic of the PP energy levels as a function of an external magnetic field, including energy split due to exchange coupling.

increasing magnetic field. Considering that the magnetic field determines the Zeeman energy and the low-field structure occurs at very weak fields, a reasonable explanation is

that a weak exchange interaction in the PP state lifts the degeneracy of the singlet and triplet states, as shown in FIG. 4.7. The small energy difference is due to the relatively weak coupling of the electron and the hole polarons in the PP state. As the magnetic field increases, the magnitude of the energy difference between S and T_+ states decreases initially and increases subsequently. Therefore the correlation between the two states exhibits an initial increase followed by a decrease.

The effect of weak exchange coupling in the PP states is readily incorporated into the previous model. The new Hamiltonian of 0th order can be written as:[134]

$$H_0^n = H_Z^n + H_{PPEC}^n = \frac{g\mu_B}{\hbar}\vec{B}\cdot\left(\vec{S}_h^n + \vec{S}_e^n\right) - \frac{4}{\hbar^2}\Delta\left(\vec{S}_h^n \cdot \vec{S}_e^n\right) \tag{4.14}$$

PPEC denotes Polaron Pair Exchange Coupling. Δ describes the energy scale of the exchange coupling in PP states. Using similar derivation procedures (Appendix B), analytical expressions of the PP density matrix are obtained:

$$\rho_{22} = \frac{C_1 B_2 - C_2 B_1}{A_1 B_2 - A_2 B_1} R \tag{4.15a}$$

$$\rho_{33} = \frac{C_1 A_2 - C_2 A_1}{B_1 A_2 - B_2 A_1} R \tag{4.15b}$$

$$\rho_{11} = \frac{2R + J_O^{21}\rho_{22} + J_O^{31}\rho_{33}}{2K_T + J_O^{21} + J_O^{31}} \tag{4.15c}$$

$$\rho_{44} = \frac{2R + J_O^{42}\rho_{22} + J_O^{31}\rho_{33}}{2K_T + J_O^{42} + J_O^{31}} \tag{4.15d}$$

where

$$A_1 = \frac{J_O^{21} J_O^{31}\left(J_O^{21} - J_O^{42}\right)}{4K_T + 2J_O^{21} + 2J_O^{31}} - \frac{1}{2}J_O^{31}J_O^{21} - \frac{1}{2}J_O^{31}J_O^{42} - J_O^{31}J_S^{32} - J_O^{31}K_S - J_O^{42}J_S^{32}$$

$$B_1 = \frac{\left(J_O^{31}\right)^2\left(J_O^{21} - J_O^{42}\right)}{4K_T + 2J_O^{21} + 2J_O^{31}} + J_O^{31}J_S^{32} + J_O^{42}J_O^{31} + J_O^{42}J_S^{32} + J_O^{42}K_T$$

$$C_1 = -\frac{J_O^{31}\left(J_O^{21} - J_O^{42}\right)}{2K_T + J_O^{21} + J_O^{31}} + J_O^{42} - J_O^{31}$$

A_2, B_2, and C_2 are obtained by interchanging J_O^{21} and J_O^{42} in A_1, B_1, and C_1,respectively. The J terms are defined as:

$$J^{ab} = J^{ab(e)} + J^{ab(h)},\ J^{ab(e,h)} = \frac{\alpha E_{HF(e,h)}^2}{\hbar^2}\int f\left(|\tau|/\tau_{0(e,h)}\right)e^{i\frac{\tau}{\hbar}(E_b - E_a)}d\tau$$

The values of α are the same as those in the previous section. α = 2/3 for the case of antiparallel spins and 1/3 for the case of parallel spins. Note that for convenience the basis has been changed: 1 = T_+, 2 = S, 3 = T_0, and 4 = T_-. The corresponding energies for the 0[th]-order Hamiltonian are $E_1 = g\mu_B B - \Delta$, $E_2 = 3\Delta$, $E_3 = -\Delta$, and $E_4 = -g\mu_B B - \Delta$, where $\Delta = g\mu_B B_{PPEC}$ characterizes the exchange coupling in the PP states. The exciplex formation rates are given by:

$$\chi_S = L_S\rho_{22},\ \chi_{T0} = L_T\rho_{33},\ \chi_{T+} = L_T\rho_{11},\ \chi_{T-} = L_T\rho_{44} \tag{4.16}$$

When $\Delta \rightarrow 0$, the combination of equations (4.15) and (4.16) is identical to equations (4.4) and (4.8). The correlation functions have the same forms as in the previous section. For example, using the type I correlation function, the J terms can be written explicitly as:

$$J_O^{ab(e,h)} = \frac{4E_{HF(e,h)}^2}{3}\frac{\tau_{0(e,h)}}{\hbar^2 + \tau_{0(e,h)}^2\left(E_a - E_b\right)^2} \tag{4.17a}$$

$$J_S^{ab(e,h)} = \frac{2E_{HF(e,h)}^2}{3}\frac{\tau_{0(e,h)}}{\hbar^2 + \tau_{0(e,h)}^2\left(E_a - E_b\right)^2} \tag{4.17b}$$

FIG. 4.8 plots the exciplex fraction as a function of the magnetic field. The parameters are the same as those in FIG. 4.3. An additional B_{PPEC} = 1.4 mT ($\Delta \approx 0.16$ μeV) is incorporated into the model. We observe that there is a peak in the T_+ fraction as the magnetic field increases. This is consistent with the energy schematic in FIG. 4.7.

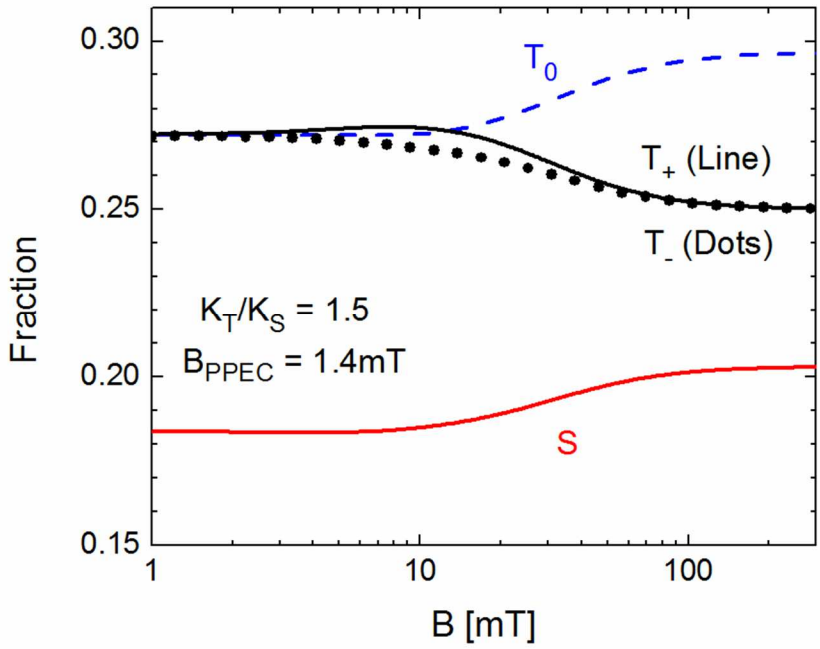

FIG. 4.8. Fractions of singlet and triplet exciplex states as a function of an external magnetic field. A 1.4 mT exchange coupling in PP states is included. The parameters are the same as in FIG. 4.3.

When the T_+ and S energy levels cross, the hyperfine interaction between them has a maximum. When a magnetic field is applied the symmetry between T_+ and T_- states is broken and χ_{T+} is no longer equal to χ_{T-} (different from FIG. 4.3). When $B >> B_{PPEC}$, the effect of PP exchange coupling is negligible and their fractions both reach 0.25.

FIG. 4.9 shows the MFE for three different exchange interaction strengths in the PP states. The corresponding energies are Δ = 0, 0.12 μeV and 0.23 μeV. The other parameters used are the same as in FIGs. 4.3 and 4.8. The result is also consistent with FIG. 4.7. Because of the weak exchange coupling in the polaron pairs, the MFE becomes

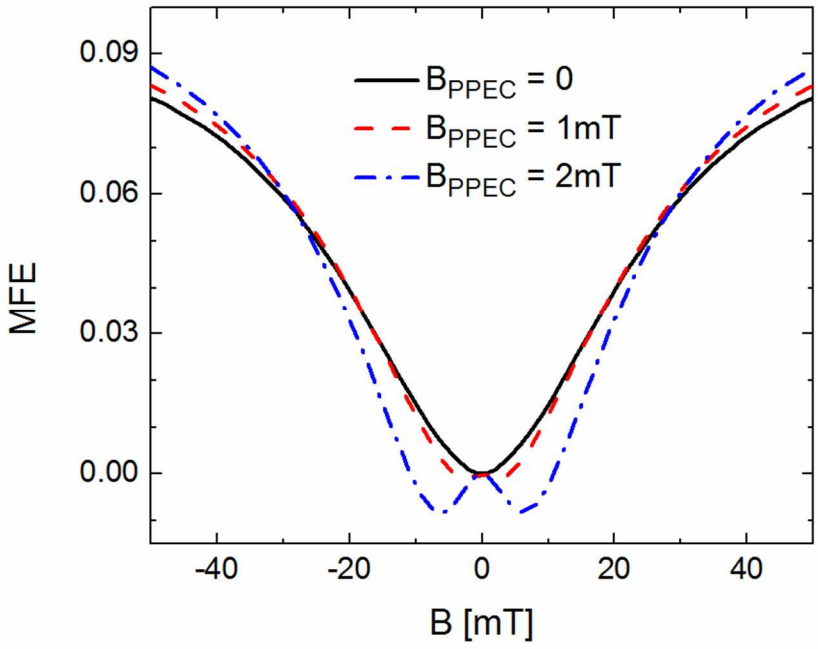

FIG. 4.9. MFE (defined in equation (4.10)) as a function of an external magnetic field. A variation of the PP exchange coupling energies is assumed for the three curves. The correlation function used is of type I. Other parameters are the same as in FIG. 4.3.

negative before it turns positive. When the exchange interaction is greater, the w-shape at low field is more significant.

4.5 Conclusion

As a final remark of this chapter, we comment on different recombination mechanisms in the OLEDs. As mentioned in section II, a polaron pair may form at the heterojunction interface or in the bulk material, resulting in formation of an exciplex or a bulk exciton. Usually an exciplex extends at least over two adjacent molecules while an exciton resides on a single molecule. Hence, the PP state involved in exciton formation is also likely to be more localized than that occurring during exciplex formation. This in turn implies that the effect of PP exchange coupling is more prominent for the bulk exciton mechanism. That is a possible explanation that the fine structure is observed in reference 131 but not in the experimental data shown in FIG. 4.6. For the type of correlation functions in that system, the experimental observations suggest that devices with exciplex recombination tend to have a type II behavior (FIG. 4.6), while devices with exciton recombination are more likely to be in the type I form.[153,154] But firm conclusions cannot be reached without further explorations.

We have presented a theoretical model for magneto-electroluminescence in organic light-emitting devices. It yields insight into the physics of the hyperfine interaction and Zeeman effect for polarons in organic molecules. It also illuminates how singlet/triplet exciplex formation rates and the spatial extent of the polaron pair control the optoelectronic properties.

Chapter 5 Coupling of channel conductance and gate-to-channel capacitance in electric double layer transistors

5.1 Introduction

Organic electric double layer transistors (EDLTs) belong to a special class of OFET in which electrolytes (e.g., ionic liquids) are used as the material between the gate and the semiconductor. The high capacitance associated with electrolyte gating facilitates the probing of transport phenomena in a variety of semiconductors at high charge carrier densities (10^{13} cm^{-2} to 10^{15} cm^{-2}), and the development of future low-

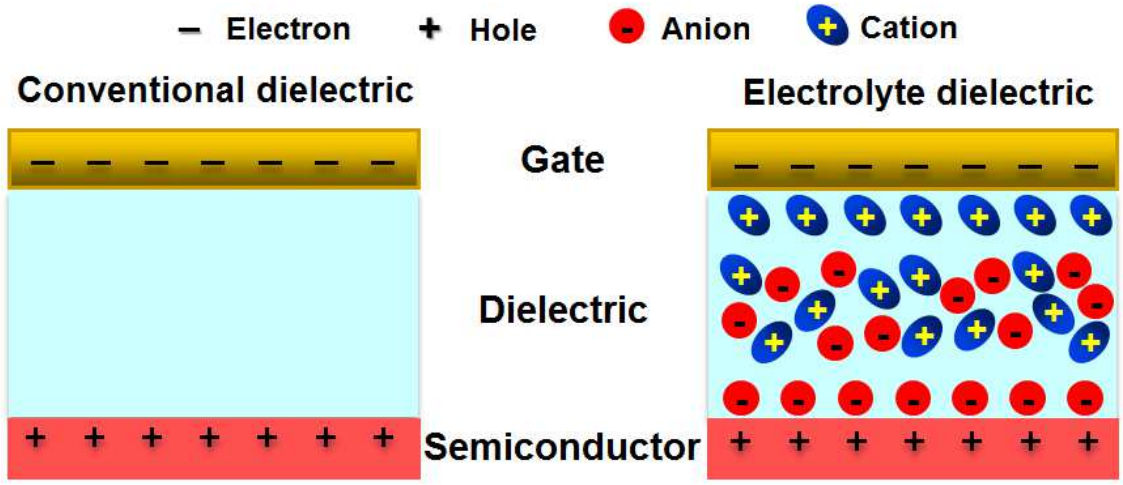

FIG. 5.1. Schematics of the metal-dielectric-semiconductor structures with conventional and electrolyte (*e.g.*, ionic liquid) dielectrics.

voltage (< 3 V), organic semiconductor electronics. The operating mechanism of EDLTs is fundamentally different from that of conventional FETs using an insulator (such as an oxide or polymer) as the dielectric material, as schematically shown in FIG. 5.1. For both conventional FETs and EDLTs, application of a negative gate voltage induces (positive) holes in the semiconductor forming a p-type conducting channel. In the former case, the gate-to-channel capacitance (per unit area) is determined by the dielectric permittivity divided by the layer thickness, while in the latter case ions in the electrolyte redistribute, which leads to an accumulation of anions (cations) at the electrolyte/ semiconductor (gate/electrolyte) interface forming two electric double layers (EDLs) of nanometer thickness. The gate voltage only drops across the EDLs and the bulk polarization is negligible due to the charge screening of the double layers. Consequently, the gate-to-channel capacitance is very large, on the order of 1 ~ 10 $\mu F/cm^2$, and it is independent of the electrolyte layer thickness.[155-166]

Despite recent achievements in electrolyte gating, device physics and electrical properties of EDLTs are not as well understood as those of conventional FETs. For example, as the motion of ions toward the interfaces appears to be slow compared to that of the charge carriers forming the conducting channel in the semiconductor, the equivalent capacitance of EDLTs has a strong dependence on frequency. Furthermore, the measured equivalent gate-to-channel capacitance may depend on the channel conductance even in the low frequency regime. In this chapter the dynamics of EDLTs is explored theoretically and results are compared with experimental data.

5.2 Model

We start by introducing the equivalent circuit model for EDLTs shown in FIG. 5.2. Similar to conventional FETs, there exists a geometric capacitance, C_{geo}, which is defined as the (intermediate frequency) permittivity of the electrolyte multiplied by the

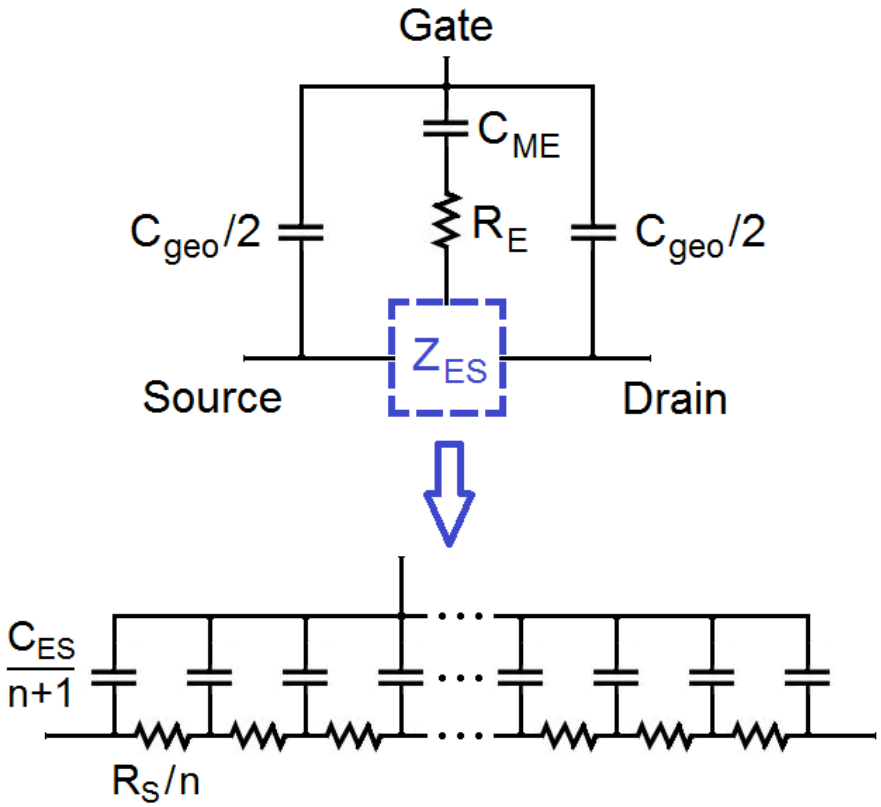

FIG. 5.2. Equivalent circuit model for EDLTs. C_{geo} is the geometric capacitance between the gate and the conduction channel, R_E is the electrolyte resistance, C_{ME} and C_{ES} are the two double-layer capacitances at the interfaces, R_S is the semiconductor channel resistance.

area of the gate/electrolyte interface and divided by the thickness of the electrolyte layer. As the electrolyte has non-zero conductivity, its resistance is finite and denoted as R_E. The key parts of the equivalent circuit model are the gate/electrolyte and the electrolyte/semiconductor interfaces where the EDLs form. Because opposite charges accumulate at these interfaces, the effect can be viewed as two capacitances, C_{ME} and C_{ES}, both much greater than C_{geo}. The resistance of the gate contact is negligible but that of the semiconductor is not. Therefore the gate/electrolyte interface is approximated as a single element, C_{ME}, while the electrolyte/semiconductor heterojunction interface is modeled as a distributed network between C_{ES} and the semiconductor resistance R_S.

The impedance of this coupled network defines the Z_{ES} shown in the lower part of FIG. 5.2. The conduction channel in the semiconductor is described by n resistors. Each resistor has the value of the channel resistance R_S divided by n. The interfacial capacitance C_{ES} is described by $n + 1$ capacitors. Each capacitor is equal to $C_{ES} / (n + 1)$. For the discussions of this chapter, we assume that the source and drain terminals are connected (short circuit). In this case, the frequency-dependent impedance Z_{ES} can be calculated analytically following a transmission-line-approach[167] by letting $n \to \infty$:

$$Z_{ES} = \frac{1}{2}\sqrt{\frac{R_S}{j\omega C_{ES}}}\coth\left(\frac{\sqrt{j\omega C_{ES}R_S}}{2}\right) \tag{5.1}$$

where ω is the (angular) frequency. In the low frequency limit, $Z_{ES} \to \frac{1}{j\omega C_{ES}} + \frac{R_S}{12}$. Its imaginary part reduces to the interfacial capacitance C_{ES}, which is the expected equivalent capacitance. Its real part can be written as $(1/4) \times R_S/3$. The $R_S/3$ part derives from the effect of the network, where the resistors near the middle have a smaller current

flow than those near the source/drain. There is a factor 1/4 because the source and drain are connected together and the whole network can be viewed as two "half devices" in parallel. In the high frequency limit, $Z_{ES} \to \frac{1}{2}\sqrt{\frac{R_S}{j\omega C_{ES}}}$. If the equivalent capacitance is determined in this limit, the result is $C_{eq} = -\frac{1}{(\mathrm{Im} Z_{ES}) \times \omega} = \sqrt{\frac{2C_{ES}}{\omega R_S}}$. This equation exhibits a key finding of our study, namely, that the equivalent capacitance at high frequency displays a dependence on the semiconductor channel resistance. The predicted coupling between the channel resistance and the gate-to-channel capacitance at the heterojunction interface highlights a unique property of EDLTs. However, because of the relatively large channel conductance and small capacitance, this transmission-line effect is not significant for conventional FETs unless they are probed at very high frequency.[168] Further discussion of this equivalent circuit is presented in Appendix D.

5.3 Results and discussion

To verify the theoretical arguments, organic EDLTs based on rubrene crystals and ionic liquids (ILs) were fabricated and characterized by following previously established procedures.[169] The source, drain and gate contacts were made from Au. The ionic liquid employed in this study was [1-butyl-1-methyl pyrrolidinium][tris(pentafluoroethyl) trifluorophosphate], or [P14][FAP], which was selected to ensure a high carrier mobility (~ 3 $cm^2V^{-1}s^{-1}$) and stable device operation for a wide range of gate bias and

temperature.[157] Variable temperature admittance measurements and transistor measurements were then carried out.[57,169] The hole accumulation in the rubrene

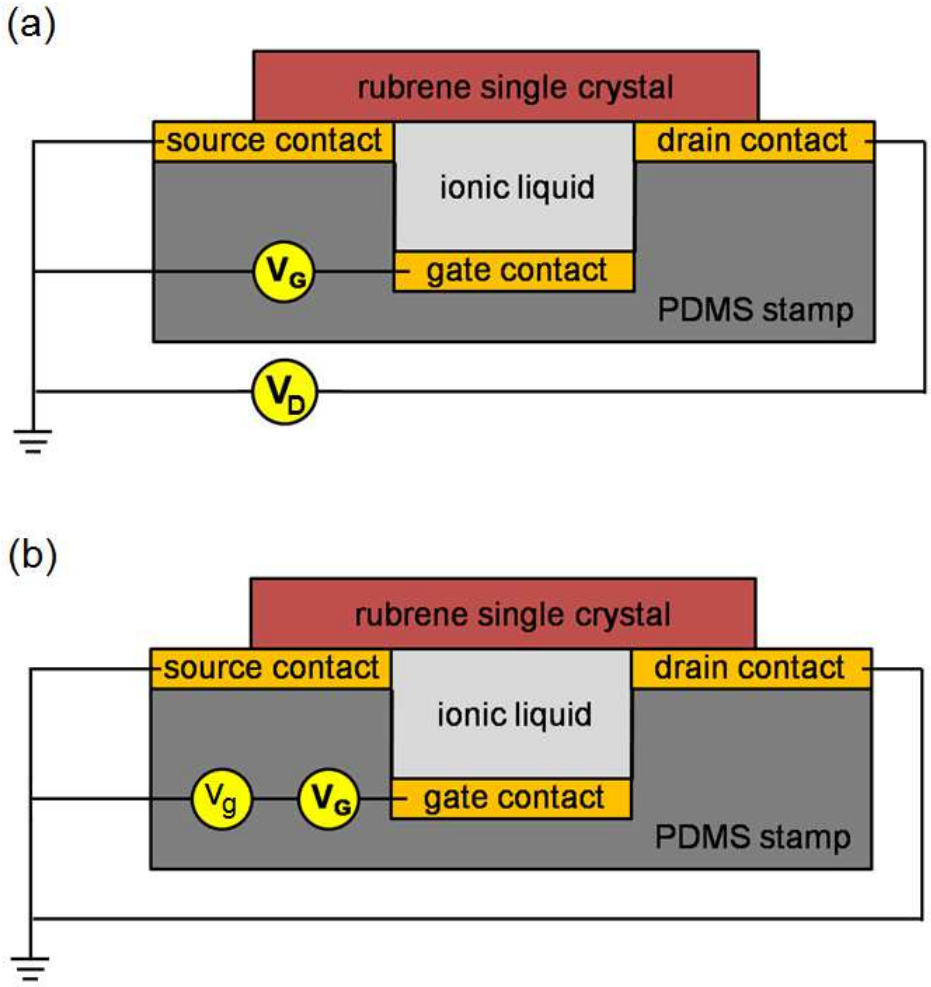

FIG. 5.3. Schematics of experimental device configuration for transistor measurement (a) and for admittance measurement (b). V_G and V_D are DC voltage biases. v_g is an AC signal.

conduction channel can reach up to (6 ~7) × 10^{13} cm^{-2} before device failure, as identified by gate displacement current measurements.[157,170,171] Measurement configurations are

shown in FIG. 5.3. In the transistor measurement (FIG. 5.3 (a)), the channel sheet conductance, σ_S (= R_S^{-1}), was measured as a function of gate voltage, V_G, with a four-terminal structure.[144] For the admittance measurement, both source and drain contacts were grounded, effectively resulting in a gate-IL-channel structure, and the gate-to-channel total admittance Y and phase angle θ were measured as a function of V_G and frequency f. (The small signal modulation amplitude was 100 mV.) An equivalent gate-to-channel capacitance C_{eq} was extracted from the imaginary part of Y (C_{eq} = Im(Y)/ω).

The frequency-dependent admittance measurement was first performed on a rubrene EDLT with the DC voltage bias V_G set to zero. The transfer curve at 300 K (not shown) of this device indicated that the channel was fully "on" when V_G = 0 V (threshold voltage V_T ~ 1.0 V), with a sheet resistance of ~ 130 kΩ. The admittance results are shown in FIG. 5.4 for both 250 K (red circles) and 300 K (black diamonds). FIG. 5.4 (a) and (b) show the real part, Re(Y), and the imaginary part, Im(Y), respectively. FIG. 5.4 (c) shows the equivalent gate-to-channel capacitance C_{eq}. FIG. 5.4 (d) shows the phase angle of Y. The EDLT measured has a channel length of 300 μm, a channel width of 340 μm, and the distance between the gate and rubrene (*i.e.*, the thickness of ionic liquid layer) is 5 μm. The corresponding solid lines are calculated results from the equivalent circuit shown in FIG. 5.2 with the following parameters: gate/electrolyte capacitance C_{ME} = 1.1 × 10^{-5} F/cm^2, electrolyte/semiconductor capacitance C_{ES} = 1.7 × 10^{-6} F/cm^2, and rubrene channel resistance R_S = 1.3 × 10^5 Ω. The ionic liquid resistance R_E decreases with increasing temperature.[172] The values used in the calculation are: R_E (250 K) = 6.7 × 10^4 Ω and R_E (300 K) = 7.5 × 10^3 Ω.

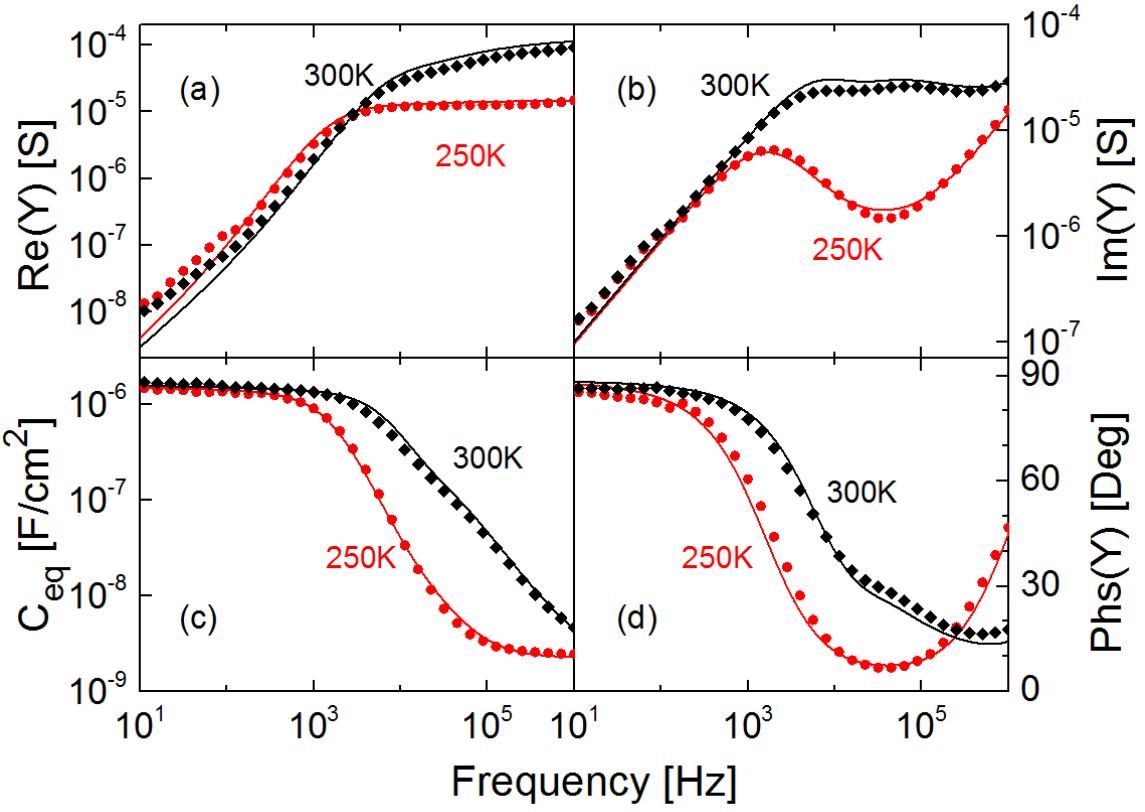

FIG. 5.4. Gate-to-channel admittance of EDLTs at 250 K (red) and 300 K (black) as a function of frequency. The dots are experimental results from a rubrene/[P14][FAP]/Au device ($V_G = 0$). The lines are calculation results from the model shown in FIG. 5.2. (a) Real part of admittance. (b) Imaginary part of admittance. (c) Equivalent gate-to-channel capacitance $C_{eq} = \mathrm{Im}(Y)/\omega$. (d) Phase of admittance. Experimental data are courtesy of Dr. Wei Xie et al. at University of Minnesota.

The calculated results agree well with the experiments. Looking at the capacitance-frequency plots in FIG. 5.4 (c), at low frequency ($\leq 10^2$ Hz), the equivalent

capacitance C_{eq} reaches a maximum, the value of which is consistent with the electrolyte/semiconductor interfacial capacitance C_{ES}. This is attributed to the ions having enough time to move and reach a steady state forming two double-layer charges at the gate/electrolyte and electrolyte/semiconductor interfaces. The former is usually larger due to the small Thomas-Fermi screening length in Au.[173,174] Therefore, the equivalent capacitance $C_{eq} = (C_{ES} C_{ME})/(C_{ES} + C_{ME}) \approx C_{ES}$. At high frequency (~ 10^6 Hz), C_{eq} reaches a minimum, the value of which is approaching the geometric capacitance, C_{geo}. In this case, the ion motion does not follow the rapidly changing field, and the IL behaves essentially like a conventional dielectric. The strong frequency dependence of the capacitance in rubrene EDLTs is in qualitative accordance with the behavior of a metal-IL-metal structure.[157,175] For the phase angle plot in FIG. 5.4 (d), a 90° phase means the system is capacitive and a 0° phase means that it is resistive. At low frequency ($\leq 10^2$ Hz), the double-layer interfacial capacitance is the dominant element and the system is largely capacitive (~ 86°). As the frequency increases, the electrolyte conductivity starts to play a role but the effect of the geometric capacitance is still negligible, therefore the system becomes resistive resulting in a decreasing phase angle approaching 0°. When the frequency is very high (~ 10^6 Hz), eventually the geometric capacitance becomes dominant and the phase increases again, as clearly seen in the curve at 250 K. Additionally, a gentle change in slope is observed in the phase plot (see the 10^4 Hz ~ 10^6 Hz region in the 300 K plot). This is controlled by the ratio of the semiconductor to electrolyte resistance, R_S / R_E. R_E decreases significantly with

temperature while R_S does not. At 250 K, R_S / R_E is relatively small and the phase plot is smooth. At 300 K, the decrease of R_E leads to a more prominent effect of R_S. As the

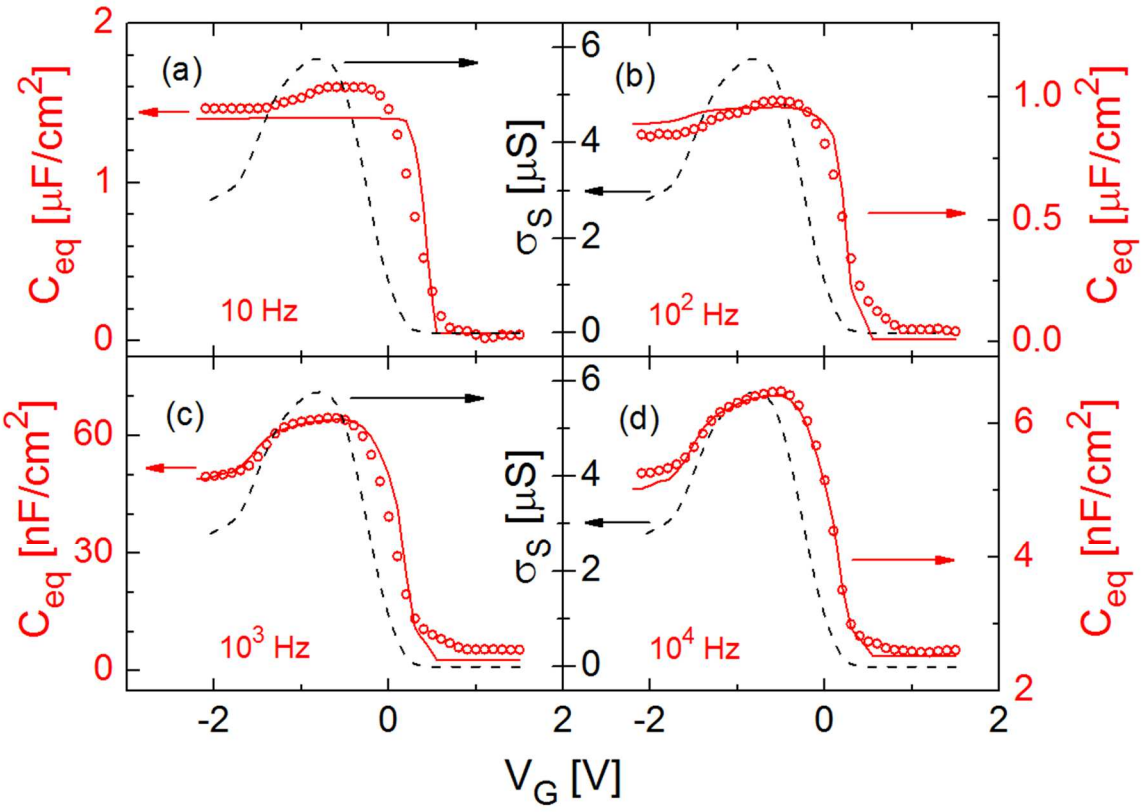

FIG. 5.5. Equivalent gate-to-channel capacitance-voltage characteristics of EDLTs at 235 K at different frequencies. The dashed lines are channel conductance as a function of the gate voltage (the same for the four subplots). The open circles are experimental results from a rubrene/[P14][FAP]/Au device. The solid lines are corresponding calculation results from the model shown in FIG. 5.2. Experimental data are courtesy of Dr. Wei Xie et al. at University of Minnesota.

overall resistive component in the circuit decreases, the phase angle increases and its frequency dependence becomes non-smooth. The satisfactory agreement between the

calculated and experimental results over these subtle changes validates the proposed equivalent circuit model.

Next, V_G-dependent admittance measurements were performed for different frequencies, together with transistor measurements on a different rubrene EDLT ($V_T \sim 0.3$ V). The measured equivalent capacitance as a function of V_G is shown in FIG. 5.5 (open circles) at frequencies from 10 Hz to 10^4 Hz. The temperature is 235 K. The red solid lines are corresponding calculations from the equivalent circuit model using the same C_{ES} and C_{ME} parameters as shown above. The ionic liquid resistance R_E (235 K) is set to 5×10^5 Ω in the calculation. The rubrene channel conductance σ_S is V_G-dependent and approximately frequency-independent. (For the frequency range discussed here, the equivalent circuit model using a frequency-independent R_S is sufficient to obtain good agreement with the experiments.[176]) The measured σ_S as a function of the gate voltage is plotted as the black dashed lines in FIG. 5.5, and is used in the calculation (for the parameter R_S). It can be seen that the channel conductance in rubrene EDLTs exhibits a pronounced peak as a function of V_G. This unusual behavior has been extensively discussed in previous work and is beyond the scope of this chapter.[177] Nevertheless, the non-monotonic σ_S-V_G relationship happens to provide an excellent example to demonstrate the internal correlation between conductance and capacitance in EDLTs.

The model calculation agrees well with the experimental results. When the device is turned on ($V_G \leq 0.3$ V), we observe that the equivalent gate-to-channel capacitance decreases with increasing operating frequency, consistent with results in FIG. 5.4 (c). The important observation is that at low frequency (*e.g.*, 10 Hz), the measured

capacitance is independent of the gate voltage and its maximum value (~ 1.5 μF/cm^2) agrees with the double-layer interfacial capacitance C_{ES}. As the frequency increases, the capacitance shows non-monotonic V_G dependence and starts to exhibit a peak. At $f = 10^4$ Hz the capacitance-voltage characteristics reflect the conductance-voltage characteristics satisfactorily. The results agree with the prediction of equation (5.1). At low frequency, the equivalent capacitance reduces to the double-layer capacitance, which is independent with the gate voltage. At high frequency, the equivalent capacitance is coupled to the voltage-dependent channel conductance. The capacitance-voltage curve is broader than the conductance-voltage curve because the channel conductance term is under the square root.

The next question is whether one can find a characteristic frequency, f_C, for the transition between the two distinct C_{eq} vs. V_G relationships. Physically, the measurement of the equivalent capacitance can be viewed as a charging/discharging process. If the holes in the rubrene channel have enough time to reach a steady state distribution corresponding to the voltage applied ($f < f_C$), the measured capacitance result should be equal to the double-layer interfacial capacitance, and the charging process is complete. If the holes in the rubrene channel do not have enough time to charge the ion liquid/ rubrene interface ($f > f_C$), the charging process is incomplete. The charge level reached in the process is proportional to the rubrene conductance, and it is expected that the capacitance follows a voltage dependence similar to that of the conductance. A rough estimate of f_C may be obtained from the RC constant τ defined by the rubrene resistance, R_S/12 (see discussions for equation (5.1)), multiplied by the electrolyte/semiconductor capacitance

C_{ES}. For this device, $f_C = (2\pi\tau)^{-1} \approx 4 \times 10^3$ Hz. This agrees with the results of FIG. 5.5. For organic EDLTs f_C is low due to the large interfacial capacitance and the relatively small channel conductance. On the other hand, since the model does not involve any specific properties of the semiconductor, it can be readily extended to EDLTs based on inorganic semiconductors. In this case, (*e.g.*, ZnO channel[165]) we expect the characteristic frequency to be greater (~ 10^5 Hz) due to the smaller channel resistance. The frequency window needs to be chosen carefully to observe this coupling effect. (Appendix E)

5.4 Conclusion

We have theoretically investigated the unique coupling of channel conductance and gate-to-channel capacitance in EDLTs and compared the results to experimental data. We anticipate this coupling to be an inherent property of these devices. Gate voltage dependent DC and AC measurements in rubrene EDLTs confirm the model-predicted correlation of conductance and capacitance. Our work is important for understanding the device physics of EDLTs, an intriguing class of FETs that will continue to facilitate fundamental transport studies at high charge densities and that has potential for low-voltage printable electronics.

Chapter 6 Summary and suggestions for future work

6.1 Summary

We have presented models and calculations for heterostructure OLEDs, OPCs, and OFETs. Generally, the interface of a heterostructure is critical for various types of devices. Fascinating physics may occur because of the special environment between two different materials. In OLEDs the offset of HOMO and LUMO levels leads to charge accumulation at the interface, increasing the probability of exciplex formation. From a spintronic point of view, the exciplexes and their precursor polaron pairs establish a link between two spin 1/2 particles. In OPCs the energy offset facilitates the charge-transfer state exciton dissociation. When a thin tunnel barrier is inserted at the interface, certain microscopic processes are enhanced or suppressed. For OFETs, the introduction of an ionic liquid makes its interface with the organic semiconductor interesting. The coupling between the channel conductance and the gate-to-channel capacitance revealed in chapter 5 is only part of the story. This particular interface also leads to an unexpected two-channel conduction mechanism.[59] A problem that still exists today is how to probe the (quasi-) two-dimentional interfacial properties. In this dissertation, some assumptions regarding interfacial parameters are made. They are consistent with macroscopic device observations, but their validity still remains unknown without direct measurements. Also we have assumed that the interface is a flat surface throughout this dissertation. In

practice, the morphology and non-uniformity may be critical for device performance.[117,178,179]

In additional to the work presented in the previous chapters, I have been also working on several other topics during my Ph.D. period, such as electrostatic capacitance in single and double layer organic diodes, two-channel conduction model in ionic-liquid-gated organic transistors based on percolation theory, and spin scattering in graphene. More details can be found in relevant papers.[58-64]

6.2 Suggestions for future work

At the end of this dissertation, we give a few suggestions for possible future work.

One topic that still requires much theoretical work is the bulk heterojunction modeling.[180,181] The structure of a bulk heterojunction has been widely applied to organic photovoltaic cells. It improves the device efficiency because of a dramatic increase in the interfacial area between donor and acceptor materials. However, the current state of theoretical modeling remains largely empirical due to the complexity of the structure. In order to model the device properly at least a two-dimensional model is required. For example, a local interface that is perpendicular to the current flow shows a significantly different behavior for carrier recombination compared to a local interface parallel to the current flow.[182] There are additional issues to be considered such as the degree of material mixing and percolation properties.

Based on the idea in chapter 3, experimental results have shown that "spacer layers" of different materials can be inserted between donor and acceptor materials showing an improvement in device efficiency.[54] A rough explanation has been given using the model developed in this thesis. However, there are still limitations requiring future work. The spacer layer is not always an insulating material as shown in chapter 3. In some experiments, the spacer layer is also an organic material with conductivity comparable to the donor and acceptor materials. Also the thickness of the spacer layer is sometimes comparable to the donor and acceptor layers, making the bilayer model less convincing.

Bibliography

[1] C. K. Chiang, C. R. Fincher, Jr., Y. W. Park, and A. J. Heeger, Phys. Rev. Lett. **39**, 1098 (1977).

[2] T. W. Kelley, P. F. Baude, C. Gerlach, D. E. Ender, D. Muyres, M. A. Haase, D. E. Vogel, and S. D. Theiss, Chem. Mater. **16**, 4413 (2004).

[3] J. M. Shaw and P. F. Seidler, IBM J. Res. & Dev. **45**, 3 (2001).

[4] S. R. Forrest and M. E. Thompson, Chem. Rev. **107**, 923 (2007).

[5] W. Brütting, *Physics of organic semiconductors* (Wiley-VCH, Weinheim, Germany, 2005).

[6] C. W. Tang and S. A. van Slyke, Appl. Phys. Lett. **51**, 913 (1987).

[7] J. H. Burroughes, D. D. C. Bradley, A. R. Brown, R. N. Marks, K. Mackay, R. H. Friend, P. L. Burns, and A. B. Holmes, Nature (London) **347**, 539 (1990).

[8] D. Braun and A. J. Heeger, Appl. Phys. Lett. **58**, 1982 (1991).

[9] A. C. Mayer, S. R. Scully, B. E. Hardin, M. W. Rowell, and M. D. McGehee, Mater. Today **10**, 28 (2007).

[10] S. Günes, H. Neugebauer, and N. S. Sariciftci, Chem. Rev. **107**, 1324 (2007).

[11] G. Dennler, M. C. Scharber, and C. J. Brabec, Adv. Mater. **21**, 1323 (2009).

[12] G. Horowitz, Adv. Mater. **10**, 365 (1998).

[13] Z. Bao and J. Locklin, *Organic field-effect transistors* (CRC Press, Boca Raton, Florida, 2007).

[14] H. Sirringhaus, Adv. Mater. **26**, 1319 (2014).

[15] Q. Meng and W. Hu, Phys. Chem. Chem. Phys. **14**, 14152 (2012).

[16] Z. B. Henson, K. Müllen, and G. C. Bazan, Nature Chem. **4**, 699 (2012).

[17] A. Mishra and P.Bäuerle, Angew. Chem. Int. Ed. **51**, 2020 (2012).

[18] L. Duan, L. Hou, T-W Lee, J. Qiao, D. Zhang, G. Dong, L. Wang, and Y. Qiu, J. Mater. Chem. **20**, 6392 (2010).

[19] V. A. Montes, R. Pohl, J. Shinar, and P. Anzenbacher Jr. Chem. Eur. J. **12**, 4523 (2006).

[20] B. C. Thompson and J. M. J. Fréchet, Angew. Chem. Int. Ed. **47**, 58 (2008).

[21] J. Nelson, Mater. Today **14**, 462 (2011).

[22] V. Podzorov, V. M. Pudalov, and M. E. Gershenson, Appl. Phys. Lett. **82**, 1739 (2003).

[23] F. Yakuphanoglu, J. Phys. Chem. Solids **69**, 949 (2008).

[24] V. Coropceanu, J. Cornil, D. A. da S. Filho, Y. Olivier, R. Silbey, and J.-L. Brédas, Chem. Rev. **107**, 926 (2007).

[25] Z. Shuai, H. Geng, W. Xu, Y. Liao, and J.-M. André, Chem. Soc. Rev. **43**, 2662 (2014).

[26] R. A. Marcus, J. Chem. Phys. **24**, 966 (1956).

[27] R. A. Marcus, J. Chem. Phys. **26**, 867 (1957).

[28] R. A. Marcus, J. Chem. Phys. **26**, 872 (1957).

[29] M. C. J. M. Vissenberg and M. Matters, Phys. Rev. B **57**, 964 (1998).

[30] J. Locklin, M. E. Roberts, S. C. B. Mannsfeld, and Z. Bao, J. Macromolecular Science, Part C: Polymer Rev. **46**, 79 (2006).

[31] J. J. M. van der Holst, F. W. A. van Oost, R. Coehoorn, and P. A. Bobbert, Phys. Rev. B **80**, 235202 (2009).

[32] A. Pivrikas, G. Juška, R. Österbacka, M. Westerling, M. Viliūnas, K. Arlauskas, and H. Stubb, Phys. Rev. B **71**, 125205 (2005).

[33] M. Lenes and H. J. Bolink, ACS Appl. Mater. Interfaces **2**, 3664 (2010).

[34] T. R. Hebner, C. C. Wu, D. Marcy, M. H. Lu, and J. C. Sturm, Appl. Phys. Lett. **72**, 519 (1998).

[35] S. Chang, J. Liu, J. Bharathan, Y. Yang, J. Onohara, and J. Kido, Adv. Mater. **11**, 734 (1999).

[36] M.J.Thompson, Solid State Tech. **47**, 30 (2004).

[37] S. Tokito, H. Tanaka, K. Noda, A. Okada, and Y. Taga, Appl. Phys. Lett. **70**, 1929 (1997).

[38] F. Wang, X. Qiao, T. Xiong, and D. Ma, Organic Electron. **9**, 985 (2008).

[39] B. Paci, A. Generosi, V. R. Albertini, G. D. Spyropoulos, E. Stratakis, and E. Kymakis, Nanoscale **4**, 7452 (2012).

[40] C. Boehme and J. M. Lupton, Nature Nanotech. **8**, 612 (2013).

[41] D. Sun, E. Ehrenfreund, and Z. V. Vardeny, Chem. Commun. **50**, 1781 (2014).

[42] V. N. Prigodin, J. W. Yoo, H. W. Jang, C. Kao, C. B. Eom, and A. J. Epstein, J. Phys.: Conference Series **292**, 012001 (2011).

[43] M. Yunus, P. P. Ruden, and D. L. Smith, J. Appl. Phys. **103**, 103714 (2008).

[44] M. Yunus, P. P. Ruden, and D. L. Smith, Appl. Phys. Lett. **93**, 123312 (2008).

[45] M. Yunus, P. P. Ruden, and D. L. Smith, Synth. Met. **160**, 204 (2009).

[46] D. L. Smith and P. P. Ruden, Phys. Rev. B **78**, 125202 (2008).

[47] M. Yunus, P. P. Ruden, and D. L. Smith, Appl. Phys. Lett. **97**, 223304 (2010).

[48] F. Liu, P. P. Ruden, I. H. Campbell, and D. L. Smith, Appl. Phys. Lett. **99**, 123301 (2011).

[49] F. Liu, P. P. Ruden, I. H. Campbell, and D. L. Smith, J. Appl. Phys. **111**, 094507 (2012).

[50] F. Liu, P. P. Ruden, I. H. Campbell, and D. L. Smith, Mater. Res. Soc. Symp. Proc. **1448**, (2012) DOI: 10.1557/opl.2012.1492.

[51] F. Liu, B. K. Crone, P. P. Ruden, and D. L. Smith, J. Appl. Phys. **113**, 044516 (2013).

[52] F. Liu, B. K. Crone, P. P. Ruden, and D. L. Smith, Mater. Res. Soc. Symp. Proc. **1537**, (2013) DOI: 10.1557/opl.2013.911.

[53] A. Mohite, W. Nie, G. Gupta, B. Crone, C. Kuo, H. Tsai, D. Smith, P. Ruden, F. Liu, H. Wang, and S. Tretiak, Bulletin of the American Physical Society **59**, (2014) http://meetings.aps.org/link/BAPS.2014.MAR.B22.9.

[54] W. Nie, G. Gupta, B. K. Crone, F. Liu, D. L. Smith, P. P. Ruden, C.-Yu Kuo, H. Tsai, H.-L. Wang, H. Li, S. Tretiak, and A. D. Mohite, Advanced Science, . DOI: 10.1002/advs.201500024.

[55] F. Liu, M. R. Kelley, S. A. Crooker, W. Nie, A. D. Mohite, P. P. Ruden, and D. L. Smith, Phys. Rev. B **90**, 235314 (2014).

[56] S. A. Crooker, F. Liu, M. R. Kelley, N. J. D. Martinez, W. Nie, A. Mohite, I. H. Nayyar, S. Treitak, D. L. Smith, and P. P. Ruden, Appl. Phys. Lett. **105**, 153304 (2014).

[57] F. Liu, W. Xie, S. Shi, C. D. Frisbie, and P. P. Ruden, Appl. Phys. Lett. **103**, 193304 (2013).

[58] F. Liu, P. P. Ruden, I. H. Campbell, and D. L. Smith, Appl. Phys. Lett. **101**, 023501 (2012).

[59] W. Xie, F. Liu, S. Shi, P. P. Ruden, and C. D. Frisbie, Adv. Mater. **26**, 2527 (2014).

[60] F. Liu, Y. Liu, J. Hu, D. L. Smith, and P. P. Ruden, J. Appl. Phys. **114**, 093708 (2013).

[61] A. Goswami, Y. Liu, F. Liu, P. P. Ruden, and D. L. Smith, Mater. Res. Soc. Symp. Proc. **1505**, (2013) DOI: 10.1557/opl.2013.246.

[62] F. Liu, Y. Liu, D. L. Smith, and P. P. Ruden, in preparation for IEEE Trans. Electron Devices.

[63] S. Shi, F. Liu, D. L. Smith, and P. P. Ruden, J. Appl. Phys. **117**, 085501 (2015).

[64] Y. Liu, A. Goswami, F. Liu, D. L. Smith, and P. P. Ruden, J. Appl. Phy. **116**, 234301 (2014).

[65] A. Dodabalapur, Solid State Commun. **102**, 259 (1997).

[66] J. Kido, M. Kimura, and K. Nagai, Science, **267**, 1332 (1995).

[67] C. W. Tang, Appl. Phys. Lett. **48**, 183 (1986).

[68] S. H. Park, A. Roy, S. Beaupré, S. Cho, N. Coates, J. S. Moon, D. Moses, M. Leclerc, K. Lee, and A. J. Heeger, Nature Photonics, **3**, 297 (2009).

[69] M. Pope and C. Swenberg, *Electronic Process in Organic Crystals and Polymers*, 2nd ed. (Oxford University Press, New York, 1999).

[70] V. N. Abakumov, V. I. Perel, and I. N. Yassievich, *Nonradiative Recombination in Semiconductors* (North-Holland, Amsterdam, 1991).

[71] R. A. Street and M. Schoendorf, Phys. Rev. B **81**, 205307 (2010).

[72] D. D. Gebler, Y. Z. Wang, J. W. Blatchford, S. W. Jessen, D. K. Fu, T. M. Swager, A. G. MacDiarmid, and A. J. Epstein, Appl. Phys. Lett. **70**, 1644 (1997).

[73] S. A. Jenekhe and J. A. Osaheni, Science **265**, 765 (1994).

[74] J. A. Osaheni and S. A. Jenekhe, Macromolecules **27**, 739 (1994).

[75] L. Onsager, Phys. Rev. **54**, 554 (1938).

[76] C. L. Braun, J. Chem. Phys. **80**, 4157 (1984).

[77] S. L. Lai, M. Y. Chan, Q. X. Tong, M. K. Fung, P. F. Wang, C. S. Lee, and S. T. Lee, Appl. Phys. Lett. **93**, 143301 (2008).

[78] D. Wang, W. Li, B. Chu, Z. Su, D. Bi, D. Zhang, J. Zhu, F. Yan, Y. Chen, and T. Tsuboi, Appl. Phys. Lett. **92**, 053304 (2008).

[79] P. Peumans, S. Uchida, and S. R. Forrest, Nature, **425**, 158 (2003).

[80] J. G. Müller, J. M. Lupton, J. Feldmann, U. Lemmer, M. C. Scharber, N. S. Sariciftci, C. J. Brabec, and U. Scherf, Phys. Rev. B, **72**, 195208 (2005).

[81] S. K. Pal, T. Kesti, M. Maiti, F. Zhang, O. Inganäs, S. Hellström, M. R. Andersson, F. Oswald, F. Langa, T. Österman, T. Pascher, A. Yartsev, and V. Sudström, J. Am. Cem. Soc., **132**, 12440 (2010).

[82] P. S. Davids, I. H. Campbell, and D. L. Smith, J. Appl. Phys. **82**, 6319 (1997).

[83] B. K. Crone, P. S. Davids, I. H. Campbell, and D. L. Smith, J. Appl. Phys. **87**, 1974 (2000).

[84] J. Frekel, Phys. Rev. **54**, 647 (1938).

[85] D. L. Scharfetter and H. K. Gummel, IEEE Trans. Electron Device **ED-16**, 64 (1969).

[86] C. Chu, Y. Shao, V. Shrotriya, and Y. Yang, Appl. Phys. Lett. **86**, 243506 (2005).

[87] P. Peumans, A. Yakimov, and S. R. Forrest, J. Appl. Phys. **93**, 3693 (2003).

[88] T. Takahashi, S. Suzuki, T. Morikawa, H. Katayama-Yoshida, S. Hasegawa, H. Inokuchi, K. Seki, K.Kikuchi, S. Suzuki, K. Ikemoto, and Y. Achiba, Phys. Rev. Lett. **68**, 1232 (1992).

[89] E. L. Shirley, L. X. Benedict and S. G. Louie, Phys. Rev. B **54**, 10970 (1996).

[90] S. S. Harilal, C. V. Bindhu, V. P. N. Nampoori, and C. P. G. Vallabhan, J. Appl. Phys. **86**, 1388 (1999).

[91] J. W. Arbogast, A. P. Darmanyan, C. S. Foote, Y. Rubin, F. N. Diederich, M. M. Alvarez, S. J. Anz, and R. L. Whetten, J. Phys. Chem. **95**, 11 (1991).

[92] L. A. A. Pettersson, L. S. Roman, and O. Inganäs, J. Appl. Phys. **86**, 487 (1999).

[93] D. Qin, P. Gu, R. S. Dhar, S. G. Razavipour, and D. Ban, Phys. Status Solidi (a) **208**, 1967 (2011).

[94] N. Geacintov, M. Pope, and F. Vogel, Phys. Rev. Lett. **22**, 593 (1969).

[95] Y. Tomkiewicz, R. P. Groff, and P. Avakian, J. Chem. Phys. **54**, 4504 (1971).

[96] V. K. Thorsmølle, R. D. Averitt, J. Demsar, D. L. Smith, S. Tretiak, R. L. Martin, X. Chi, B. K. Crone, A. P. Ramirez, and A. J. Taylor, Phys. Rev. Lett. **102**, 017401 (2009).

[97] W. Hofberger and H. Bässler, Phys. Stat. Sol. (b) **69**, 725 (1975).

[98] G. Vaubel and H. Bässler, Mole. Crys. Liq. Crys. **12**, 47 (1970).

[99] R. P. Groff, P. Avakian, and R. E. Merrifield, Phys. Rev. B **1**, 815 (1970).

[100] M. A. Baldo and S. R. Forrest, Phys. Rev. B **64**, 085201 (2001).

[101] H. Hoppe and N. S. Sariciftci, J. Mater. Res. **19**, 1924 (2004).

[102] J.-M. Nunzi, C. R. Physique **3**, 523 (2002).

[103] S. R. Forrest, MRS Bulletin **30**, 28 (2005).

[104] T. Zhuang, Z. Su, Y. Liu, B. Chu, W. Li, J. Wang, F. Jin, X. Yan, B. Zhao, F. Zhang, and D. Fan, Appl. Phys. Lett. **100**, 243902 (2012).

[105] W. Chen, H. Xiang, Z. Xu, B. Yan, V. A. L. Roy, and C. Che, Appl. Phys. Lett. **91**, 191109 (2007).

[106] I. H. Campbell and B. K. Crone, Appl. Phys. Lett. **101**, 023301 (2012).

[107] D. Veldman, Ö. İpek, S. C. Meskers, J. Sweelssen, M. M. Koetse, S. C. Veenstra, J. M. Kroon, S. S. van Bavel, J. Loos, and R. A. J. Janssen, J. Am. Chem. Soc. **130**, 7721 (2008).

[108] A. Wappelt, A. Bergmann, A. Napiwotzki, H. J. Eichler, H. J. Jüpner, A. Kummrow, A. Lau, and S. Woggon, J. Appl. Phys. **78**, 5192 (1995).

[109] C. J. Brabec, N. S. Sariciftci, and J. C. Hummelen, Adv. Funct. Mater. **11**, 15 (2001).

[110] N. C. Giebink, B. E. Lassiter, G. P. Wiederrecht, M. R. Wasielewski, and S. R. Forrest, Phys. Rev. B **82**, 155306 (2010).

[111] A. Matsui, J. Opt. Soc. Am. B **7**, 1615 (1990).

[112] E. A. Silinsh and V. Capek, *Organic Molecular Crystals* (American Institute of Physics, New York, 1994).

[113] D. A. Hutchinson, Acta. Cryst. **15**, 949 (1962).

[114] M. S. Dresselhaus, G. Dresselhaus, and P. C. Eklund, *Science of Fullerenes and Carbon Nanotubes* (Academic Press, 1996).

[115] B. Ray and M. A. Alam, IEEE J. Photovoltaics **3**, 310 (2013).

[116] M. A. Green, K. Emery, Y. Hishikawa, W. Warta, and E. D. Dunlop, Prog. Photovolt: Res. Appl. **20**, 12 (2012).

[117] J. D. Zimmerman, X. Xiao, C. K. Renshaw, S. Wang, V. V. Diev, M. E. Thompson, and S. R. Forrest, Nano Lett. **12**, 4366 (2012).

[118] P. Maniadis, T. Lookman, A. Saxena, and D. L. Smith, Phys. Rev. Lett. **108**, 257802 (2012).

[119] Z. V. Vardeny, *Organic Spintronics* (CRC Press, Boca Raton, FL, USA, 2010).

[120] Z. V. Vardeny, Nat. Mater. **8**, 91 (2009).

[121] B. Koopmans, Nat. Phys. **10**, 249 (2014).

[122] V. A. Dediu, L. E. Hueso, I. Bergenti, and C. Taliani, Nat. Mater. **8**, 707 (2009).

[123] J. Kalinowski, M. Cocchi, D. Virgili, P. D. Marco, and V. Fattori, Chem. Phys. Lett. **380**, 710 (2003).

[124] T. L. Francis, Ö. Mermer, G. Veeraraghavan, and M. Wohlgenannt, New J. Phys. **6**, 185 (2004).

[125] V. N. Prigodin, J. D. Bergeson, D. M. Lincoln, and A. J. Epstein, Synth. Met. **156**, 757 (2006).

[126] P. Desai, P. Shakya, T. Kreouzis, and W. P. Gillin, Phys. Rev. B **76**, 235202 (2007).

[127] B. Hu and Y. Wu, Nat. Mater. **6**, 985 (2007).

[128] Y. Iwasaki, T. Osasa, M. Asahi, and M. Matsumura, Phys. Rev. B **74**, 195209 (2006).

[129] Y. Wu, Z. Xu, and B. Hu, Phys. Rev. B **75**, 035214 (2007).

[130] J. D. Bergeson, V. N. Prigodin, D. M. Lincoln, and A. J. Epstein, Phys. Rev. Lett. **100**, 067201 (2008).

[131] T. D. Nguyen, G. H.-Markosian, F. Wang, L. Wojcik, X.-G. Li, E. Ehrenfreund, and Z. V. Vardeny, Nat. Mater. **9**, 345 (2010).

[132] D. V. Dodin, A. I. Ivanov, and A. I. Burshtein, J. Chem. Phys. **138**, 124102 (2013).

[133] S. P. Kersten, A. J. Schellekens, B. Koopmans, and P. A. Bobbert, Phys. Rev. Lett. **106**, 197402 (2011).

[134] E. Ehrenfreund and Z. V. Vardeny, Isr. J. Chem. **52**, 552 (2012).

[135] J. Rybicki, T. D. Nguyen, Y. Sheng, M. Wolgenannt, Synth. Met. **160**, 280 (2010).

[136] J. Rybicki and M. Wohlgenannt, Phys. Rev. B **79**, 153202 (2009).

[137] N. J. Harmon and M. E. Flatté, Phys. Rev. B **85**, 075204 (2011).

[138] A. J. Schellekens, W. Wagemans, S. P. Kersten, P. A. Bobbert, and B. Koopmans, Phys. Rev. B **84**, 075204 (2011).

[139] I. A. Merkulov, Al. L. Efros, and M. Rosen, Phys. Rev. B **65**, 205309 (2002).

[140] H. Haashi, *Introdution to Dynamic Spin Chemistry: Magnetic Field Effects upon Chemical and Biochemical Reactions* (World Scientific Publishing, Singapore, 2004).

[141] R. Kubo, J. Math. Phys. **4**,174 (1963).

[142] C. P. Slichter, *Principles of Magnetic Resonance* 3rd Ed. (Springer, UIUC, IL, USA, 1990).

[143] A. G. Redfield, IBM J. Research Develop. **1**, 19 (1957).

[144] R. K. Wangsness and F. Bloch, Phys. Rev. **89**, 728 (1953).

[145] F. Bloch, Phys. Rev. **102**, 104 (1956).

[146] E. Paladino, Y. M. Galperin, G. Falci, and B. L. Altshuler, Rev. Mod. Phys. **86**, 361 (2014).

[147] P. Dutta and P. M. Horn, Rev. Mod. Phys. 53, 497 (1981).

[148] F. N. Hooge and P. A. Bobbert, Physica B 239, 223 (1997).

[149] K. Goushi, K. Yoshida, K. Sato, and C. Adachi, Nat. Photon. 6, 253 (2012).

[150] E. J. Shisick and H. M. McConnell, Biochem. Biophys. Res. Comm. **46**, 321 (1972).

[151] B. Brocklehurst, J. Chem. Soc., Faraday Trans. **2**, 1869 (1976).

[152] T. D. Nguyen, T. P. Basel, Y.-J. Pu, X-G. Li, E. Ehrenfreund, and Z. V. Vardeny, Phys. Rev. B **85**, 245437 (2012).

[153] G. Ni, T. D. Nguyen, and Z. V. Vardeny, Appl. Phys. Lett. **98**, 263302 (2011).

[154] P. Chen, Q. Peng, L. Yao, N. Gao, and F. Li, Appl. Phys. Lett. **102**, 063301 (2013).

[155] S. H. Kim, K. Hong, W. Xie, K. H. Lee, S. Zhang, T. P. Lodge, and C. D. Frisbie, Adv. Mater. **25**, 1822 (2013).

[156] T. Fujimoto and K. Awaga, Phys. Chem. Chem. Phys. **15**, 8983 (2013).

[157] W. Xie and C. D. Frisbie, J. Phys. Chem. C **115**, 14360 (2011).

[158] W. Xie and C. D. Frisbie, MRS Bulletin **38**, 43 (2013).

[159] K. Ueno, S. Nakamura, H. Shimotani, A. Ohtomo, N. Kimura, T. Nojima, H. Aoki, Y. Iwasa, and M. Kawasaki, Nat. Mater. **7**, 855 (2008).

[160] Y. Yamada, K. Ueno, T. Fukumura, H. T. Yuan, H. Shimotani, Y. Iwasa, L. Gu, S. Tsukimoto, Y. Ikuhara, and M. Kawasaki, Science **332**, 1065 (2011).

[161] J. Ye, M. F. Craciun, M. Koshino, S. Russo, S. Inoue, H. Yuan, H. Shimotani, A. F. Morpurgo, and Y. Iwasa, Proc. Natl. Acad. Sci. **108**, 13002 (2011).

[162] J. H. Cho, J. Lee, Y. Xia, B. Kim, Y. He, M. J. Renn, T. P. Lodge, and C. D. Frisbie, Nat. Mater. **7**, 900 (2008).

[163] M. Ha, Y. Xia, A. A. Green, W. Zhang, M. J. Renn, C. H. Kim, M. C. Hersam, and C. D. Frisbie, ACS Nano **4**, 4388 (2010).

[164] M. J. Panzer and C. D. Frisbie, J. Am. Chem. Soc. **129**, 6599 (2007).

[165] H. Yuan, H. Shimotani, A. Tsukazaki, A. Ohtomo, M. Kawasaki, and Y. Iwasa, Adv. Funct. Mater. **19**, 1046 (2009).

[166] W. Xie, K. A. McGarry, F. Liu, Y. Wu, P. P. Ruden, C. J. Douglas, and C. D. Frisbie, J. Phys. Chem. **117**, 11522 (2013).

[167] F. T. Ulaby, E. Michielssen, and U. Ravaioli, *Fundamentals of applied electromagnetics*, 6th Edition (Upper Saddle River, NJ 07458, Prentice Hall, 2010)

[168] V. I. Kol'dyaev, A. Clerix, L. Deferm, and R. Van Overstraeten, J. Appl. Phys. **83**, 2131 (1998).

[169] Y. Xia, J. H. Cho, J. Lee, P. P. Ruden, and C. D. Frisbie, Adv. Mater. **21**, 2174 (2009).

[170] Y. Liang, C. D. Frisbie, H.-C. Chang, and P. P. Ruden, J. Appl. Phys. **105**, 024514 (2009).

[171] Y. Liang, H.-C. Chang, P. Paul Ruden, and C. Daniel Frisbie, J. Appl. Phys. **110**, 064514 (2011).

[172] M. Galiński, A. Lewandowski, and I. Stępniak, Electro. Acta **51**, 5567 (2006).

[173] S. Longo, L. D. Pietanza, F. A. Tassielli, M. Capitelli, Laser and Particle Beams **20**, 285 (2002).

[174] L. Burgi, N. Knorrl, H. Brune, M. A. Schneider, K. Kern, Appl. Phys. A **75**, 141 (2002).

[175] K. H. Lee, S. Zhang, T. P. Lodge, and C. D. Frisbie, J. Phys. Chem. B **115**, 3315 (2011).

[176] D. Braga, M. Campione, A. Borghesi, and G. Horowitz, Adv. Mater. **22**, 424 (2010).

[177] Y. Xia, W. Xie, P. P. Ruden, and C. D. Frisbie, Phys. Rev. Lett. **105**, 036802 (2010).

[178] H.-C. Chang, P. P. Ruden, Y. Liang, and C. D. Frisbie, J. Appl. Phys. 107, 104502 (2010).

[179] A. A. Kornyshev and R. Qiao, J. Phys. Chem. C **118**, 18285 (2014).

[180] C. Liang, Y. Wang, D. Li, X. Ji, F. Zhang, and Z. He, Solar Energy Mater. Solar Cells **127**, 67 (2014).

[181] A. Pierre, S. Lu, I. A. Howard, A. Facchetti, and A. C. Arias, J. Appl. Phys. **113**, 154506 (2013).

[182] H.-C. Chang, Ph.D. Dissertation, *Modeling of Electronic Properties in Organic Semiconductor Device Structures* (University of Minnesota, 2012).

Appendix

A. Derivations for section 4.2

The four-dimensional Hilbert space in section 4.2 is spanned by the electron and hole spin states of the polaron pair (PP). With notations $|spin_e\rangle|spin_h\rangle = |eh\rangle$, the eigenvectors are defined as follows:

$$\left|\uparrow\uparrow\right\rangle = \begin{pmatrix}1\\0\\0\\0\end{pmatrix}, \left|\uparrow\downarrow\right\rangle = \begin{pmatrix}0\\1\\0\\0\end{pmatrix}, \left|\downarrow\uparrow\right\rangle = \begin{pmatrix}0\\0\\1\\0\end{pmatrix}, \left|\downarrow\downarrow\right\rangle = \begin{pmatrix}0\\0\\0\\1\end{pmatrix}. \tag{A.1}$$

The 0^{th} order Hamiltonian (Zeeman effect) is:

$$H_Z = \sum_n Q_n(t)\frac{g\mu_B}{\hbar}\vec{B}\cdot\left(\vec{S}_h^n + \vec{S}_e^n\right) \tag{A.2}$$

Here $g \approx 2$ is the g-factor, μ_B is the Bohr magneton. n labels the molecular pair sites which can support a PP state, $Q_n(t)$ is unity if the molecular pair n is occupied by a PP at time t and zero otherwise. $\overrightarrow{S_h}$ and $\overrightarrow{S_e}$ are the spin operators for the hole and electron polarons on molecular pair site n, respectively. Assuming that the external magnetic field $\vec{B}$ is along the z-axis, the Hamiltonian can be written as:

$$\begin{aligned}\langle he|H_Z|eh\rangle &= \langle h|\langle e|H_Z|e\rangle|h\rangle = \sum_n Q_n(t)\frac{g\mu_B B_z}{2}\langle h|\langle e|\left(\sigma_{zh}^n + \sigma_{ze}^n\right)|e\rangle|h\rangle \\ &= \sum_n Q_n(t)\frac{g\mu_B B_z}{2}\left(\langle e|e\rangle\langle h|\sigma_{zh}^n|h\rangle + \langle h|h\rangle\langle e|\sigma_{ze}^n|e\rangle\right)\end{aligned} \tag{A.3}$$

σ_z^n is the *z*-component of the Pauli matrix of the polaron spin on molecular pair *n*. In matrix form the 0th order Hamiltonian can be expressed as:

$$H_Z = \sum_n Q_n(t) g\mu_B B_z \begin{pmatrix} 1 & 0 & 0 & 0 \\ 0 & 0 & 0 & 0 \\ 0 & 0 & 0 & 0 \\ 0 & 0 & 0 & -1 \end{pmatrix} \tag{A.4}$$

The density matrix equation for the polaron pair ensemble is given by:

$$\frac{d\rho}{dt} = \frac{i}{\hbar}[\rho, H_Z + H_{HF}] + \left.\frac{\partial \rho}{\partial t}\right|_{eh} + \left.\frac{\partial \rho}{\partial t}\right|_{EP} \tag{A.5a}$$

H_{HF} is the perturbation Hamiltonian due to the hyperfine interaction. It is convenient to define $\rho^* = \exp\left(\frac{i}{\hbar} H_Z t\right) \rho \exp\left(-\frac{i}{\hbar} H_Z t\right)$, and to transform equation (A.5a) into the interaction picture as:[1]

$$\frac{d\rho^*}{dt} = \frac{i}{\hbar}[\rho^*, H_{HF}^*] + \left.\frac{\partial \rho^*}{\partial t}\right|_{eh} + \left.\frac{\partial \rho^*}{\partial t}\right|_{EP} \tag{A.5b}$$

The advantage of this transformation is that, in steady state, ρ^* is constant in time, and the first term on the right hand side contains only the perturbation Hamiltonian, with $H_{HF}^* = \exp\left(\frac{i}{\hbar} H_Z t\right) H_{HF} \exp\left(-\frac{i}{\hbar} H_Z t\right)$.

The second term on right hand side of equation (A.5b) describes the formation rate of PPs from independent electron and hole polarons and the possible dissociation of

[1] C. P. Slichter, *Principles of Magnetic Resonance* 3rd Ed. (Springer, UIUC, IL, USA, 1990)

the PP back to independent electron and hole polarons. Assuming charge conservation and spin randomness, this term can be written as:

$$\left.\frac{\partial \rho^*}{\partial t}\right|_{eh} = \begin{pmatrix} R - L_{eh}\rho_{11}^* & -L_{eh}\rho_{12}^* & -L_{eh}\rho_{13}^* & -L_{eh}\rho_{14}^* \\ -L_{eh}\rho_{21}^* & R - L_{eh}\rho_{22}^* & -L_{eh}\rho_{23}^* & -L_{eh}\rho_{24}^* \\ -L_{eh}\rho_{31}^* & -L_{eh}\rho_{32}^* & R - L_{eh}\rho_{33}^* & -L_{eh}\rho_{34}^* \\ -L_{eh}\rho_{41}^* & -L_{eh}\rho_{42}^* & -L_{eh}\rho_{43}^* & R - L_{eh}\rho_{44}^* \end{pmatrix} \tag{A.6a}$$

R is the rate constant for forming the PP from independent electrons and holes and L_{eh} is the dissociation rate constant for PPs. The dissociation rate for PPs is assumed to be independent of polaron spin.

The third term on the right hand side of equation (A.5b) describes the rate of exciplex formation from PPs. It is proportional to the PP density, and can be written as:

$$\left.\frac{\partial \rho^*}{\partial t}\right|_{EP} = -\frac{1}{2}\left(\Lambda\rho^* + \rho^*\Lambda\right) \tag{A.6b}$$

The projection operator Λ commutes with H_Z, hence the ρ^* in equation (A.6) is interchangeable with ρ. The singlet and triplet states are given in the following matrix form:

$$|S\rangle = \frac{1}{\sqrt{2}}\left(|\uparrow\downarrow\rangle - |\downarrow\uparrow\rangle\right) = \frac{1}{\sqrt{2}}\begin{pmatrix} 0 \\ 1 \\ -1 \\ 0 \end{pmatrix} \tag{A.7a}$$

$$|T_0\rangle = \frac{1}{\sqrt{2}}\left(|\uparrow\downarrow\rangle + |\downarrow\uparrow\rangle\right) = \frac{1}{\sqrt{2}}\begin{pmatrix} 0 \\ 1 \\ 1 \\ 0 \end{pmatrix}, \quad |T_+\rangle = |\uparrow\uparrow\rangle = \begin{pmatrix} 1 \\ 0 \\ 0 \\ 0 \end{pmatrix}, \quad |T_-\rangle = |\downarrow\downarrow\rangle = \begin{pmatrix} 0 \\ 0 \\ 0 \\ 1 \end{pmatrix}. \tag{A.7b}$$

L_S and L_T are the singlet and triplet exciplex formation rates (we assume that the three triplet states have the same formation rate constants). The projection operator Λ can be expressed in terms of the exciplex formation rates and the projection to the corresponding exciplex basis: $\Lambda = \sum_{\lambda} L_\lambda |\lambda\rangle\langle\lambda|$, $\lambda = S$, T_0, T_+, or T_-. Written explicitly:

$$\Lambda = \begin{pmatrix} L_T & 0 & 0 & 0 \\ 0 & \frac{L_T + L_S}{2} & \frac{L_T - L_S}{2} & 0 \\ 0 & \frac{L_T - L_S}{2} & \frac{L_T + L_S}{2} & 0 \\ 0 & 0 & 0 & L_T \end{pmatrix} \tag{A.8}$$

Combining equations (A.6b) and (A.8), the matrix elements of the third term are expressed as:

$$\left.\frac{\partial \rho^*}{\partial t}\right|_{EP,11} = -L_T \rho^*_{11} \tag{A.9a}$$

$$\left.\frac{\partial \rho^*}{\partial t}\right|_{EP,12} = -\frac{L_S + 3L_T}{4}\rho^*_{12} - \frac{L_T - L_S}{4}\rho^*_{13} \tag{A.9b}$$

$$\left.\frac{\partial \rho^*}{\partial t}\right|_{EP,13} = -\frac{L_S + 3L_T}{4}\rho^*_{13} - \frac{L_T - L_S}{4}\rho^*_{12} \tag{A.9c}$$

$$\left.\frac{\partial \rho^*}{\partial t}\right|_{EP,14} = -L_T \rho^*_{14} \tag{A.9d}$$

$$\left.\frac{\partial \rho^*}{\partial t}\right|_{EP,22} = -\frac{L_T + L_S}{2}\rho^*_{22} - \frac{L_T - L_S}{4}\left(\rho^*_{23} + \rho^*_{32}\right) \tag{A.9e}$$

$$\left.\frac{\partial \rho^*}{\partial t}\right|_{EP,23} = -\frac{L_T + L_S}{2}\rho^*_{23} - \frac{L_T - L_S}{4}\left(\rho^*_{22} + \rho^*_{33}\right) \tag{A.9f}$$

$$\left.\frac{\partial \rho^*}{\partial t}\right|_{EP,24} = -\frac{L_S + 3L_T}{4}\rho^*_{24} - \frac{L_T - L_S}{4}\rho^*_{34} \tag{A.9g}$$

$$\left.\frac{\partial \rho^*}{\partial t}\right|_{EP,33} = -\frac{L_T + L_S}{2}\rho^*_{33} - \frac{L_T - L_S}{4}\left(\rho^*_{23} + \rho^*_{32}\right) \tag{A.9h}$$

$$\left.\frac{\partial \rho^*}{\partial t}\right|_{EP,34} = -\frac{L_S + 3L_T}{4}\rho^*_{34} - \frac{L_T - L_S}{4}\rho^*_{24} \tag{A.9i}$$

$$\left.\frac{\partial \rho^*}{\partial t}\right|_{EP,44} = -L_T\rho^*_{44} \tag{A.9j}$$

As the density matrix is Hermitian, only 10 of the 16 terms are independent.

H_{HF} is the perturbation Hamiltonian, which represents the hyperfine interaction between the hole/electron and the hydrogen nuclei of the host donor/acceptor molecule. As the electron and the hole polarons forming PP states may hop from one molecule to another neighboring molecule of the same kind, they interact with a fluctuating configuration of nuclear spins. The first term on the right hand side of equation (A.5b) can be obtained from Bloch-Wangsness-Redfield theory:[1,2,3,4]

$$\frac{i}{\hbar}\left[\rho^*, H^*_{HF}\right]_{\alpha\alpha'} = \sum_{\beta,\beta'} R_{\alpha\alpha',\beta\beta'}\rho^*_{\beta\beta'} \tag{A.10a}$$

where the sum only runs through the terms with $E_\alpha - E_{\alpha'} = E_\beta - E_{\beta'}$. The $R_{\alpha\alpha',\beta\beta'}$ terms are given by:

[1] C. P. Slichter, *Principles of Magnetic Resonance* 3rd Ed. (Springer, UIUC, IL, USA, 1990).
[2] A. G. Redfield, IBM J. Research Develop. **1**, 19 (1957).
[3] R. K. Wangsness and F. Bloch, Phys. Rev. **89**, 728 (1953).
[4] F. Bloch, Phys. Rev. **102**, 104 (1956).

$$R_{\alpha\alpha',\beta\beta'} = \frac{1}{2}\left[J_{\alpha\beta\alpha'\beta'}(\alpha'-\beta') + J_{\alpha\beta\alpha'\beta'}(\alpha-\beta) - \delta_{\alpha'\beta'}\sum_{\gamma} J_{\gamma\beta\gamma\alpha}(\gamma-\beta) - \delta_{\alpha\beta}\sum_{\gamma} J_{\gamma\alpha'\gamma\beta'}(\gamma-\beta') \right]$$

(A.10b)

where

$$J_{\alpha\alpha'\beta\beta'}(\omega) = \frac{1}{\hbar^2}\int_{-\infty}^{+\infty} \overline{\langle\alpha|H_{HF}(t)|\alpha'\rangle\langle\beta'|H_{HF}(t+\tau)|\beta\rangle} e^{-i\omega\tau} d\tau \qquad \text{(A.10c)}$$

Before writing equation (A.10a) explicitly, we comment on equation (A.10c). For the PP state, the electron and the hole are weakly bound, hence we assume that the hyperfine interaction with hydrogen nuclei on the acceptor (donor) molecule only affects the electron (hole) spin. There is no correlation between the electron and hole polaron spins in the PP state. Hence, the perturbation Hamiltonian can be separated into a hole-only part and an electron-only part:

$$H_{HF} = H_{HF}^{h} + H_{HF}^{e} \qquad \text{(A.11)}$$

The correlation term in eq. (10c) is simplified to:

$$\begin{aligned}
&\overline{\langle\alpha|H_{HF}(t)|\alpha'\rangle\langle\beta'|H_{HF}(t+\tau)|\beta\rangle} \\
&= \overline{\langle h|\langle e|\left(H_{HF}^{h}(t)+H_{HF}^{e}(t)\right)|e'\rangle|h'\rangle\langle h'|\langle e'|\left(H_{HF}^{h}(t+\tau)+H_{HF}^{e}(t+\tau)\right)|e\rangle|h\rangle} \\
&= \overline{\left(\langle h|H_{HF}^{h}(t)|h'\rangle\delta_{ee'} + \langle e|H_{HF}^{e}(t)|e'\rangle\delta_{hh'}\right)\left(\langle h'|H_{HF}^{h}(t+\tau)|h\rangle\delta_{ee'} + \langle e'|H_{HF}^{e}(t+\tau)|e\rangle\delta_{hh'}\right)} \\
&= \overline{\langle h|H_{HF}^{h}(t)|h'\rangle\langle h'|H_{HF}^{h}(t+\tau)|h\rangle\delta_{ee'} + \langle e|H_{HF}^{e}(t)|e'\rangle\langle e'|H_{HF}^{e}(t+\tau)|e\rangle\delta_{hh'}}
\end{aligned} \qquad \text{(A.12)}$$

In the last step, the cross terms are zero because the randomness makes the ensemble average of the 1st order terms zero. (For example, $\overline{\langle h|H_{HF}^{h}(t)|h'\rangle\langle e'|H_{HF}^{e}(t+\tau)|e\rangle} = 0$). Another relationship used here is $\langle\uparrow|H_1^{h,e}|\uparrow\rangle =$

$-\left\langle\downarrow\left|H_1^{h,e}\right|\downarrow\right\rangle$, which follows from the property of the Pauli matrix σ_z. Also we assume the correlation function is an even function of τ, therefore, all J terms are real, and

$$\begin{aligned} J_{\alpha\alpha'\beta\beta'}(\omega) &= \frac{1}{\hbar^2}\int_{-\infty}^{+\infty}\overline{\langle\alpha|H_{HF}(t)|\alpha'\rangle\langle\beta'|H_{HF}(t+\tau)|\beta\rangle}e^{-i\omega\tau}d\tau \\ &= \left[\frac{1}{\hbar^2}\int_{-\infty}^{+\infty}\overline{\langle\alpha'|H_{HF}(t)|\alpha\rangle\langle\beta|H_{HF}(t+\tau)|\beta'\rangle}e^{i\omega\tau}d\tau\right]^{+} \\ &= \left[J_{\alpha'\alpha\beta'\beta}(-\omega)\right]^{+} = J_{\alpha'\alpha\beta'\beta}(-\omega) \end{aligned} \tag{A.13}$$

where the "+" superscript denotes the complex conjugate. Using these relationships, all the correlation terms J can be expressed as linear combinations of the following:

Correlation between same hole spin:

$$J_S^h = \frac{1}{\hbar^2}\int_{-\infty}^{+\infty}\overline{\langle\uparrow|H_{HF}^h(t)|\uparrow\rangle\langle\uparrow|H_{HF}^h(t+\tau)|\uparrow\rangle}d\tau \tag{A.14a}$$

Correlation between same electron spin:

$$J_S^e = \frac{1}{\hbar^2}\int_{-\infty}^{+\infty}\overline{\langle\uparrow|H_{HF}^e(t)|\uparrow\rangle\langle\uparrow|H_{HF}^e(t+\tau)|\uparrow\rangle}d\tau \tag{A.14b}$$

Correlation between opposite hole spins:

$$J_O^h = \frac{1}{\hbar^2}\int_{-\infty}^{+\infty}\overline{\langle\downarrow|H_{HF}^h(t)|\uparrow\rangle\langle\uparrow|H_{HF}^h(t+\tau)|\downarrow\rangle}e^{iE\tau}d\tau \tag{A.14c}$$

Correlation between opposite electron spins:

$$J_O^e = \frac{1}{\hbar^2}\int_{-\infty}^{+\infty}\overline{\langle\downarrow|H_{HF}^e(t)|\uparrow\rangle\langle\uparrow|H_{HF}^e(t+\tau)|\downarrow\rangle}e^{iE\tau}d\tau \tag{A.14d}$$

where $E = g\mu_B B_z/\hbar$.

Combining equations (A.10) ~ (A.14), equation (A.10a) can be expressed explicitly as:

$$\frac{i}{\hbar}\left[\rho^*, H_{HF}^*\right]_{11} = -\left(J_O^h + J_O^e\right)\rho_{11}^* + J_O^h\rho_{22}^* + J_O^e\rho_{33}^* \tag{A.15a}$$

$$\frac{i}{\hbar}\left[\rho^*, H^*_{HF}\right]_{22} = J^h_O \rho^*_{11} - \left(J^h_O + J^e_O\right)\rho^*_{22} + J^e_O \rho^*_{44} \tag{A.15b}$$

$$\frac{i}{\hbar}\left[\rho^*, H^*_{HF}\right]_{33} = J^e_O \rho^*_{11} - \left(J^h_O + J^e_O\right)\rho^*_{33} + J^h_O \rho^*_{44} \tag{A.15c}$$

$$\frac{i}{\hbar}\left[\rho^*, H^*_{HF}\right]_{44} = J^e_O \rho^*_{22} + J^h_O \rho^*_{33} - \left(J^h_O + J^e_O\right)\rho^*_{44} \tag{A.15d}$$

$$\frac{i}{\hbar}\left[\rho^*, H^*_{HF}\right]_{12} = -\left(J^h_O + J^e_O + 2J^h_S\right)\rho^*_{12} + J^e_O \rho^*_{34} \tag{A.15e}$$

$$\frac{i}{\hbar}\left[\rho^*, H^*_{HF}\right]_{13} = -\left(J^h_O + J^e_O + 2J^e_S\right)\rho^*_{13} + J^h_O \rho^*_{24} \tag{A.15f}$$

$$\frac{i}{\hbar}\left[\rho^*, H^*_{HF}\right]_{14} = -\left(J^h_O + J^e_O + 2J^h_S + 2J^e_S\right)\rho^*_{14} \tag{A.15g}$$

$$\frac{i}{\hbar}\left[\rho^*, H^*_{HF}\right]_{23} = -\left(J^h_O + J^e_O + 2J^h_S + 2J^e_S\right)\rho^*_{23} \tag{A.15h}$$

$$\frac{i}{\hbar}\left[\rho^*, H^*_{HF}\right]_{24} = J^h_O \rho^*_{13} - \left(J^h_O + J^e_O + 2J^e_S\right)\rho^*_{24} \tag{A.15i}$$

$$\frac{i}{\hbar}\left[\rho^*, H^*_{HF}\right]_{34} = J^e_O \rho^*_{12} - \left(J^h_O + J^e_O + 2J^h_S\right)\rho^*_{34} \tag{A.15j}$$

So far all the terms in equation (A.5b) have been derived explicitly. The 10 equations can be categorized as belonging to one of three groups. Group I couples 11, 22, 33, 44, and 23 terms of the density matrix. Group II couples 12, 13, 24, and 34 terms. Group III includes only the 14 term. During time evolution, groups II and III gradually decay to zero. As the terms of electron and hole polarons forming polaron pairs are coupled to group I, at time $t \to \infty$ they approach nonzero values. The 23 off-diagonal term is nonzero because the Zeeman energy is the same for ↑↓ and ↓↑ states.

We are only interested in steady states, where only the group I terms are non-zero. Because all the coefficients are real, the calculated density matrix elements are also real. This leads to $\rho_{23}^{*}=\rho_{32}^{*}$. It is convenient to define the rates $K_{S,T} = L_{eh} + L_{S,T}$, and the five equations in group I are shown below:

$$-\left(J_O^h+J_O^e+K_T\right)\rho_{11}^{*}+J_O^h\rho_{22}^{*}+J_O^e\rho_{33}^{*}+R=0 \tag{A.16a}$$

$$J_O^h\rho_{11}^{*}-\left(J_O^h+J_O^e+\frac{K_S+K_T}{2}\right)\rho_{22}^{*}-\frac{K_T-K_S}{2}\rho_{23}^{*}+J_O^e\rho_{44}^{*}+R=0 \tag{A.16b}$$

$$J_O^e\rho_{11}^{*}-\frac{K_T-K_S}{2}\rho_{23}^{*}-\left(J_O^h+J_O^e+\frac{K_S+K_T}{2}\right)\rho_{33}^{*}+J_O^h\rho_{44}^{*}+R=0 \tag{A.16c}$$

$$J_O^e\rho_{22}^{*}+J_O^h\rho_{33}^{*}-\left(J_O^h+J_O^e+K_T\right)\rho_{44}^{*}+R=0 \tag{A.16d}$$

$$-\left(J_O^h+J_O^e+2J_S^h+2J_S^e+\frac{K_S+K_T}{2}\right)\rho_{23}^{*}-\frac{K_T-K_S}{4}\left(\rho_{22}^{*}+\rho_{33}^{*}\right)=0 \tag{A.16e}$$

Solving equation (A.16) gives the steady state solution for the polaron density matrix: (equation (4.4) in section 4.2)

$$\rho_{22}^{*}=\rho_{33}^{*}=\frac{2\left[K_T+2\left(J_O^h+J_O^e\right)\right]R}{\left(K_S+3K_T\right)\left(J_O^h+J_O^e\right)+K_T\left(K_S+K_T\right)-\dfrac{\left(K_S-K_T\right)^2\left(J_O^h+J_O^e+K_T\right)}{2\left(J_O^h+J_O^e\right)+4\left(J_S^h+J_S^e\right)+K_S+K_T}} \tag{A.17a}$$

$$\rho_{23}^{*}=\rho_{32}^{*}=\frac{K_S-K_T}{2\left(J_O^h+J_O^e\right)+4\left(J_S^h+J_S^e\right)+K_S+K_T}\rho_{22}^{*} \tag{A.17b}$$

$$\rho_{11}^{*}=\rho_{44}^{*}=\frac{R+\left(J_O^h+J_O^e\right)\rho_{22}^{*}}{J_O^h+J_O^e+K_T} \tag{A.17c}$$

Because $\rho_{\alpha\beta}^{*}=\exp\left(\frac{i}{\hbar}\left(E_\alpha-E_\beta\right)t\right)\rho_{\alpha\beta}$, we obtain $\rho_{\alpha\beta}^{*}=\rho_{\alpha\beta}$ if $\alpha=\beta$ or $\alpha,\beta=2,3$.

Using equation (4.1) in chapter 4, the correlation terms in equation (A.14) can be rearranged as:

$$\overline{\left\langle \downarrow \left| H_{HF}^{(e,h)}(t) \right| \uparrow \right\rangle \left\langle \uparrow \left| H_{HF}^{(e,h)}(t+\tau) \right| \downarrow \right\rangle} = \frac{2}{3} E_{HF(e,h)}^2 \sum_{n,n'} \overline{Q_n(t) Q_{n'}(t+\tau)} \qquad \text{(A.18a)}$$

$$\overline{\left\langle \uparrow \left| H_{HF}^{(e,h)}(t) \right| \uparrow \right\rangle \left\langle \uparrow \left| H_{HF}^{(e,h)}(t+\tau) \right| \uparrow \right\rangle} = \frac{1}{3} E_{HF(e,h)}^2 \sum_{n,n'} \overline{Q_n(t) Q_{n'}(t+\tau)} \qquad \text{(A.18b)}$$

$E_{HF,h}$ and $E_{HF,e}$ describe the corresponding strength of the hyperfine interaction. The prefactors 2/3 and 1/3 come from property that the opposite spin correlation is proportional to $\sigma_x^2 + \sigma_y^2$, while the same spin correlation is proportional to σ_z^2, and because of the randomness of hydrogen spin directions, the averages in *x*, *y*, and *z* directions are equal.

B. Derivations for section 4.4

In section 4.4, a weak exchange interaction in the polaron pair (PP) state is included. The 0th order Hamiltonian then can be written as:

$$H_0^n = H_Z^n + H_{PPEC}^n = \frac{g\mu_B}{\hbar}\vec{B}\cdot\left(\vec{S}_h^n + \vec{S}_e^n\right) - \frac{4}{\hbar^2}\Delta\left(\vec{S}_h^n \cdot \vec{S}_e^n\right) \tag{B.1}$$

The corresponding energies are obtained using equation (A.7):

$$E_S = \left\langle S\middle|H_{PPEC}^n\middle|S\right\rangle = 3\Delta \tag{B.2a}$$

$$E_T = \left\langle T\middle|H_{PPEC}^n\middle|T\right\rangle = -\Delta \text{ (3-fold degenerate)} \tag{B.2b}$$

In this case, it is more convenient to change the basis of the density matrix to S and T: 1 = T_+, 2 = S, 3 = T_0, and 4 = T_-. In this notation, the 0th order Hamiltonian only contains diagonal terms:

$$H_0^n = \begin{pmatrix} g\mu_B B_z - \Delta & 0 & 0 & 0 \\ 0 & 3\Delta & 0 & 0 \\ 0 & 0 & -\Delta & 0 \\ 0 & 0 & 0 & -g\mu_B B_z - \Delta \end{pmatrix} \tag{B.3}$$

Note that as Δ introduces coupling between the electron and the hole polaron wavefunctions, strictly the PP wavefunction is not separable, $|eh\rangle \neq |e\rangle|h\rangle$. However, for simplicity we will neglect this (weak) effect and still assume $|eh\rangle = |e\rangle|h\rangle$.

The $\left.\frac{\partial\rho}{\partial t}\right|_{eh}$ term in the new basis is the same as before:

$$\left.\frac{\partial \rho^*}{\partial t}\right|_{eh} = \begin{pmatrix} R - L_{eh}\rho_{11}^* & -L_{eh}\rho_{12}^* & -L_{eh}\rho_{13}^* & -L_{eh}\rho_{14}^* \\ -L_{eh}\rho_{21}^* & R - L_{eh}\rho_{22}^* & -L_{eh}\rho_{23}^* & -L_{eh}\rho_{24}^* \\ -L_{eh}\rho_{31}^* & -L_{eh}\rho_{32}^* & R - L_{eh}\rho_{33}^* & -L_{eh}\rho_{34}^* \\ -L_{eh}\rho_{41}^* & -L_{eh}\rho_{42}^* & -L_{eh}\rho_{43}^* & R - L_{eh}\rho_{44}^* \end{pmatrix} \tag{B.4}$$

For the term $\left.\frac{\partial \rho}{\partial t}\right|_{EP}$, following the same procedures as the previous section, the operator Λ is expressed as:

$$\Lambda = \begin{pmatrix} L_T & 0 & 0 & 0 \\ 0 & L_S & 0 & 0 \\ 0 & 0 & L_T & 0 \\ 0 & 0 & 0 & L_T \end{pmatrix} \tag{B.5}$$

and

$$\left.\frac{\partial \rho}{\partial t}\right|_{EP} = -\frac{1}{2}(\Lambda\rho + \rho\Lambda) = -\begin{pmatrix} L_T\rho_{11} & \frac{L_S + L_T}{2}\rho_{12} & L_T\rho_{13} & L_T\rho_{14} \\ \frac{L_S + L_T}{2}\rho_{21} & L_S\rho_{22} & \frac{L_S + L_T}{2}\rho_{23} & \frac{L_S + L_T}{2}\rho_{24} \\ L_T\rho_{31} & \frac{L_S + L_T}{2}\rho_{32} & L_T\rho_{33} & L_T\rho_{34} \\ L_T\rho_{41} & \frac{L_S + L_T}{2}\rho_{42} & L_T\rho_{43} & L_T\rho_{44} \end{pmatrix} \tag{B.6}$$

Because Λ commutes with H_0, ρ is interchangeable with ρ^*.

For the hyperfine interaction perturbation Hamiltonian we again apply Bloch-Wangsness-Redfield theory:[1,2,3,4]

$$\frac{i}{\hbar}\left[\rho^*, H_{HF}^*\right]_{\alpha\alpha'} = \sum_{\beta,\beta'} R_{\alpha\alpha',\beta\beta'} e^{i\frac{t}{\hbar}\left(E_\alpha - E_{\alpha'} - E_\beta + E_{\beta'}\right)} \rho_{\beta\beta'}^* \tag{B.7}$$

---

[1] C. P. Slichter, *Principles of Magnetic Resonance* 3rd Ed. (Springer, UIUC, IL, USA, 1990)
[2] A. G. Redfield, IBM J. Research Develop. **1**, 19 (1957).
[3] R. K. Wangsness and F. Bloch, Phys. Rev. **89**, 728 (1953).
[4] F. Bloch, Phys. Rev. **102**, 104 (1956).

Only the terms that satisfy $E_\alpha - E_{\alpha'} = E_\beta - E_{\beta'}$ are non-zero. The energies are shown as the corresponding diagonal terms in equation (B.3). Written explicitly, the non-zero terms are:

$$0 = E_1 - E_1 = E_2 - E_2 = E_3 - E_3 = E_4 - E_4,\ g\mu_B B_z = E_1 - E_3 = E_3 - E_4 \quad \text{(B.8)}$$

The $R_{\alpha\alpha',\beta\beta'}$ terms are given by equation (A.10b).

Similar to the previous case, the J terms can be summarized in terms of spin auto-correlations:

$$\begin{aligned} J_S^{\alpha\beta} &= J_S^h\left(E_\alpha - E_\beta\right) + J_S^e\left(E_\alpha - E_\beta\right) \\ &= \frac{1}{\hbar^2}\int_{-\infty}^{+\infty}\overline{\left\langle\uparrow\left|H_{HF}^h(t)\right|\uparrow\right\rangle\left\langle\uparrow\left|H_{HF}^h(t+\tau)\right|\uparrow\right\rangle}e^{-i\frac{\tau}{\hbar}\left(E_\alpha - E_\beta\right)}d\tau \\ &+ \frac{1}{\hbar^2}\int_{-\infty}^{+\infty}\overline{\left\langle\uparrow\left|H_{HF}^e(t)\right|\uparrow\right\rangle\left\langle\uparrow\left|H_{HF}^e(t+\tau)\right|\uparrow\right\rangle}e^{-i\frac{\tau}{\hbar}\left(E_\alpha - E_\beta\right)}d\tau \end{aligned} \quad \text{(B.9a)}$$

and:

$$\begin{aligned} J_O^{\alpha\beta} &= J_O^h\left(E_\alpha - E_\beta\right) + J_O^e\left(E_\alpha - E_\beta\right) \\ &= \frac{1}{\hbar^2}\int_{-\infty}^{+\infty}\overline{\left\langle\downarrow\left|H_{HF}^h(t)\right|\uparrow\right\rangle\left\langle\uparrow\left|H_{HF}^h(t+\tau)\right|\downarrow\right\rangle}e^{-i\frac{\tau}{\hbar}\left(E_\alpha - E_\beta\right)}d\tau \\ &+ \frac{1}{\hbar^2}\int_{-\infty}^{+\infty}\overline{\left\langle\downarrow\left|H_{HF}^e(t)\right|\uparrow\right\rangle\left\langle\uparrow\left|H_{HF}^e(t+\tau)\right|\downarrow\right\rangle}e^{-i\frac{\tau}{\hbar}\left(E_\alpha - E_\beta\right)}d\tau \end{aligned} \quad \text{(B.9b)}$$

Equation (B.7) is written explicitly as follows. (We are only interested in the diagonal terms because the off-diagonal terms have all decayed to zero in a steady state.)

$$\frac{i}{\hbar}\left[\rho^*, H_{HF}^*\right]_{11} = -\frac{1}{2}\left(J_O^{21} + J_O^{31}\right)\rho_{11}^* + \frac{1}{2}J_O^{21}\rho_{22}^* + \frac{1}{2}J_O^{31}\rho_{33}^* \quad \text{(B.10a)}$$

$$\frac{i}{\hbar}\left[\rho^*, H_{HF}^*\right]_{22} = \frac{1}{2}J_O^{21}\rho_{11}^* - \left(\frac{1}{2}J_O^{21} + \frac{1}{2}J_O^{42} + J_S^{32}\right)\rho_{22}^* + J_S^{32}\rho_{33}^* + \frac{1}{2}J_O^{42}\rho_{44}^* \quad \text{(B.10b)}$$

$$\frac{i}{\hbar}\left[\rho^*, H_{HF}^*\right]_{33} = \frac{1}{2}J_O^{31}\rho_{11}^* + J_S^{32}\rho_{22}^* - \left(J_O^{31} + J_S^{32}\right)\rho_{33}^* + \frac{1}{2}J_O^{31}\rho_{44}^* \quad \text{(B.10c)}$$

$$\frac{i}{\hbar}\left[\rho^*, H^*_{HF}\right]_{44} = \frac{1}{2}J_O^{42}\rho_{22}^* + \frac{1}{2}J_O^{31}\rho_{33}^* - \frac{1}{2}\left(J_O^{42} + J_O^{31}\right)\rho_{44}^* \tag{B.10d}$$

The next step is to solve the rate equation (A.5) for the steady state. After lengthy but straight-forward derivations, the following expressions are obtained:

$$\rho_{22} = \frac{C_1 B_2 - C_2 B_1}{A_1 B_2 - A_2 B_1} R \tag{B.11a}$$

$$\rho_{33} = \frac{C_1 A_2 - C_2 A_1}{B_1 A_2 - B_2 A_1} R \tag{B.11b}$$

$$\rho_{11} = \frac{2R + J_O^{21}\rho_{22} + J_O^{31}\rho_{33}}{2K_T + J_O^{21} + J_O^{31}} \tag{B.11c}$$

$$\rho_{44} = \frac{2R + J_O^{42}\rho_{22} + J_O^{31}\rho_{33}}{2K_T + J_O^{42} + J_O^{31}} \tag{B.11d}$$

where

$$A_1 = \frac{J_O^{21}J_O^{31}\left(J_O^{21} - J_O^{42}\right)}{4K_T + 2J_O^{21} + 2J_O^{31}} - \frac{1}{2}J_O^{31}J_O^{21} - \frac{1}{2}J_O^{31}J_O^{42} - J_O^{31}J_S^{32} - J_O^{31}K_S - J_O^{42}J_S^{32}$$

$$A_2 = \frac{J_O^{42}J_O^{31}\left(J_O^{42} - J_O^{21}\right)}{4K_T + 2J_O^{42} + 2J_O^{31}} - \frac{1}{2}J_O^{31}J_O^{21} - \frac{1}{2}J_O^{31}J_O^{42} - J_O^{31}J_S^{32} - J_O^{31}K_S - J_O^{21}J_S^{32}$$

$$B_1 = \frac{\left(J_O^{31}\right)^2\left(J_O^{21} - J_O^{42}\right)}{4K_T + 2J_O^{21} + 2J_O^{31}} + J_O^{31}J_S^{32} + J_O^{42}J_O^{31} + J_O^{42}J_S^{32} + J_O^{42}K_T$$

$$B_2 = \frac{\left(J_O^{31}\right)^2\left(J_O^{42} - J_O^{21}\right)}{4K_T + 2J_O^{42} + 2J_O^{31}} + J_O^{31}J_S^{32} + J_O^{21}J_O^{31} + J_O^{21}J_S^{32} + J_O^{21}K_T$$

$$C_1 = -\frac{J_O^{31}\left(J_O^{21} - J_O^{42}\right)}{2K_T + J_O^{21} + J_O^{31}} + J_O^{42} - J_O^{31}$$

$$C_2 = -\frac{J_O^{31}\left(J_O^{42} - J_O^{21}\right)}{2K_T + J_O^{42} + J_O^{31}} + J_O^{21} - J_O^{31}.$$

This is equation (4.15) in section 4.4.

C. Discussion on the correlation functions

In this appendix, we follow well-established approaches for the discussion on the correlation function.[1] From the Bloch-Wangsness-Redfield theory (Appendices A and B), as employed in chapter 4, the *J* terms can be written as:

$$J^{(e,h)} = \frac{\alpha}{\hbar^2}\int \overline{\left\langle S_i \left| H_{HF}^{(e,h)}(t) \right| S_f \right\rangle \left\langle S_f \left| H_{HF}^{(e,h)}(t+\tau) \right| S_i \right\rangle} \exp\left[i\frac{\tau}{\hbar}\left(E_f - E_i\right)\right] d\tau \qquad \text{(C.1)}$$

The "bar" denotes an ensemble average, and the symbols are defined in chapter 4. We have assumed that the electron (hole) spin only interacts with the hydrogen nuclei on the host acceptor (donor) molecule.

Equation (C.1) can be rearranged following equation (A.18), and subsequently simplified to equation (4.5) in chapter 4, by introducing a dimensionless quantity *f*, the correlation function.

$$f = \sum_{n,n'} f_{n,n'} = \sum_{n,n'} \overline{Q_n(t) Q_{n'}(t+\tau)} \qquad \text{(C.2)}$$

$Q_n(t)$ is unity if the molecular pair *n* is occupied by a polaron pair (PP) at time *t* and zero otherwise. The corresponding H_{HF}^{n} denotes the hyperfine interaction with the randomly oriented nuclear spins of the molecule pair *n*, and this configuration is taken to be static because the nuclear spins have long precession times. The PP stays on any given the molecular site *n* for only a relatively short time, τ, before hopping to another site.

[1] F. N. Hooge and P. A. Bobbert, Physica B **239**, 223 (1997).

Assuming there is no correlation between different sites, Equation (C.2) can be simplified to:

$$f(\tau) = \sum_n \overline{Q_n(t)Q_n(t+\tau)} \tag{C.3}$$

Evidently, $f(0) = N$, the total number of PPs in a given steady state. $\overline{Q_n(t)Q_n(t+\tau)}$ for a steady state should be an even function of τ and independent of t.

The correlation term associated with each molecular pair n is taken to have a relaxation time, τ_n. Therefore,

$$\frac{\partial}{\partial \tau}\overline{Q_n(t)Q_n(t+\tau)} = -\frac{1}{\tau_n}\overline{Q_n(t)Q_n(t+\tau)} \quad (\text{for } \tau > 0) \tag{C.4a}$$

$$\frac{\partial}{\partial \tau}\overline{Q_n(t)Q_n(t+\tau)} = \frac{1}{\tau_n}\overline{Q_n(t)Q_n(t+\tau)} \quad (\text{for } \tau < 0) \tag{C.4b}$$

Eq. (C.4) consequently gives the following relationship:

$$\overline{Q_n(t)Q_n(t+\tau)} = \overline{Q_n(t)Q_n(t)}\exp\left(-\frac{|\tau|}{\tau_n}\right) \tag{C.5}$$

If we assume a single relaxation time τ_0 for all the molecular pairs, then

$$f(\tau) = N\exp\left(-\frac{|\tau|}{\tau_0}\right) \tag{C.6}$$

And its Fourier transform is:

$$F(\omega) = N\frac{2\tau_0}{1+\tau_0^2\omega^2} \tag{C.7}$$

This is the type I function in chapter 4.

On the other hand, if we assume a wide distribution of correlation times τ_n, such that $\tau_L < \tau_n < \tau_U$ and $\tau_L << \tau_U$, Equation (C.3) can be rewritten as:

$$f(\tau)=\sum_n \overline{Q_n(t)Q_n(t)}\exp\left(-\frac{|\tau|}{\tau_n}\right) \tag{C.8}$$

$\overline{Q_n(t)Q_n(t)}$ is independent of τ, and the Fourier transform yields:

$$F(\omega)=\sum_n \overline{Q_n(t)Q_n(t)}\frac{2\tau_n}{1+\tau_n^2\omega^2} \tag{C.9}$$

On average, every molecular site n is equally probably occupied by a PP. There may be a total of M such sites:

$$F(\omega)=\frac{N}{M}\sum_n \frac{2\tau_n}{1+\tau_n^2\omega^2} \tag{C.10}$$

Now we assume that the molecular sites have energies E_n and that hopping is thermally activated: $\tau_n=\tau_{00}\exp\left(\frac{E_n}{kT}\right)$. We also assume that the density of levels E_n is a constant, D_0, over the range of interest. The sum over n then can be changed into the integral $D_0\int dE$, and subsequently written as $D_0\int d\tau_n \frac{kT}{\tau_n}$. Therefore,

$$\begin{aligned} F(\omega)&=\frac{N}{M}D_0kT\int_{\tau_L}^{\tau_U} d\tau_n \frac{2}{1+\tau_n^2\omega^2}=\frac{N}{M}D_0kT\frac{2}{\omega}\int_{\omega\tau_L}^{\omega\tau_U} dx\frac{1}{1+x^2} \\ &=\frac{N}{M}D_0kT\frac{2}{\omega}\left[\arctan(\omega\tau_U)-\arctan(\omega\tau_L)\right] \end{aligned} \tag{C.11}$$

From Equation (C.11) it is observed that in the zero frequency limit: $F(0)=\frac{2N}{M}D_0kT(\tau_U-\tau_L)\approx\frac{2N}{M}D_0kT\tau_U$. However, for ω in the wide range $\frac{1}{\tau_U}<<\omega<<\frac{1}{\tau_L}$, $F(\omega)\approx\frac{N}{M}D_0kT\frac{\pi}{\omega}$. Hence, for ω not too large, we may approximate this ω -dependence by the simpler analytic form:

$$F(\omega) \approx \frac{N}{M} D_0 kT \frac{2\tau_U}{1+\tau_U(2/\pi)\omega} \tag{C.12}$$

$2\tau_U/\pi$ may be written again as τ_0 recovering the type II form of the correlation function in chapter 4.

D. Discussion on the equivalent circuit model in chapter 5

The discussions in chapter 5 are based on the equivalent circuit model in FIG. 5.2. With source and drain terminals connected, the full expression for the admittance between gate and source/drain can be written as:

$$Y = \left(Z_{ES} + R_E + \frac{1}{j\omega C_{ME}} \right)^{-1} + j\omega C_{geo} \tag{D.1}$$

One might ask whether this model is valid or how well it can represent the real device. In this section, a qualitative explanation is given based on the idea of lumped vs. distributed circuit elements.

An equivalent circuit model is essentially a combination of ideal circuit elements that approximates the real device. For the model in FIG. 5.2, the double-layer charge interface is modeled as a single capacitor at the gate/electrolyte interface (lumped element), and as a capacitor/resistor network at the electrolyte/semiconductor interface (distributed element). The bulk electrolyte is represented by a single resistor (lumped element). Obviously, this is not the only choice. For example, FIG. D1 shows an alternative equivalent circuit model that expresses all circuit elements as distributed. The calculated gate-to-channel equivalent capacitance and the phase of admittance for both models are shown in FIG. D2. They coincide at low frequency but deviate at high frequency.

Both equivalent circuit models share some degree of inaccuracy when representing the real device. For the model in FIG. 5.2, it is assumed that beyond the first monolayers of ions at the electrolyte/semiconductor interface, the electrostatic potential is

equal everywhere. For the model in FIG. D1, the constraint of equal potential is eliminated, but at the same time it prohibits current flow in the electrolyte in the direction parallel to the interface. Neither of the models fully describes the physics of the system. In principle one can introduce additional distributed circuit elements to improve accuracy. However, this implies additional parameters, and for the discussions of EDLTs as explored in this work, the model in FIG. 5.2 is found to be adequate.

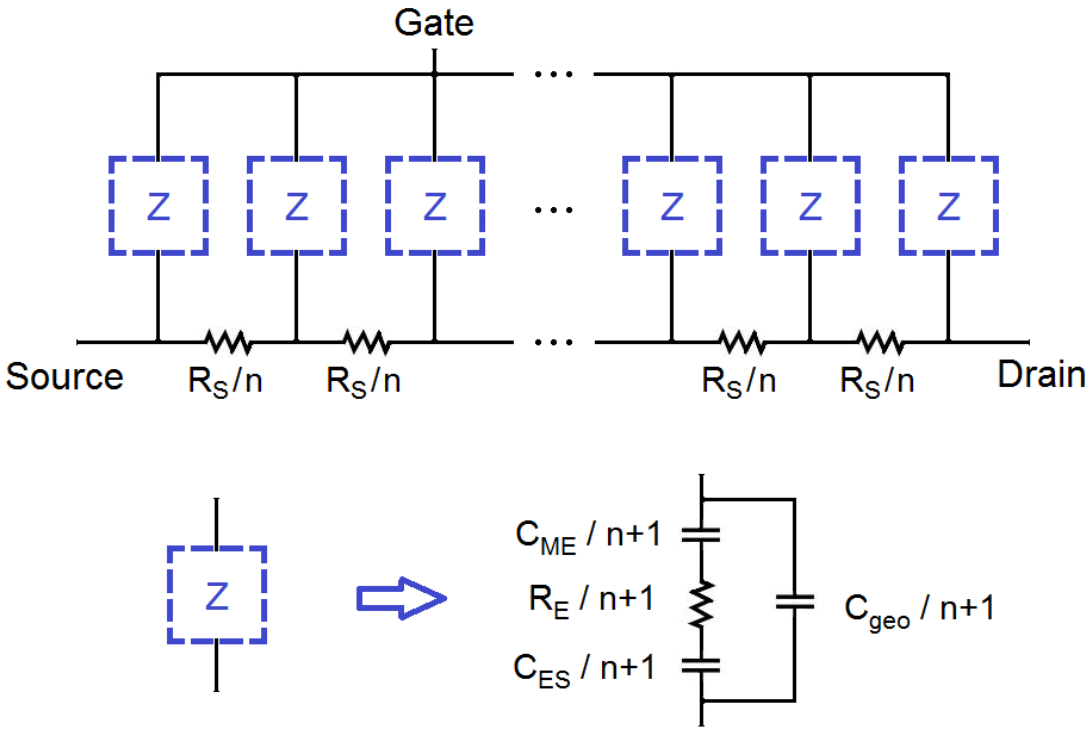

FIG. D1. An alternative equivalent circuit model for EDLTs, with all circuit elements in a distributed type.

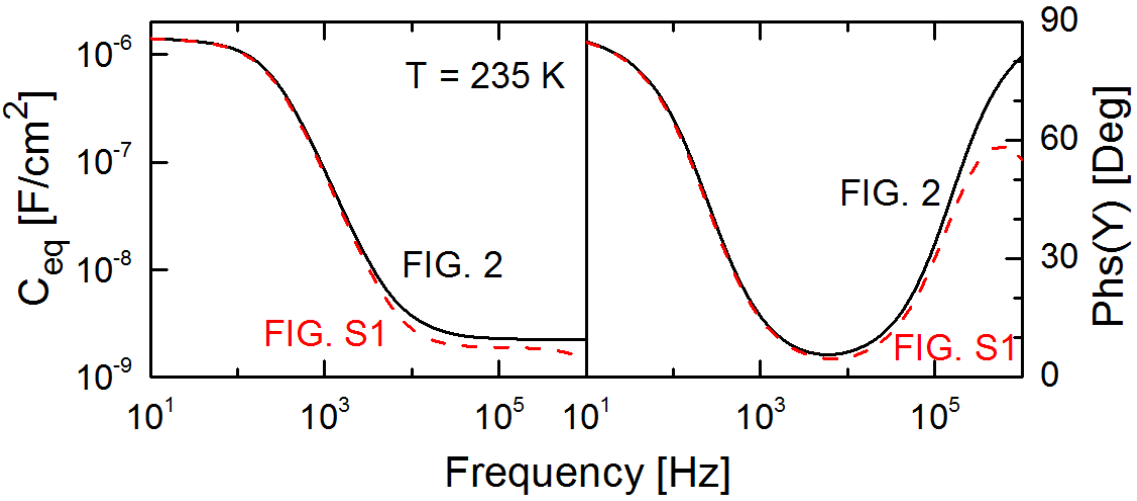

FIG. D2. The calculated equivalent gate-to-channel capacitance (left) and the phase of admittance (right) as a function of frequency at 235 K. The black solid lines are from the equivalent circuit model in FIG. 5.2 of chapter 5. The red dashed lines are from the model in FIG. D1 with the same parameters.

E. Frequency Window for Conductance-Capacitance Coupling

In chapter 5, a characteristic frequency f_C is estimated. For $f > f_C$, the capacitance-voltage plot follows a similar behavior as the conductance-voltage plot. In other words, f_C is the minimum frequency limit for the coupling effect. In this section, we show that there also exists a maximum frequency, f_{max}, beyond which the coupling effect vanishes. Therefore, the conductance-capacitance coupling can be observed only in the frequency window $f_C < f < f_{max}$, where f_C and f_{max} are determined by device parameters.

Based on the discussion of Z_{ES} in chapter 5, the device admittance in equation (D.1) for $f > f_C$ can be simplified to:

$$Y = \left(\frac{1}{2} \sqrt{\frac{R_S}{j\omega C_{ES}}} + R_E + \frac{1}{j\omega C_{ME}} \right)^{-1} + j\omega C_{geo} \qquad \text{(E.1)}$$

As the frequency increases, the first and third terms in the bracket decrease and eventually ($f > f_{max}$) Y is reduced to $1/R_E + j\omega C_{geo}$. The gate-to-channel equivalent capacitance is then the geometric capacitance, and the coupling to the channel conductance disappears.

A rough estimation of f_{max} is $(2\pi R_E C_{geo})^{-1}$. In our device f_{max} is approximately 10^6 Hz. The measured gate-to-channel capacitance is shown in FIG. E1. The 10^4 Hz curve is the same as that in FIG. 5.5(d). It is observed that, as the frequency increases, the capacitance approaches C_{geo}, which is consistent with the results in FIG. 5.4(c). The difference between the maximum and minimum of the capacitance (which implies a voltage-dependent conductance) decreases greatly with increasing frequency.

The minimum frequency, f_C, is determined by the semiconductor channel conductance and the electrolyte/semiconductor interface capacitance, while the maximum frequency, f_{max}, is determined by the electrolyte conductance and the geometric capacitance. Therefore, in order to observe the capacitance-conductance coupling effect, the device must be designed to ensure $f_C < f_{max}$.

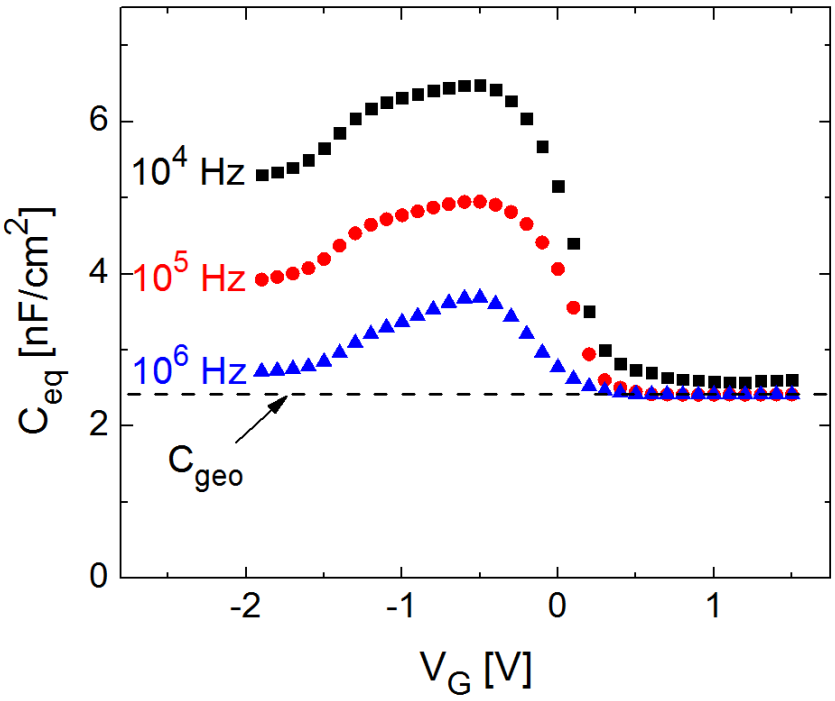

FIG. E1. Equivalent gate-to-channel capacitance-voltage characteristics of EDLTs at 235 K in the high frequency regime. The squares, circles and triangles are experimental data for the same device as FIG. 5.5 in chapter 5. The dashed line is the geometric capacitance of the device. Experimental data are countesy of Dr. Wei Xie et al. at University of Minnesota.

List of journal publications during my Ph.D. at University of Minnesota (Conference proceedings are not included.)

1. **Feilong Liu**, P. Paul Ruden, Ian H. Campbell, and Darryl L. Smith, "Exciplex current mechanism for ambipolar bilayer organic light emitting diodes", *Applied Physics Letters*, **99**, 123301 (2011). *Selected as frontier research for the October 3, 2011 issue of Virtual Journal of Nanoscale Science & Technology*

2. **Feilong Liu**, P. Paul Ruden, Ian H. Campbell, and Darryl L. Smith, "Device model for electronic processes at organic/organic interfaces", *Journal of Applied Physics*, **111**, 094507 (2012).

3. **Feilong Liu**, P. Paul Ruden, Ian H. Campbell, and Darryl L. Smith, "Electrostatic capacitance in single and double layer organic diodes", *Applied Physics Letters*, **101**, 023501 (2012).

4. **Feilong Liu**, Brian K. Crone, P. Paul Ruden, and Darryl L. Smith, "Control of interface microscopic processes in organic bilayer structures and their effect on photovoltaic device performance", *Journal of Applied Physics*, **113**, 044516 (2013).

5. Wei Xie, Kathryn A. McGarry, **Feilong Liu**, Yanfei Wu, P. Paul Ruden, Christopher J. Douglas, and C. Daniel Frisbie, "High mobility transistors based on single crystals of isotopically substituted rubrene-d_{28}", *Journal of Physical Chemistry C*, **117**, 11522 (2013).

6. **Feilong Liu**, Yue Liu, Jiaxi Hu, Darryl L. Smith, and P. Paul Ruden, "Rashba-induced spin scattering at graphene edges", *Journal of Applied Physics*, **114**, 093708 (2013).

7. **Feilong Liu**, Wei Xie, Sha Shi, C. Daniel Frisbie, and P. Paul Ruden, "Coupling of channel conductance and gate-to-channel capacitance in electric double layer transistors", *Applied Physics Letters*, **103**, 193304 (2013).

8. Wei Xie, **Feilong Liu**, Sha Shi, P. Paul Ruden, and C. Daniel Frisbie, "Charge density dependent two-channel conduction in organic electric double layer transistors (EDLTs)", *Advanced Materials*, **26**, 2527 (2014).

9. S. A. Crooker, **F. Liu**, M. R. Kelley, N. J. D. Martinez, W. Nie, A. Mohite, I. H. Nayyar, S. Treitak, D. L. Smith, and P. P. Ruden, "Spectrally-resolved hyperfine interactions between polaron and nuclear spins in organic light emitting diodes: Magneto-EL studies", *Applied Physics Letters*, **105**, 153304 (2014).

10. Yue Liu, Aditi Goswami, **Feilong Liu**, Darryl L. Smith, and P. Paul Ruden, "Scattering in graphene associated with charged out-of-plane impurities", *Journal of Applied Physics*, **116**, 234301 (2014).

11. **Feilong Liu**, Megan R. Kelley, Scott A. Crooker, Wanyi Nie, Aditya D. Mohite, P. Paul Ruden, and Darryl L. Smith, "Magnetoelectroluminescence of organic heterostructures: Analytical theory and spectrally resolved measurements", *Physical Review B*, **90**, 235314 (2014).

12. Sha Shi, **Feilong Liu**, Darryl L. Smith, and P. Paul Ruden, "Effects of disorder on spin injection and extraction for organic semiconductor spin-valves", *Journal of Applied Physics*, **117**, 085501 (2015).

13. Wanyi Nie, Gautam Gupta, Brian K. Crone, **Feilong Liu**, Darryl L. Smith, P. Paul Ruden, Cheng-Yu Kuo, Hsinhan Tsai, Hsing-Lin Wang, Hao Li, Sergei Tretiak, and

Aditya D. Mohite, “Interface design principles for high efficiency organic semiconductor devices”, to appear in *Advance Science*.